# PREPARATION AND CHARACTERIZATION OF NIOBIA-CONTAINING SOLID ACID

**A THESIS**
**SUBMITTED TO THE DEPARTMENT OF CHEMISTRY**
**AND THE INSTITUTE OF ENGINEERING AND SCIENCES OF**
**BILKENT UNIVERSITY**
**IN PARTIAL FULFILLMENT OF THE REQUIREMENTS**
**FOR THE DEGREE OF**
**DOCTOR OF PHILOSOPHY**

**By**
**İLKNUR ÇAYIRTEPE**

**January 2010**

I certify that I have read this thesis and that in my opinion it is fully adequate, in scope and quality, as a dissertation for the degree of Doctor of philosophy.

_____

Assoc. Prof. Dr. Margarita Kantcheva (Supervisor)

I certify that I have read this thesis and that in my opinion it is fully adequate, in scope and quality, as a dissertation for the degree of Doctor of philosophy.

_____

Prof. Dr. Ömer Dağ

I certify that I have read this thesis and that in my opinion it is fully adequate, in scope and quality, as a dissertation for the degree of Doctor of philosophy.

_____

Assoc. Prof. Dr. Oğuz Gülseren

I certify that I have read this thesis and that in my opinion it is fully adequate, in scope and quality, as a dissertation for the degree of Doctor of philosophy.

_____

Assist. Prof. Dr. Emrah Özensoy

I certify that I have read this thesis and that in my opinion it is fully adequate, in scope and quality, as a dissertation for the degree of Doctor of philosophy.

_____

Prof. Dr. Gürkan Karakaş

Approved for the Institute of Engineering and Sciences

_____

Prof. Dr. Mehmet Baray
Director of Institute of Engineering and Science

## ABSTRACT

# PREPARATION AND CHARACTERIZATION OF NIOBIA-CONTAINING SOLID ACID

**İLKNUR ÇAYIRTEPE**

**Ph.D. in Chemistry**

**Supervisor: Assoc. Prof. Dr. Margarita Kantcheva**

**January 2010**

The research in this work is directed towards (i) the development of effective methods for synthesis of new solid acids based on zirconia and niobia resulting in high concentration of acid sites and (ii) investigation of the potential of these materials as catalysts for the selective catalytic reduction (SCR) of nitrogen oxides ($NO_x$) with hydrocarbons and alcohol transformations. A series of $NbO_x/ZrO_2$ and $WO_x/Nb_2O_5$ samples have been obtained by the so called "peroxo route" using acidic $H_2O_2$ solutions as a reaction medium. The impregnation of hydrated zirconia with solutions of $[Nb_2(O_2)_3]^{4+}$ ions allows the synthesis of $Nb_2O_5$-$ZrO_2$ samples with niobium loading up to 30 wt % without formation of a seperate $Nb_2O_5$ phase. The presence of a single phase

of $Zr_6Nb_2O_{17}$ has been observed for the sample containing 25 wt% of Nb. The formation of $Zr_6Nb_2O_{17}$ is favored by the partial solubility of hydrated zirconia in the $H_2O_2$ solution. Among the fully crystallized $Nb_2O_5$-based samples, the solid $WO_3$-$Nb_2O_5$ solution containing 20 wt % of $WO_3$ has the highest and strongest Brønsted acidity.

Catalytic activity tests for the $C_3H_6$-SCR of $NO_x$ have shown that Pd-free and Pd-promoted niobia-based samples containing 20 wt% $WO_3$ are inactive, whereas the $Zr_6Nb_2O_{17}$ and 0.1Pd/ $Zr_6Nb_2O_{17}$ samples catalyze this reaction. The conversion of $NO_x$ in the SCR of $NO_x$ with propene in excess oxygen over $Zr_6Nb_2O_{17}$ passes through a maximum at 493 K. The mixed oxide displays good water tolerance and resistance toward $SO_2$ poisoning. Based on the in situ FT-IR results, a reaction mechanism is proposed with nitroacetone and NCO species as the key reaction intermediates. The results of the investigation show that the catalytic properties of the new solid acid $Zr_6Nb_2O_{17}$ could be of interest regarding the development of sulfur- and water-tolerant, low-temperature catalysts for the SCR of $NO_x$ with hydrocarbons.

The $Zr_6Nb_2O_{17}$ and $Nb_2O_5$-containing 20 % $WO_3$ samples have potential as low-temperature catalysts for oxidant-free or oxidative transformation of alcohols, respectively.

**Key words:** $Nb_2O_5/ZrO_2$, $WO_3/Nb_2O_5$, synthesis from $H_2O_2$ precursor solutions, HC-SCR of $NO_x$; catalytic activity; in situ FT-IR spectroscopy; reaction mechanism; alcohol transformation.

# ÖZET

## NİYOBYA İÇEREN KATI ASİTLERİN HAZIRLANMASI VE KARAKTERİZASYONU

**İLKNUR ÇAYIRTEPE**

**Danışman: Doç. Dr. Margarita Kantcheva**

**Ocak 2010**

Bu çalışmadaki araştırma, (i) yüksek yoğunluklu asit bölgeleriyle sonuçlanan, zirkonya ve niyobya temelli yeni katı asitlerin sentezlenmesinde etkin yöntemlerin geliştirilmesine; ve (ii) hidrokarbonlarla nitrojen oksitlerin ($NO_x$) seçici katalitik indirgenmesinde (SKİ) ve alkol dönüşümlerinde katalizör olarak bu malzemelerin potansiyelinin araştırılmasına yönlendirilmiştir. $NbO_x/ZrO_2$ ve $WO_x/Nb_2O_5$ malzemeleri, tepkime ortamı olarak asidik $H_2O_2$ çözeltilerinin kullanıldığı "perokso yol" ile sentezlenmiştir. Hidratlı zirkonyanın $[Nb_2(O_2)_3]^{4+}$ iyonlarıyla doyurulması, ayrı $Nb_2O_5$ fazı oluşmadan ağırlıkça %30 a kadar niyobyum içeren $Nb_2O_5$-$ZrO_2$ numunelerinin sentezlenmesine izin verir. $Zr_6Nb_2O_{17}$ tek fazın varlığı, ağırlıkça % 25 Nb içeren numunede gözlemlenmiştir. $Zr_6Nb_2O_{17}$ oluşması, $H_2O_2$ çözeltisinde hidratlı zirkonyanın

kısmi çözünürlüğü tarafından elverişli kılınır. Tümüyle kristallenmiş $Nb_2O_5$-temelli numuneler içinde, ağırlıkça %20 $WO_3$ içeren katı $WO_3$-$Nb_2O_5$ çözeltisi en yüksek ve kuvvetli Brønsted asitliğe sahiptir.

$NO_x$ $C_3H_6$-SKİ tepkimesi için katalitik aktivite testleri göstermektedir ki; Pd-içermeyen ve Pd-eklenmiş ağırlıkça % 20 $WO_3$ içeren niyobya temelli numuneler aktif değilken, $Zr_6Nb_2O_{17}$ ve 0.1Pd/ $Zr_6Nb_2O_{17}$ numuneleri bu tepkimeyi katalizlemektedir. Bol oksijenli ortamda, propenli $NO_x$ SKİ tepkimesinde $NO_x$ dönüşümü, 493 K de maksimumdan geçmektedir. Karışık oksit, su karşı iyi tolerans ve $SO_2$ zehirlenmesine karşı iyi direnç göstermektedir. FT-IR sonuçlarına göre; anahtar tepkime ara-ürünleri olarak nitroaseton ve NCO türlerinin içerildiği tepkime mekanizması önerilmiştir. Araştırmaların sonuçları göstermektedir ki; hidrokarbonlarla $NO_x$ SKİ tepkimesi için yeni katı asitin, $Zr_6Nb_2O_{17}$, katalitik özellikleri kükürt- ve su- toleranslı, düşük-sıcaklık katalizörleri geliştirme açısından önemlidir.

$Zr_6Nb_2O_{17}$ ve % 20 $WO_3$ içeren $Nb_2O_5$ temelli numuneler, sırasıyla, alkollerin oksitleyici-içermeyen ve oksidatif dönüşümlerinde düşük-sıcaklık katalizörleri olarak potansiyele sahiptir.

Anahtar kelimeler: $Nb_2O_5/ZrO_2$, $WO_3/Nb_2O_5$, $H_2O_2$ öncül çözeltilerinden sentez, $NO_x$ HK-SKİ; katalitik aktiflik; yerinde FT-IR spektroskopi; reaksiyon mekanizması, alkol dönüşümü.

## ACKNOWLEGMENTS

It is a pleasure for me to express my deepest gratitude to Dr. Margarita Kantcheva for her supervision, encouragement and guidance throughout the development of this thesis.

I would like to thank Assist. Prof. Emrah Özensoy and Assoc. Prof. Oğuz Gülseren for reading and commenting on this thesis.

I appreciate the moral support by my friends; Yurdanur Türker, Fatih Mustafa Genişel, Cemal Albayrak, Stanislava Andova, Ivalina Avramova and Emine Kayhan.

I would like to thank all present and former members of Bilkent University, Chemistry Department for their help.

I would like to thank Bilkent University and the Scientific and Technical Research Council of Turkey for the financial support.

I would like to express my deepest gratitude to my daughter, Elif, and my husband, Fatih, for endless support, patient and love. I would like to give my special thanks to my family.

## TABLE OF CONTENTS

## LIST OF TABLES

## LIST OF FIGURES

# I. Introduction

## I.1. Environmental Problems, Regulations and Possible Solutions

Gaseous products of the combustion of fossil fuels, like natural gas, diesel oil, coal, gasoline or fuel oil, are emitted as exhaust gas from mobile sources, e.g. Otto, Diesel, jet and rocket engines, and stationary sources, such as power plants and chemical industry. Air pollution caused primarily by the exhaust gases from the mobile sources is taken attention due to a gradual increase in the number of vehicles in the world. Despite the fact that the fuel combusted in an ideal system should produce only water vapor ($H_2O$) and carbon dioxide ($CO_2$), the presence of intolerable amounts of carbon monoxide (CO), unburned and/or partially burned hydrocarbons (HCs) or particulate matter (PM) due to incomplete oxidation and nitrogen oxides ($NO_x$), sulfur oxides ($SO_x$) produced from N- and S-containing components in the fuel are detected in the exhaust gas as undesirable harmful or toxic chemicals. Their concentrations vary depending on the type of engine, fuel specification and driving conditions, e.g. idling, deceleration and acceleration. Typical compositions of the exhaust gases from lean burn (Diesel) and gasoline engines are shown in Table 1 [1].

Exhaust compounds listed in Table 1 can split into two subclasses:

1. Harmless compounds, $CO_2$, $H_2O$, $O_2$ and $N_2$ (not listed in Table 1), because they do not affect the health of human-being directly. Nevertheless, among them $CO_2$ and $H_2O$ cause greenhouse effect. That is why there is consensus on the limit for the emission of $CO_2$ released by automobiles, for which auto-manufacturers will have been developing and applying the hybrid systems.
2. Regulated compounds, $NO_x$, HC, CO, $SO_x$ and PM, which directly affect our health and habitat adversely.

**Table 1.** Typical compositions for the exhaust gases of diesel and gasoline engines [1].

| **Exhaust components** | **Diesel engine Vol %** | **Gasoline engine Vol %** |
|---|---|---|
| $NO_x$ | 0.003 – 0.06 % | 0.1 – 6 % |
| HC | 0.005 – 0.05 % C | 0.5 – 1 % C |
| CO | 0.01 – 0.1 % | 0.1 – 6 % |
| $O_2$ | 5 – 15 % | 0.2 – 2 % |
| $H_2O$ | 2 – 10 % | 10 – 12 % |
| $CO_2$ | 2 – 12 % | 10 – 13.5 % |
| $SO_x$ (proportional to fuel S content) | 10 – 100 ppm | 15 – 60 ppm |
| PM | 20 – 200 $mg/m^3$ | 1 – 10 $mg/m^3$ |
| λ (A/F) | 1.1 – 6 | 0.9 – 1.1 |

Since 1992, there exist European emission standards for heavy-duty diesel engines and gasoline and diesel engines for passengers. Table 2 shows the changes in the exhaust emission limits with the years [2,3,4]. Since Turkey import generally all types of engines from EU countries, EU legislations are met automatically [2].

Intense research has been lasting on modified and/or alternative fuels. Unleaded and oxygenated gasoline with higher octane rating reduces the CO and HC emissions from the Otto engines. The emissions of $SO_x$, $NO_x$ and PM are lowered by decreasing the contents of sulfur and aromatic compounds in the fuel for the diesel engines [1]. EU countries have been using sulfur-free diesel and gasoline fuels (≤ 10 ppm S) since 2005 and sulfur-free fuels will be mandatory after 2009 [2]. Moreover, the use of synthetic diesel fuel and biodiesel can help reducing the regulated compounds. Alternative to the conventional diesel fuel, compressed natural gas and liquefied petroleum gas have beneficial effect on the reduction of $NO_x$ and PM emissions [1,5].

**Table 2.** Changes in the exhaust emission limits with the years [2,3,4].

| **Date** | **CO** | **$NO_x$** | **Total HC** | **Non-methane HC** | **HC+$NO_x$** | **PM** |
|---|---|---|---|---|---|---|
| Gasoline engines | g/kg | g/kg | g/kg | g/kg | g/kg | g/kg |
| 1992, Euro 1 | 2.72 | - | - | - | 0.97 | - |
| 1996, Euro 2 | 2.2 | - | - | - | 0.5 | - |
| 2000, Euro 3 | 2.3 | 0.15 | 0.20 | - | - | - |
| 2005, Euro 4 | 1.0 | 0.08 | 0.10 | - | - | - |
| 2009, Euro 5 | 1.000 | 0.060 | 0.100 | 0.068 | - | 0.005 |
| 2014, Euro 6 | 1.000 | 0.060 | 0.100 | 0.068 | - | 0.005 |
| Diesel engines | g/kg | g/kg | g/kg | g/kg | g/kg | g/kg |
| 1992, Euro 1 | 2.72 | - | - | - | 0.97 | 0.14 |
| 1996, Euro 2 | 1.0 | - | - | - | 0.7 | 0.08 |
| 2000, Euro 3 | 0.64 | 0.50 | - | - | 0.56 | 0.05 |
| 2005, Euro 4 | 0.50 | 0.25 | - | - | 0.30 | 0.025 |
| 2009, Euro 5 | 0.500 | 0.180 | - | - | 0.230 | 0.005 |
| 2014, Euro 6 | 0.500 | 0.080 | - | - | 0.170 | 0.005 |
| HD Diesel engines | g/kWh | g/kWh | | HC, g/kWh | Smoke, $m^{-1}$ | g/kWh |
| 1992, Euro I | 4.5 | 8.0 | | 1.1 | - | 0.36 |
| 1996, Euro II | 4.0 | 7.0 | | 1.1 | - | 0.15 |
| 2000, Euro III | 2.1 | 5.0 | | 0.66 | 0.8 | 0.10 |
| 2005, Euro IV | 1.5 | 3.5 | | 0.46 | 0.5 | 0.02 |
| 2008, Euro V | 1.5 | 2.0 | | 0.46 | 0.5 | 0.02 |
| 2013, Euro VI | 1.5 | 0.5 | | 0.13 | - | 0.01 |

Another way of satisfying the emission limits is to utilize the advance technology in the diesel engine. Optimization of the engine parameters, e.g. injection rate shaping, turbocharging, exhaust gas recirculation, fuel nozzle, improves the $NO_x$ and PM emissions [1,5,6].

To ensure the strict emission limits the exhaust gas treatment techniques, which are so called “aftertreatment systems”, should be used by combining with the mentioned solutions. The aftertreatment systems aim reducing the concentration of $NO_x$ over different catalysts under different working conditions of the engines.

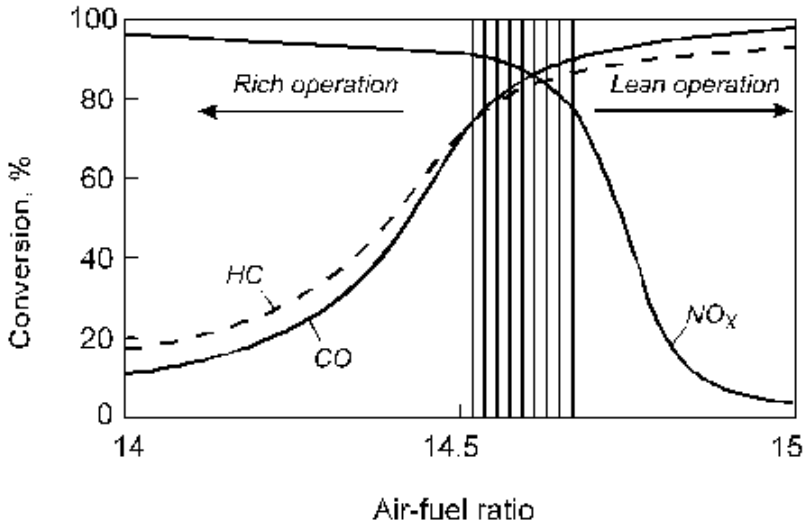


Fig. 1. The conversion efficiency (%) of a three-way catalyst as a function air to fuel (A/F) ratio. The lambda window, (A/F=14.7), corresponds to a stoichiometric operation, $\lambda = 1$ [9].

The gasoline engine operating at the stoichiometric air to fuel ratio (A/F=14.7) is equipped with the "three-way catalytic converter" (TWC), which oxidizes CO and HC and reduces $NO_x$ with HC, CO and $H_2$ (Fig. 1) [7,8,9]. The overall catalytic reactions are the followings:

| | |
|---|---|
| Oxidation reactions | $2CO + O_2 \rightarrow 2CO_2$ |
| | $C_xH_y + (x+\frac{y}{4})\ O_2 \rightarrow xCO_2 + \frac{y}{4}\ H_2O$ |
| Reduction reactions | $2NO + 2CO \rightarrow N_2 + 2CO_2$ |
| | $(2x+\frac{y}{2})\ NO + C_xH_y \rightarrow (x+\frac{y}{4})\ N_2 + xCO_2 + \frac{y}{2}\ H_2O$ |
| | $2NO + 2H_2 \rightarrow N_2 + H_2O$ |
| Water-gas shift reaction | $CO + H_2O \rightarrow CO_2 + H_2$ |
| Steam reforming | $C_xH_y + 2xH_2O \rightarrow xCO_2 + (2x+\frac{y}{2})\ H_2$ |

The commercially available three way catalyst contains Pt-Rh and/or Pd-Rh noble metals dispersed on a washcoat made up of $Al_2O_3$, $CeO_2$, $ZrO_2$, CaO, MgO and $La_2O_3$ [10]. Although rhodium catalyzes the reduction of $NO_x$, platinum and palladium help oxidizing CO and HC. Any deviation from air to fuel ratio (A/F=14.7) results in changes of the amounts of oxidizing and reducing agents in the exhaust gas even though the legislation limits must always be met under any conditions. Moreover, fuel economy cannot be achieved since the optimum performance of the TWC is accomplished at the stoichiometric A/F ratio.

The advantages of lean-burn gasoline engines are to promote the complete combustion, which reduces the emissions of CO and HC, and to provide significant fuel economy increasing the air to fuel ratio from 14.7 to 25 without changing the engine power [11,12]. Nevertheless, the high level of $NO_x$ emission appears as the main drawback. Toyota Motor Corporation developed "$NO_x$ storage reduction (NSR) catalyst" for the lean-burn gasoline engines in 1994 [13]. The working principle is that under lean burn conditions $NO_x$ is stored in the form of nitrate/nitrite on the surface of basic component (Ba sites). When the cycle shifts to fuel rich or stoichiometric (A/F= 14.7) conditions, the stored $NO_x$ species are reduced by HC, CO and $H_2$ over precious metals in order to regenerate catalyst for the next cycle [7,8,11,13,14]. The NSR catalyst consists of two noble metals:

1. Pt, which oxidizes CO, NO and HC and promotes the formation of $Ba(NO_3)_2$ under oxidizing conditions and facilities the decomposition of $Ba(NO_3)_2$ under reducing conditions [8,14].
2. Rh, which enhances the reduction of NO by CO and acts as a steam reforming catalyst with $ZrO_2$ making easier the removal of sulfur under reducing conditions [8,14].

The NSR catalyst cannot be used commercially in any countries except Japan due to high sulfur content of gasoline. The presence of $SO_2$ in the exhaust gas poisons the $NO_x$ storage sites and Pt catalyst forming $BaSO_4$ under lean and PtS species under rich conditions, respectively [7,8,14]. In order to regenerate $NO_x$ traps, the catalyst should be heated at high temperature (873 – 973 K) under reducing conditions, which causes another problem "thermal degradation" [7,11,14]. Sintering of platinum, losing barium species due to diffusion through the alumina matrix forming barium aluminate and the reduction of surface area cause thermal deactivation, which mainly limits the durability of the NSR catalyst [7,14].

Since Diesel engines operate at even higher air to fuel ratio (A/F=26), the emissions of CO and $CO_2$ are lower in the exhaust gas compared to gasoline engines. However, the quantity of particulate matter (PM) is high due to either insufficient atomization of the fuel or non-optimal fuel injection. Moreover, $NO_x$ emission also increases due to the high temperature combustion and high injection pressure of the fuel [15]. In order to achieve the emission limits, the following lean $NO_x$ control technologies have been researched and developed:

1. *Selective reduction of $NO_x$ with PM* uses the idea of simultaneous removal of soot and $NO_x$ over the catalyst, i.e. $AB_2O_4$ spinel oxides or perovskite type oxides. Yet, the practical application of this technology for the real diesel engines is not possible due to the inadequate, low-temperature activity of these catalysts [14]. On the other hand, Toyota Motor Corporation developed a new catalyst called "*Diesel Particulate $NO_x$ Reduction (DPNR) 4-way catalyst*", which reduces soot and $NO_x$ simultaneously, with the modified engine control technologies [16,17]. In order to increase the particulate matter collection efficiency and to decrease the pressure drop, the pore diameter of the diesel particulate filter (DPF) is optimized, which is

coated with modified $NO_x$ storage and reduction catalyst comprising Pt/(Ba+K)/($Al_2O_3$+$TiO_2$+Rh/$ZrO_2$) [16]. The oxides, BaO and $K_2O$, hosting Pt do not only store $NO_x$ species but also create the active oxygen, which oxidizes the deposited soot at 573 K [14,16,18]. If the system detects the pressure drop due to the accumulation of soot, the post-injection of fuel is achieved, which results in an increase in temperature, an oxidation of PM and a reduction of $NO_3^-$ species with CO and/or HC at around 723 K [16,18]. Despite the fact that the fresh DPNR system removes 80 % of $NO_x$ and PM in the exhaust gas, it may encounter the problems like engine ash deposit and complexity of data logging [16,18].

2. *Selective catalytic reduction of $NO_x$ with urea* is the commercialized system for heavy-duty vehicles since 2006, which is inspired from the SCR of $NO_x$ by ammonia developed for the abatement of $NO_x$ from stationary sources [14,19,20,21]. In commercial catalysts applied widely, $VO_x$ is the active constituent supported on titania, whose acidity is enhanced with the addition of $WO_3$ and/or $MoO_3$ [21,22]. Urea solution (32.5 % wt) is utilized in order to obtain enough $NH_3$ for the SCR of $NO_x$. Optimum catalytic activity and selectivity are observed for the oxide-based catalyst at temperatures between 523 and 673 K without losing any surface and structure features [19,20]. Nevertheless, above 873 K it is failing to keep the structure and the oxidation of $NH_3$ starts to be the predominant reaction. Moreover, urea-SCR system requires various sensors (for urea, $NH_3$ and $NO_x$), sulfur-free diesel fuel in order to prevent the formation of ammonium sulfates and pre-heating before the process starts [7,19,20,23]. Alternatively, zeolites-based SCR catalysts are also researched to fulfill EuroV and EuroVI emission limits [14,20]. The possible candidates are Fe-ZSM5 and Cu-ZSM5. The former is especially suitable in the temperature range of 673 – 923

K; yet, it suffers from moderate activity and adsorbed ammonia at low temperature due to huge adsorption capacity for ammonia, which inhibits $NO_x$ SCR and causes $NH_3$-slip [20]. The Cu-ZSM5 catalyst shows better activity at low temperature (~500 K); however, it has low hydrothermal stability and oxidizes $NH_3$ at high temperature [20].

3. *Selective catalytic reduction of $NO_x$ with HC* seems to be a promising method, which either utilizes unburned hydrocarbon available in the exhaust gas or proceeds with the help of the fuel injected in front of the catalytic converter to abate $NO_x$ [7,23]. The HC-SCR technology is not commercialized up to now because of the following reasons [8,23,24,25]:
   (i) Low selectivity toward $N_2$.
   (ii) Lack of activity at low temperature, which is around 423 K for the heavy-duty diesel engines.
   (iii) Narrow temperature window to display the highest catalytic activity.
   (iv) Low sulfur and/or water tolerance.
   (v) Low thermal stability of metal nanoparticles (against sintering or sublimation).
   (vi) Difficulty in keeping the catalyst integrity and inherent property under changing working conditions.

   Despite these, intense research on different systems (i.e. Pt-containing systems, Ir-containing catalysts, zeolite-based catalysts and Ag-promoted alumina) is still proceeding in order to improve the weak features in the HC-SCR of $NO_x$. The NO reduction over zeolite-based catalysts by alkanes and/or alkenes under the lean conditions has been found promising if the concentration of water vapor in the exhaust is not high [24], which means that the practical application of zeolite-

based catalysts is impossible. Pt-containing systems show high activity and selectivity at low temperature (~473 K) for HC-SCR of $NO_x$ [25]. The choice of support (i.e. $Al_2O_3$, $SiO_2$) and organic reductant (i.e. $CH_4$, $C_2H_4$, $C_3H_6$, $C_3H_8$, n-$C_4H_{10}$, n-$C_7H_{16}$ etc.) affects the activity and performance, which results in that the direct control of the selectivity towards the $N_2$ formation is challenging [24,25]. Ag-promoted $Al_2O_3$ takes attention due to its high activity, selectivity and relatively wide operating temperature if the Ag loading is kept low [24,25]. The activity of Ag-$Al_2O_3$ catalyst can be shifted to low temperature (~423 K for the typical heavy-duty diesel engine) using longer hydrocarbon chain as reductants and $H_2$ in the exhaust atmosphere [16,23-25]. Nevertheless, the presence of aromatics, which are available in the diesel fuel, affects the activity adversely [24]. This is the major problem to be tackled with. In the literature different metal oxides (e.g. $Al_2O_3$, $TiO_2$, $ZrO_2$, MgO) promoted by additional metal oxides (i.e. Mn, Fe, Co, Ni, Cu, Sn, Ga, In) or metal nanoparticle (i.e. Ag) are reported as active catalysts for the SCR of $NO_x$ with HC [14,25].

The common problem of all introduced technologies is the temporary or permanent diminution of the activity in the presence of $SO_2$ in the exhaust gas.

Sulfur dioxide is an acidic oxide and it can interact with the basic centers on the catalyst surface producing various types of surface sulfates. It is often used as a probe molecule for testing the catalyst basicity [26,27]. However, the interaction of $SO_2$ with cations cannot be excluded. In the $SO_4^{2-}$ group the oxygen atoms exhibit lone pairs of electrons. Thus, coordinate covalent bond can be formed between the transition metal cation (Lewis acid) and the sulfate species (Lewis base)..

Ushikubo stated [28] that the promotion of the $(VO_2)_2(SO_4)/SiO_2$ catalyst with $Nb_2O_5$ suppresses the oxidation of $SO_2$ in the $NH_3$-SCR of $NO_x$ from the industrial stack

gas. Moreover, he mentioned the catalysts, Pd-promoted $Nb_2O_5$ or $Ta_2O_5$, which prevented the $SO_2$ poisoning during the oxidation of HCs under the condition of diesel exhaust [28]. Okazaki et al. reported [29] that the mixed oxides prepared by the co-precipitation of niobium and iron show high activity for the $NH_3$-SCR of $NO_x$ even in the presence of $SO_2$. Ziólek et al. [30] investigated the decomposition of NO over Cu-containing mesoporous MCM-41 samples and concluded that the material (Cu-NbMCM-41-32) can keep its initial activity upon the adsorption of $SO_2$ if Nb is incorporated into the lattice of this material. Furthermore, Ziólek and co-workers also studied the possibility for application of Pt-promoted niobiosilicate ordered mesoporous materials (NbMCM-41) as $NO_x$ storage (NSR) and $C_3H_6$-SCR catalysts [31-33]. The presence of niobium in the MCM-41 matrix enhanced the oxidative properties of the catalyst and NO was adsorbed in the form of nitrite/nitrate species [31-33]. However, the latter species were bound strongly to the surface, which hindered their further interaction with propene. The introduction of zirconium near niobium in the MCM-41 matrix weakened the bond of the nitrites/nitrates with the niobium species and enhanced the SCR selectivity [33].

Nb-containing oxides (as a promoter or a support) and Nb-containing mixed oxides are active for many industrially important reactions, such as oxidative dehydrogenation of alkanes, oxidation and ammoxidation of olefins, cracking of cumene, CO hydrogenation, oxidation of alkanes [34].

Viparelli and coworkers [35] investigated the acidic properties of niobia-supported catalysts with the decomposition of isopropanol and the oxidative dehydrogenation of propane. $Nb_2O_5$-promoted $TiO_2$ catalyst has high selectivity to propene in both reactions, which indicates the presence of strong surface acid sites induced by $Nb_2O_5$ [35]. Hino et al. [36], recently, reported a new solid acid based on mixed oxides of tungsten and niobium. This material shows remarkable activity, which is much higher than that of

tungstated zirconia, for reactions requiring strong Brønsted acidity, such as cracking of alkylbenzenes, dehydration of ethanol [38]. Carrazan et al. [37] concluded from the results of pyridine adsorption that tungstated niobia (9.5 wt% $WO_3$) shows strong surface Lewis and Brønsted acid sites. Because of the high surface acidity, this sample has good selectivity in the formation of butene-2 from butan-2-ol at low temperature (473 K). Reports on $WO_3/Nb_2O_5$ samples [38-40] prepared by incipient wetness of stabilized niobia (calcined at 773 K) state that crystalline $WO_3$ is detected over the niobia support at tungsten contents higher than 3 W/nm$^2$. Martin et al. [41] found that niobia is able to disperse $WO_3$ up to 12.7 W/nm$^2$ in samples prepared by impregnation of hydrated niobium oxide with ammonium metatungstate. This high surface concentration can be due to formation of a solid solution by incorporation of tungsten cations into the niobia support. The samples under ambient conditions exhibit Raman band at 980 cm$^{-1}$ assigned to tetrahedral/octahedral tungsten species [41] or polytungstes of the type $W_{12}O_{40}^{8-}$ [40]. The strong surface acidity combined with increased reducibility of the $WO_x$ phase on niobia, gives rise to large activity in the oxidation of ethylene to acetaldehyde and acetate species, and of isopropanol to acetone [41].

Despite the fact that niobium-containing materials show potential applications in various oxidation and acid-catalyzed reactions [34,42], a little attention has been given to the performance of these catalysts in the SCR of $NO_x$. Regarding the reduction of NO with hydrocarbons in excess oxygen, Hinode and co-workers [43,44] reported that niobium oxide supported on titania is active in the reaction with ethene and propene showing maximum NO conversion of 30 and 62 %, respectively, at about 648 K. Using a mechanical mixture of $Nb/TiO_2$ and $Mn_2O_3$ improves the activity in the SCR with propene and lowers the temperature of maximum NO conversion to 473 – 573 K [45]. Kikuchi and Kumagai investigated the catalytic performance of Nb-promoted $Ag/Al_2O_3$

and $Co/Al_2O_3$ catalysts in the SCR of $NO_x$ in diesel engine exhaust using light gas oil as reductant [45,46]. The catalytic activity of the promoted catalysts was higher than that of the un-promoted ones and the adsorbed amount of sulfur was lower on the Nb-containing catalysts. It has been reported that the deposition of niobium on the surface of alumina lowers the concentration of basic sites [47], which should result in improved resistance to $SO_2$ poisoning.

Niobium-containing catalysts are usually prepared by impregnation using different niobium precursors such as niobic acid, $NbCl_5$, niobium oxalate, ammonium bisoxalato complex of niobium, $(NH_4)_3[NbO(C_2O_4)_2].xH_2O$, and Nb alkoxides [48]. However, there are difficulties in the preparation of niobium catalysts caused by the unacceptable characteristics of most niobium precursors. For example, niobium(V) alkoxides and chloride are moisture sensitive and expensive. Niobium oxalate and its ammonium complex have fairly low prices and are stable. However, the niobium oxalate precursors possess low solubility in aqueous solutions and they may precipitate during the course of catalyst preparation. In addition, these precursors cannot be used directly in the wet preparation of multicomponent systems as most metal ions form relatively insoluble metal oxalates.

Niobium(V) ions easily react with hydrogen peroxide producing peroxide complexes [49-53]. Peroxoniobium compounds are soluble in water [49-53] and are suitable for catalyst preparation. The interaction between the hydrated zirconia and acidified peroxide solution results in the formation of dissolved $ZrO^{2+}$ species [54]. Mixing soluble peroxoniobium complexes and $ZrO^{2+}$ species at a molecular level is beneficial for low-temperature synthesis of zirconia-based solid solutions and results in pure samples.

## I.2. Mechanism of HC-SCR of $NO_x$ on non-zeolitic oxide-based catalysts

Although a $NO_x$ storage system looks more promising from a technical perspective at present, the easiest and inexpensive way for removal of $NO_x$ from the exhaust of lean-burn engines would be the direct HC-SCR technology. The rational design of efficient HC-SCR catalysts active in low-temperature domain requires the understanding of processes at molecular level.

Recent papers of Burch et al. [8,25] reviewed the main features of the HC-SCR mechanism over non-zeolitic oxide-based catalysts. The mechanism of $NO_x$ reduction over oxide-supported platinum group metals involves dissociative adsorption of NO over the reduced noble metal and recombination of two adsorbed nitrogen atoms to molecular nitrogen [26]. The role of hydrocarbons is to remove the adsorbed atomic oxygen originating from NO and $O_2$ dissociation to restore the reduced metal surface [26]. Despite the fact that over noble metals the decomposition mechanism was proven, some authors showed experimental evidence that the mechanisms suggested for oxide-based catalysts (see below) may also be involved for these catalysts [8,25 and the references therein].

Over noble metal-free oxide based catalysts, two $DeNO_x$ mechanisms have been suggested independent of the nature of the catalyst and the nature of the reductant [8,25]. The first pathway (the NO reaction pathway [8,25]) considers the interaction of gaseous or adsorbed $NO_x$ species with the hydrocarbon (HC) [55-74], which leads to the formation of organic nitro compounds ($R–NO_2$) as intermediates [75,55-72]. These intermediates may produce molecular nitrogen directly [56-58] or decompose to other intermediates such as isocyanates [75,55,57,59-68], ammonia [61,62,65,66,68], oximes [64], nitriles [67,68], hydrocarbon oxygenates and adsorbed NO [71-74]. Thomas and coworkers [71,72] proposed that the hydrocarbon oxygenates act as reductants of adsorbed oxygen

produced by decomposition of NO to $N_2$ to restore the corresponding catalytic sites. Kantcheva and Cayirtepe [73] detected formation of methyl nitrite through the intermediacy of nitromethane during the interaction of methane with $NO_x$ species adsorbed on the surface of Pd-promoted tungstated zirconia. The organic nitrite decomposed to adsorbed NO and formates which reacted further to molecular nitrogen. The same mechanism has been proposed in the case of $CH_4$-SCR of NO over $Pd/Zr_2Nb_6O_{17}$ catalyst [74]. The DRIFT results on $Au/\gamma\text{-}Al_2O_3$ [76] indicated that the initiation of the selective reduction of NO with propene involved the oxidation of NO to $NO_2$ followed by coupling of $NO_2$ or its adsorbed species (nitrates or nitrites) with activated $C_3H_6$ to form $R–NO_x$ adsorbed on the support. Although the latter surface compound was not observed, it was proposed that it underwent internal rearrangement and decomposition leading to formation of NCO and CN species which further reacted with $NO+O_2$ or $NO_2$ to nitrogen. The possible role of nitroorganic compounds as intermediates has been supported by the fact that the decomposition of model nitroorganic compounds yielded similar products observed during the SCR reactions [56,61-63,66-70,73].

The second pathway (the hydrocarbon pathway [8,25]) considers the presence of two potential oxidants, $O_2$ and $NO_x$, in the reaction gas mixture or strongly adsorbed $NO_x$ species (nitrites and/or nitrates) on the catalyst surface, which can activate the hydrocarbon producing oxygenates [77-81]. The latter compounds reduce the surface $NO_x$ species to molecular nitrogen. This mechanism is supported by the fact that much higher $DeNO_x$ activity has been observed when using oxygenates as reductants [55,63,82-88].

Scheme 1 (adopted from references [8,25]) summarizes the proposed mechanisms for SCR of $NO_x$ on oxide-based catalysts. In conclusion, it is necessary to point out that no general agreement has been reached on the validity of the discussed mechanisms

[8,25]. The lack of fundamental understanding of the HC-SCR mechanism accounts in part for the unsuccessful development of efficient oxide-based catalysts active in the low-temperature domain.

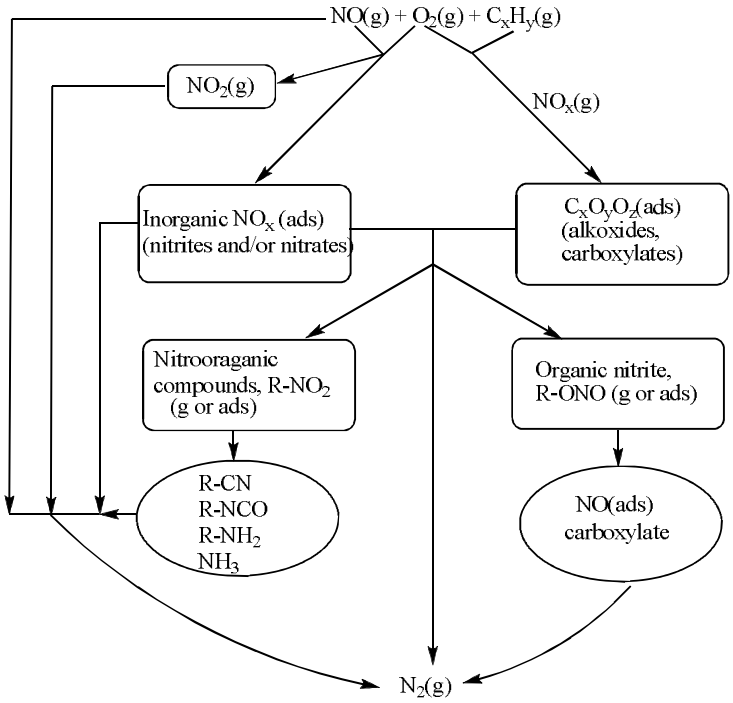


Scheme1. Reaction scheme of the HC-SCR of NO over oxide catalysts (adopted from references [8,25]).

Each of the $DeNO_x$ technologies discussed has weaknesses. The $NO_x$ storage and urea-SCR systems are complex and expensive $NO_x$ aftertreatment strategies. The former has impact on the engine operation and the latter has an impact on the vehicle architecture. The introduction of these two expensive after-treatment technologies in a large scale will increase the price difference existing today between the diesel and gasoline version of a vehicle [8]. Until recently the poor performance below 573 K prevented the commercialization of the oxide-based HC-SCR catalysts. For a car manufacturer, the most attractive method for $NO_x$ removal from the exhaust is through continuous HC-SCR process. Consequently, there is still great interest in finding a direct

HC-SCR catalyst with right properties – high activity in the low-temperature region (423-623 K), good thermal and hydrothermal stability, good sulfur and water tolerance and low cost. The best candidate would be a material with acidic and redox properties which would prevent excessive sulfatation and ensure good activity in moist feeds.

### I.3. Identification of adsorbed $NO_x$ species by FT-IR Spectroscopy

Adsorptions of NO and its coadsorption with $O_2$ lead to formation adsorbed $NO_x$ species, whose identifications are important for the mechanistic study of selective catalytic reduction of NO.

The negatively charged species usually observed on the surface of the catalysts are nitrite ($NO_2^-$) and nitrate ($NO_3^-$) anions. The free nitrite anion has a $C_s$ symmetry and absorption bands due to $\nu_{as}(NO_2)$ and $\nu_s(NO_2)$ modes are at 1330 and 1260 $cm^{-1}$, respectively [89]. When $NO_2^-$ is coordinated by one or two of its oxygen atoms, nitrito species are formed. When $NO_2^-$ is coordinated by its nitrogen atom, nitro compounds are formed. Characteristic IR regions for nitro/nitrito compounds are given in Table 1.

The free nitrate is planar and has a $D_{3h}$ symmetry. It shows three IR active modes: asymmetric stretching ($\nu_3$) at 1430 $cm^{-1}$, out-of-bending ($\nu_2$) at 825 $cm^{-1}$ and in-plane-bending ($\nu_4$) at 722 $cm^{-1}$ [90]. $\nu_1$ is symmetric and is only observed in Raman spectra. After coordination, $\nu_1$ becomes IR active and the degeneracy of $\nu_3$ is removed so that $\nu_3$ splits into two components. The magnitude of the splitting depends on the coordination type of the nitrates. The absorption ranges for nitrates are presented in Table 3.

The IR absorption bands for nitrite and nitrates sometimes overlap in the 1350-1550 $cm^{-1}$ region. In that case, combination bands of nitrates can be used for structural identification. The combination bands of the bridged nitrates are at 2845-2800 $cm^{-1}$ [$\nu_s(N=O) + \nu_s(NO_2)$] and pair bands at 1980-1960 [$\nu_s(NO_2) + \delta(ONO)$] and 1900-1890

$cm^{-1}[\nu_s(NO_2) + \delta(ONO)]$. Bidentate nitrates produce combination bands in the region of 2600 $cm^{-1}$ $[\nu_s(N=O) + \nu_s(NO_2)]$ and pair of bands at 1755 and 1700 $cm^{-1}$ $[\nu_s(NO_2) + \delta(ONO)]$ [90].

Stability of adsorbed $NO_x$ species can give information about their nature. The noncharged species, e.g. NO, $(NO)_2$, $NO_2$, $N_2O_3$ and $N_2O_4$, are generally weakly adsorbed and easily removed from the surface upon evacuation at room temperature. On the other hand charged species, e.g. $NO^+$, $NO_2^-$, $NO_3^-$, $NO^-$ are stable. They need to be heated at elevated temperatures in order to desorb from the surface. The nitro species are more stable than the nitrito species and bridged and bidentate nitrates are more thermally stable than the monodentate nitrates.

**Table 3:** Spectral characteristics of $NO_x$ species observed on the metal oxides [69, 89-91].

| $NO_x$ Species | Vibration Modes | Wavenumbers ($cm^{-1}$) |
|---|---|---|
| Free nitrite ion, $NO_2^-$ | $\nu_{as}(NO_2)$<br>$\nu_s(NO_2)$<br>$\delta(ONO)$ | 1250<br>1335<br>830 |
| Nitro, 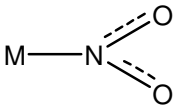 | $\nu_{as}(NO_2)$<br>$\nu_s(NO_2)$<br>$\delta(ONO)$ | 1370-1470<br>1320-1340<br>820-850 |
| Nitrito, 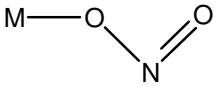 | $\nu(N=O)$<br>$\nu(NO)$<br>$\delta(ONO)$ | 1400-1485<br>1050-1100<br>820-840 |
| Chelated Nitrito, 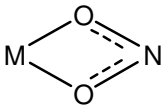 | $\nu_{as}(NO_2)$<br>$\nu_s(NO_2)$<br>$\delta(ONO)$ | 1270-1390<br>1170-1225<br>840-860 |
| Bridging nitro, 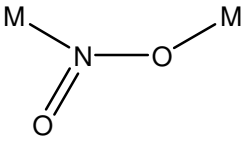 | $\nu_{as}(NO_2)$<br>$\nu_s(NO_2)$ | 1390-1520<br>1180-1260 |
| Bidentate nitro | $\nu_{as}(NO_2)$<br>$\nu_s(NO_2)$ | 1390-1520<br>1180-1260 |
| Free nitrate ion, $NO_3^-$ | $\nu_{as}(NO_2)$ | 1430 |
| Monodentate nitrate, 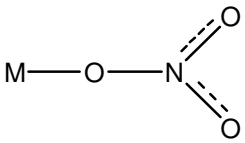 | $\nu_{as}(NO_2)$<br>$\nu_s(NO_2)$<br>$\nu(NO)$ | 1450-1570<br>1250-1330<br>970-1035 |
| Bidentate nitrate, 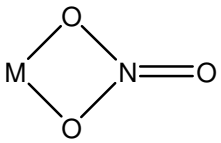 | $\nu_{as}(NO_2)$<br>$\nu_s(NO_2)$<br>$\nu(NO)$ | 1200-1310<br>1003-1040<br>1500-1620 |
| Bridged nitrate, 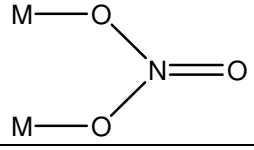 | $\nu_{as}(NO_2)$<br>$\nu_s(NO_2)$<br>$\nu(NO)$ | 1200-1260<br>1000-1030<br>1590-1660 |

## I.4. Objective of the study

The aim of the thesis is (i) to develop synthetic routes for novel niobium-containing solid acids and (ii) to investigate the role of niobium for improving the sulfur tolerance of catalysts for selective catalytic reduction of NO with hydrocarbons in excess oxygen and (iii) to study the potential of the niobium-containing solid acids for alcohol transformations.

This study is comprised of three parts:

1. In the first part, synthesis methods are developed for the synthesis of new nanostructured solid acids based on niobium-zirconium and tungsten-niobium. The synthesized materials are characterized structurally by XRD, Micro-Raman spectroscopy and DR-UV-vis spectroscopy with respect to compositional changes and/or calcination temperatures. By means of in situ FT-IR spectroscopy the acidic sites developed on the surface of samples after each modification are probed by the adsorption of 2,6-dimethylpyridine and/or CO.
2. In the second part, the samples possessing the highest concentration of Brønsted acid sites are investigated as catalysts for the selective catalytic reduction of $NO_x$ with propene. In order to elucidate the reaction mechanism, in situ FTIR investigations of the adsorption and co-adsorption of the reagents have been carried out and their interactions were followed at various temperatures. Furthermore, what kind of surface $SO_x$ species are formed and how the $NO_x$ and $C_xH_yO_z$ compounds are affected by the presence of $SO_2$ are examined in order to make conclusions about the $SO_2$ poisoning effect.
3. In the last part, by means of in situ FTIR spectroscopy the potential of the samples with the highest Brønsted acidity is evaluated as catalysts for other reactions like dehydrogenation or oxidative dehydration of alcohols.

# II. Experimental

## II.1. Sample Preparation

Amorphous $ZrO_x(OH)_{4-2x}$ was prepared by hydrolysis of $ZrCl_4$ (Merck, for synthesis) with concentrated (25 %) solution of ammonia as already described [92]. After washing (negative test for $Cl^-$ ions) the precipitate, it was dried at 383 K in air for 24 h. According to XRD, the solid (specific surface area of 298 $m^2/g$) was amorphous. This material (denoted as $ZrO_2$-383) was used to prepare the tungsten- and niobium-containing samples.

### II.1.1. $Nb_2O_5/ZrO_2$

A solution of the complex $[Nb_2(O_2)_3]^{4+}$ was prepared according to the procedure described in reference [52]. The starting Nb(V) precursor, $(NH_4)(C_2O_4)_2NbO.xH_2O$ (Aldrich, x = 19.15), was added under stirring in small portions to a 30 % $H_2O_2$ solution (Merck, without stabilizer) acidified to a pH ~ 0.5 by concentrated $HNO_3$ and then the solution was heated for 1 h at 323 K. Hydrated zirconia was impregnated for 24 h, under stirring, at room temperature with the peroxoniobium(V) solutions taken in concentrations ensuring $ZrO_2$:$Nb_2O_5$ mole ratios ranging from 150:1 to 4:1. The amount of the hydrated zirconia was determined according to the weight loss after the calcination for 2 h at 873 K. The liquid was removed from the suspension by gentle evaporation at 343 K and the solid was calcined under static air for 2 h at 623 K and 2 h at 873 K (heating rate 10K/min). The samples obtained from the niobium(V) peroxo precursor are denoted as xNbZ-P, where x stands for the amount of niobium in wt %.

For comparison purposes a $Nb_2O_5$-$ZrO_2$ sample containing $ZrO_2$:$Nb_2O_5$ mole ratio of 5:1 was synthesized by impregnating hydrated zirconia with an aqueous solution of

ammonium niobium oxalate. This sample (labeled as 30NbZ-O) was dried and calcined according to the procedures described above. The nominal niobium content and the surface areas of selected $Nb_2O_5$-$ZrO_2$ samples are summarized in Table 4.

**Table 4.** Composition and surface area of selected $Nb_2O_5$-$ZrO_2$ samples

| Sample | Nb wt% | Mole ratio $ZrO_2$:$Nb_2O_5$ | Surface area, $m^2/g$ |
|---|---|---|---|
| $ZrO_2$ | - | - | 25 |
| 5NbZ-P | 5 | 30:1 | 28 |
| 10NbZ-P | 10 | 15:1 | 18 |
| 15NbZ-P | 15 | 10:1 | - |
| 19NbZ-P | 19 | 8:1 | 22 |
| 25NbZ-P | 25 | 6:1 | 42 |
| 30NbZ-P | 30 | 5:1 | 37 |
| 32NbZ-P | 32 | 4.8:1 | - |
| 30NbZ-O | 30 | 5:1 | - |

Niobium pentaoxide was obtained by the precipitation of $Nb_2O_5.nH_2O$ with a concentrated (25%) solution of ammonia from an aqueous solution of ammonium niobium oxalate at pH = 8.2. The precipitate was separated from the solution, washed with deionized water (negative test for oxalate ions) and calcined for 2 h at 873K. A sample of zirconia (denoted as $ZrO_2$-P) was prepared by suspending hydrated zirconia in $H_2O_2$ (30%) for 24 h under stirring. Then the material was filtered off, dried and calcined for 2 h at 873 K. Monoclinic zirconia was obtained by the calcination of hydrated zirconium oxyhydroxide at 873 K for 2 h.

II.1.2. $WO_3/Nb_2O_5$

Niobium(V) peroxo solutions with different concentrations were prepared as described above. To these solutions various amounts of solid ammonium metatungstate (AMT, $(NH_4)_6H_2W_{12}O_{40}.18H_2O$) were added ensuring the desired $Nb_2O_5$:$WO_3$ mole ratios (Table 5). The liquid was evaporated by a gentle heating followed by calcination of the solid substances at various temperatures for 2 h. The $WO_3$-$Nb_2O_5$ samples are denoted as xWNy, where x indicates the amount of $WO_3$ in wt% and y stands for the calcination temperature.

$WO_3$ was prepared by dissolving $(NH_4)_6H_2W_{12}O_{40}.18H_2O$ in 30 % $H_2O_2$. After the evaporation of the liquid the solid material was calcined at 773 K for 2 h.

**Table 5.** Nominal composition of the $WO_3$-$Nb_2O_5$ samples

| Sample | $WO_3$ wt % | $Nb_2O_5$:$WO_3$ mole ratio |
|---|---|---|
| 10WN | 10 | 7.85:1 |
| 20WN | 20 | 4:1 |
| 40WN | 40 | 1.3:1 |
| 60WN | 60 | 0.6:1 |
| 80WN | 80 | 0.2:1 |

### II.2. Surface area measurements, X-ray diffraction, DR-UV-vis spectroscopy and UV-vis spectroscopy

The BET surface areas of the samples were measured by nitrogen adsorption at 77 K using Monosorp apparatus from Quantachrome Corporation, Autosorp-1-C/MS. Prior the measurements, the samples were dehydrated under vacuum (~$10^{-2}$ torr) for 2 h at 623K.

XRD analysis was performed on a Rigaku Miniflex diffractometer with Ni-filtered Cu $K_\alpha$ radiation ($\lambda$ = 1.5405Å) under ambient conditions. The scan speed was 2°/min.

DR-UV-vis spectra were obtained under ambient conditions with a fiber optic spectrometer AvaSpec-2048 (Avantes) using WS-2 as a reference. The DR-UV-vis spectra were smoothed before the calculation of absorption edge energy.

UV-vis spectra of liquid samples were recorded using a Varian Cary 5 double beam spectrophotometer with a resolution of 2 nm over a wavelength range from 600 to 200 nm in the absorbance mode.

### II.3. Micro-Raman spectroscopy

The micro-Raman spectra were recorded on a LabRam confocal Raman microscope with a 300 mm focal length. The spectrometer is equipped with both HeNe laser operated at 20 mW, polarized 500:1 with a wavelength of 623.817 nm, and dipole-pumped solid state laser operated at 50 mW, polarized 100:1 with a wavelength of 523.1 nm, and a 1024x256 element CCD camera. The signal collected was transmitted through a fiber optic cable into a grating with 600 g/mm spectrometer.

## II.4. FT-IR spectroscopy

The FT-IR spectra were recorded using a Bomem Hartman & Braun MB-102 model FT-IR spectrometer with a liquid-nitrogen cooled MCT detector at a resolution of 4 $cm^{-1}$ (128 scans). The FT-IR spectra were smoothed without losing any features.

### II.4.1. Experimental Setup

The IR cell allowed recording of the spectra at ambient and elevated temperatures (with $BaF_2$ windows). The sample holder of the cell can be moved up and down relatively to the light beam, which gives the possibility for the subtraction of the gas phase spectrum when needed. The IR cell is connected to a vacuum/adsorption apparatus.

### II.4.2. Activation of the Samples

The self-supporting discs (0.01 - 0.035 $g/cm^2$) were activated in the IR cell by heating for 1 h in a vacuum at 723 K and in oxygen (100 mbar, passed through a trap cooled in liquid nitrogen) at the same temperature, followed by evacuation for 1 h at 723 K.

The spectra of the activated sample were taken at high temperature and room temperature, which were used as background references. The spectra of the samples that were subjected to heat treatments at elevated temperatures were recorded at those temperatures. The high temperature background reference was used in the subtraction of the spectra taken at high temperatures and correspondingly the room temperature background reference was used for the spectra registered below 423 K.

II.4.3. Surface Acidity of the Samples

The surface acidity of the samples was investigated by in situ FT-IR spectroscopy using 2,6-dimethylpyridine (2,6-DMP or lutidine), CO and NO as probe molecules. The 2,6-dimethylpyridine (lutidine, Sigma-Aldrich, redistilled) adsorption test was carried out by the admission of 2.4 mbar of the base into the IR cell and left in contact with the sample for 10 min. The excess 2,6-lutidine was then evacuated at room temperature for 15 min, followed by desorption of the strongly bonded base fraction in the temperature range 150 – 723 K. The CO (99.95%, BOC) used was passed through a trap cooled by liquid nitrogen before admission to the IR cell. The purity of the NO gas (Air Products) was 99.9%.

II.4.4. Reactivity of the surface species formed upon room temperature adsorption of $NO+C_3H_6+O_2$ mixture on the samples

3 mbar of $C_3H_6$, 10 mbar of $O_2$ and 18 mbar of NO were premixed in the flange at room temperature; afterwards the gas mixture was admitted to the IR cell. After reaching the equilibrium between the gas phase and the surface species, the gas phase was evacuated for 10 min. Then, the closed IR cell was heated from 298 K to 623 K in order to follow the reactivity of the surface species. The duration time was 15 min for each temperature level.

**II.5. Catalytic activity measurements**

The catalytic tests of $NO_x$ reduction by propene were carried out in a tubular flow reactor (quartz glass) with an internal diameter of 6.0 mm. The catalyst sample was loaded in the form of particles with irregular shape and size of 0.6 – 1.2 mm. The gas analysis was performed using on-line analyzers as follows: $NO/NO_2/NO_x$ (Environment

S.A., Model 31 M), $CO/CO_2/O_2$ (Maihak), THC (ThermoFID). Gas supply section was based on mass-flow controllers manufactured by Bronkhorst. The catalyst was tested at GHSV of 10 000 $h^{-1}$. The reaction mixture used in the catalytic test contained 245 ppm of $NO_x$ ($NO/NO_2$ = 1.77), 504 ppm $C_3H_6$, 9 vol. % of oxygen and nitrogen for balance to 100 vol. %. The steady-state test was made upon step-wise increase of the reaction temperature and holding at each temperature (approximately 1.5 h) to reach a constant conversion value. The conversion degrees of $NO_x$ (taken as a measure of the catalytic activity) and propene were calculated using the inlet and outlet concentrations. The $SO_2$ poisoning experiment was performed with 56 ppm of $SO_2$ in the inlet and under fast poisoning conditions (200 ppm of $SO_2$ in the inlet) at temperature corresponding to the maximum $NO_x$ conversion. The effect of $H_2O$ vapour was tested with 1.2 vol % of $H_2O$ in the inlet at temperature corresponding to the maximum $NO_x$ conversion.

# III. Results and Discussion

## III.1. Structural Characterization and Surface Acidity of Solid Acids based on Zirconia and Niobia

In this part we describe the structural characterization and the surface acid properties of solid acids based on zirconia and niobia.

### III.1.1. $Nb_2O_5/ZrO_2$

Here, we describe the results of structural characterization of $Nb_2O_5$, $ZrO_2$ and $Nb_2O_5$-$ZrO_2$ oxide system. The mixed oxides were prepared using acidic solutions of the peroxoniobium(V) complex, $[Nb_2(O_2)_3]^{4+}$.

#### *III.1.1.1. Niobium species in the precursor solutions*

Fig. 2 shows the UV-Vis spectra of aqueous solutions of $(NH_4)(C_2O_4)_2NbO.xH_2O$ with different concentrations. The absorption at 270 nm indicates the presence of the 2:1 oxalato-niobium complex $[Nb(OH)_2(C_2O_4)_2]^-$ [49].

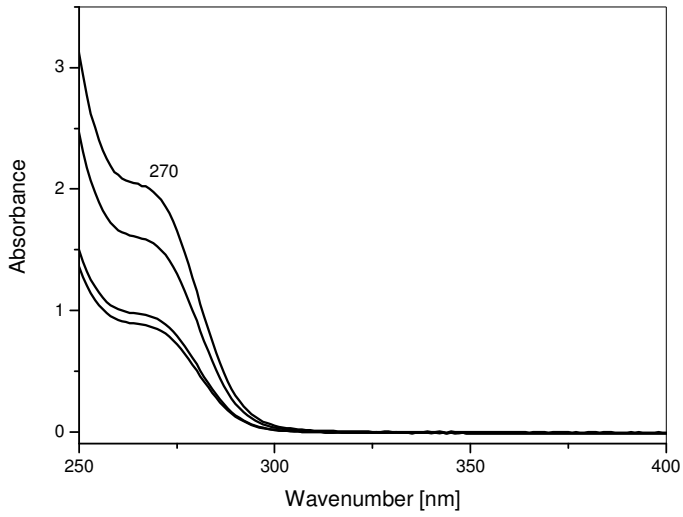


Fig. 2. UV-vis spectra of aqueous solutions of $(NH_4)(C_2O_4)_2NbO.xH_2O$ with different concentrations.

The UV-vis spectra of the peroxo solutions with different concentrations of the Nb(V) are shown in Fig. 3. The color of the solutions is yellow. Three different Nb(V) peroxo complexes with peroxo:Nb mole ratios of 1:1, 1:2 and 2:3 are reported [49-51]. The absorption bands with maxima at 310 – 321 nm observed in Fig. 3 are characteristic of the 2:3 complex and indicate that the Nb(V) peroxo solutions contain the ions $[Nb_2(O_2)_3]^{4+}$. The 1:1 and 1:2 complexes absorb below 290 nm [49-51].

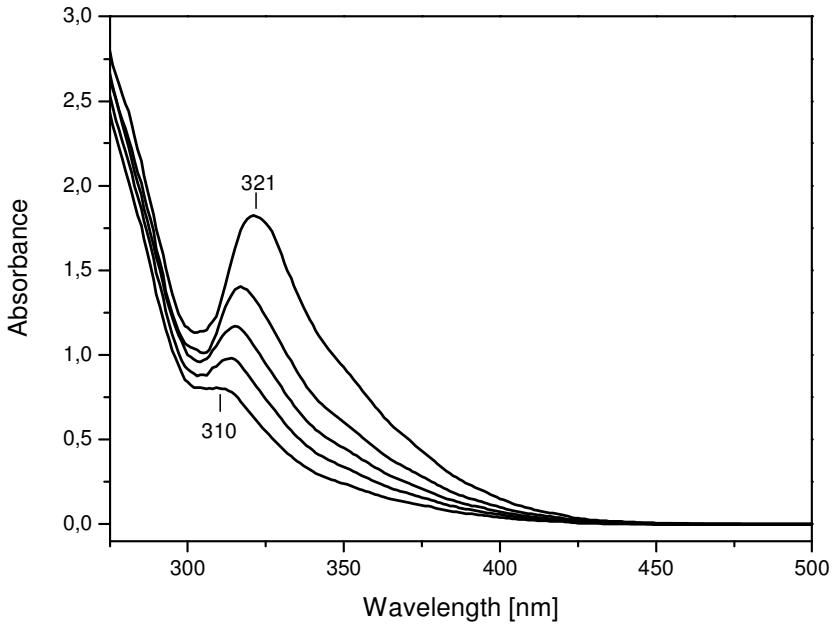


Fig. 3. UV-vis spectra of peroxo solutions with different concentrations of the Nb(V).

The Raman spectra of the of the Nb(V) oxalate (spectrum a) and peroxo (spectrum b) precursor solutions used for the preparation of the 25NbZ-P sample are shown in Fig. 4. Coordinated oxalate ion exhibits vibrational modes between 1750 and 1200 $cm^{-1}$ corresponding to the carboxylic groups [90]. In Fig. 4, spectrum a, four bands are observed in this region and they are attributed to $C_2O_4^{2-}$ ions coordinated in bidentate and monodentate modes (see Table 6). The intensities of the oxalate bands in the spectrum of the peroxo precursor (Fig. 4, spectrum b) are very low indicating that decomposition of the $[Nb(OH)_2(C_2O_4)_2]^-$ complex has occurred. The intensities of these bands remain

constant within a period of 30 min of the decomposition process. The signals at 1050 and 720 $cm^{-1}$ belong to the $NO_3^-$ ions arising from the dissociation of nitric acid used for pH adjustment. The strong band at 879 $cm^{-1}$ is typical of the $\delta_s$(O–O) mode of hydrogen peroxide present in excess. The characteristic ν(O–O) vibrations of the Nb(V) peroxo complexes fall between 890 and 800 $cm^{-1}$ [52,53] and are not visible because of the strong $H_2O_2$ band.

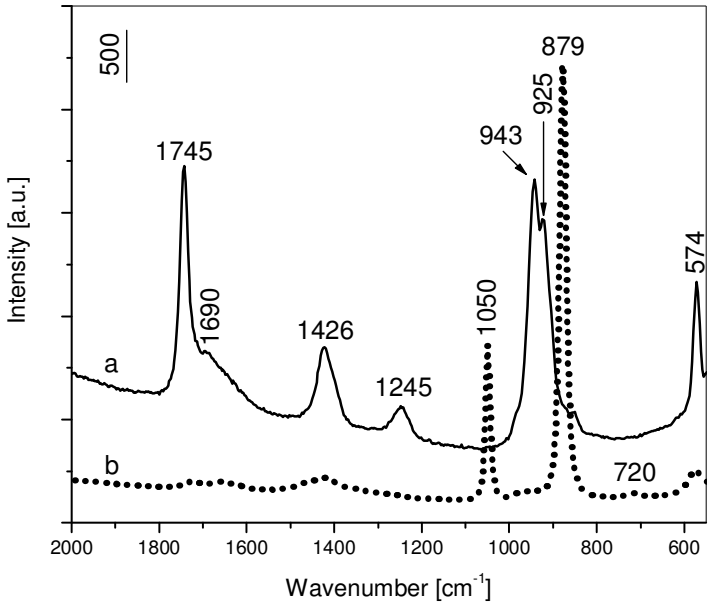


Fig. 4. Raman spectra of the Nb(V) oxalato (a) and peroxo (b) precursor solutions.

Based on these data, the following processes of decomposition of the Nb(V) oxalato complex in excess $H_2O_2$ can be proposed:

$$[NbO(C_2O_4)_2]^- + H_2O \rightarrow [Nb(OH)_2(C_2O_4)_2]^-$$

$$2[Nb(OH)_2(C_2O_4)_2]^- + 7H_2O_2 + 6H^+ \rightarrow [Nb_2(O_2)_3]^{4+} + 8CO_2 + 12H_2O$$

These processes lead to the formation of the peroxo precursor complex $[Nb_2(O_2)_3]^{4+}$.

As shown earlier [54], the dissolution of $(NH_4)_6H_2W_{12}O_{40}.18H_2O$ in acidic $H_2O_2$ (30 %) does not lead to formation of W(VI) peroxo complex and the solution contains the metatungstate ion, $[(H_2)W_{12}O_{40}]^{6-}$.

**Table 6.** Assignments of the Raman bands observed in the spectra shown in Fig. 4.

| Species | Band position ($cm^{-1}$) | Mode |
|---|---|---|
| $C_2O_4^{2-}$ (bidentate) | 1742<br>1426<br>574 | $\nu_{as}$(C=O)<br>$\nu_s$(C=O)<br>$\delta$(O–C=O) |
| $C_2O_4^{2-}$ (monodentate) | 1690<br>1245<br>574 | $\nu_{as}$(C=O)<br>$\nu_s$(C=O)<br>$\delta$(O–C=O) |
| Nb=O<br>Nb-OH | 943<br>925 | $\nu$(Nb=O)<br>$\nu$(Nb–O) |
| $H_2O_2$ | 879 | $\delta$(O–O) |

*III.1.1.2. Structural characterization of the calcined samples*

The XRD patterns of $ZrO_2$ prepared by calcination of hydrated zirconium oxyhydroxide at 873 K (Fig. 5) correspond to monoclinic zirconia (ICDD Card No 37-1484). The treatment of $ZrO_x(OH)_{4-2x}$ with solution of $H_2O_2$ (30%) followed by drying and calcination at 873 K leads to formation of a mixture of tetragonal (ICDD Card No 17-0923) and monoclinic zirconia. Kantcheva and Koz reported earlier [54] that the interaction of hydrated zirconia with $H_2O_2$ solution results in increase in the amount of OH groups and formation of surface Zr(IV) peroxo complex. The increased amount of OH groups in the amorphous material favors the stabilization of the tetragonal polymorph [93,94]. The crystallographic modification of $Nb_2O_5$ synthesized corresponds to the

pseudo-hexagonal TT-phase (ICDD Card No 27-1312). The XRD patterns of the 30NbZ-O sample reveal the presence of two phases – niobia and tetragonal zirconia. In contrast, the $Nb_2O_5$-$ZrO_2$ sample with the same $ZrO_2$:$Nb_2O_5$ mole ratio prepared from the Nb(V) peroxo precursor

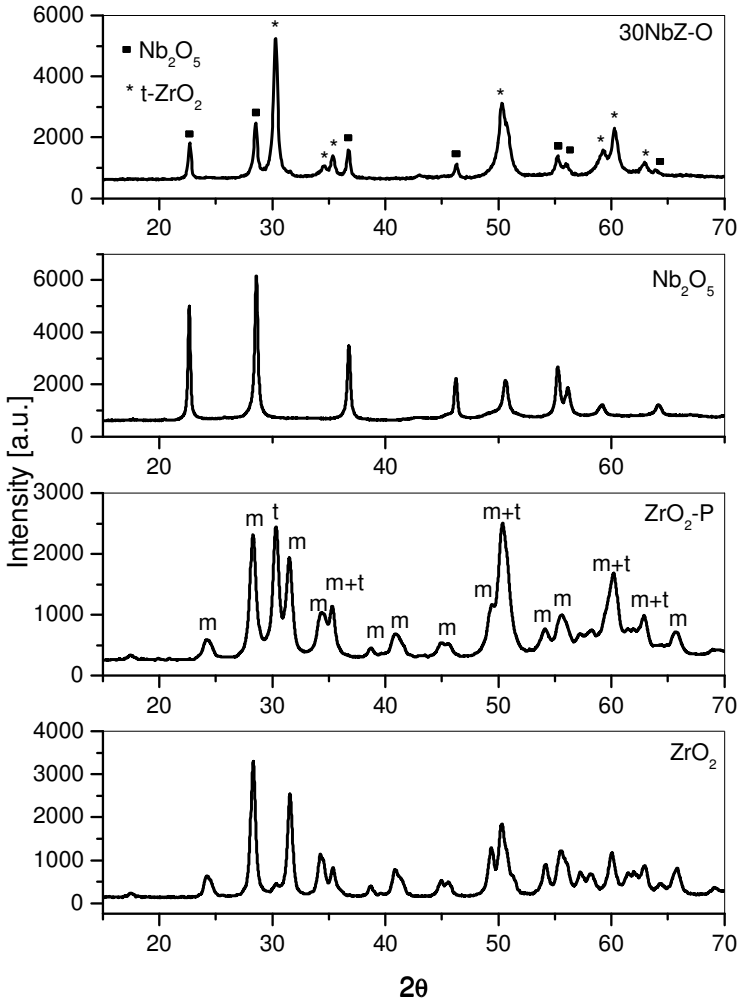


Fig. 5. XRD patterns of $ZrO_2$, $ZrO_2$-P, $Nb_2O_5$ and 30NbZ-O samples.
(m: monoclinic; t: tetragonal)

(sample 30NbZ-P) does not contain phase of $Nb_2O_5$. All diffraction peaks of the 30NbZ-P and 25NbZ-P samples (Fig. 6) are indexed as $Zr_6Nb_2O_{17}$ (ICDD Card No 09-0251). The diffraction patterns in Fig. 6 show that the increase in the Nb content causes the stabilization of tetragonal zirconia. The phase composition of the 15NbZ-P sample

corresponds to a mixture of tetragonal zirconia and $Zr_6Nb_2O_{17}$. For the 32NbP-Z sample (mole ratio $ZrO_2$:$Nb_2O_5$ = 4.8:1) three phases, $Nb_2O_5$, $Zr_6Nb_2O_{17}$ and tetragonal zirconia, are detected. According to XRD, the stoichiometric mixed oxide, $Zr_6Nb_2O_{17}$, is detected at $ZrO_2$:$Nb_2O_5$ mole ratios ranging from 10:1 to 5:1. The formation of the $Zr_6Nb_2O_{17}$ is favored by the partial solubility of hydrated zirconia in $H_2O_2$ solution [54].

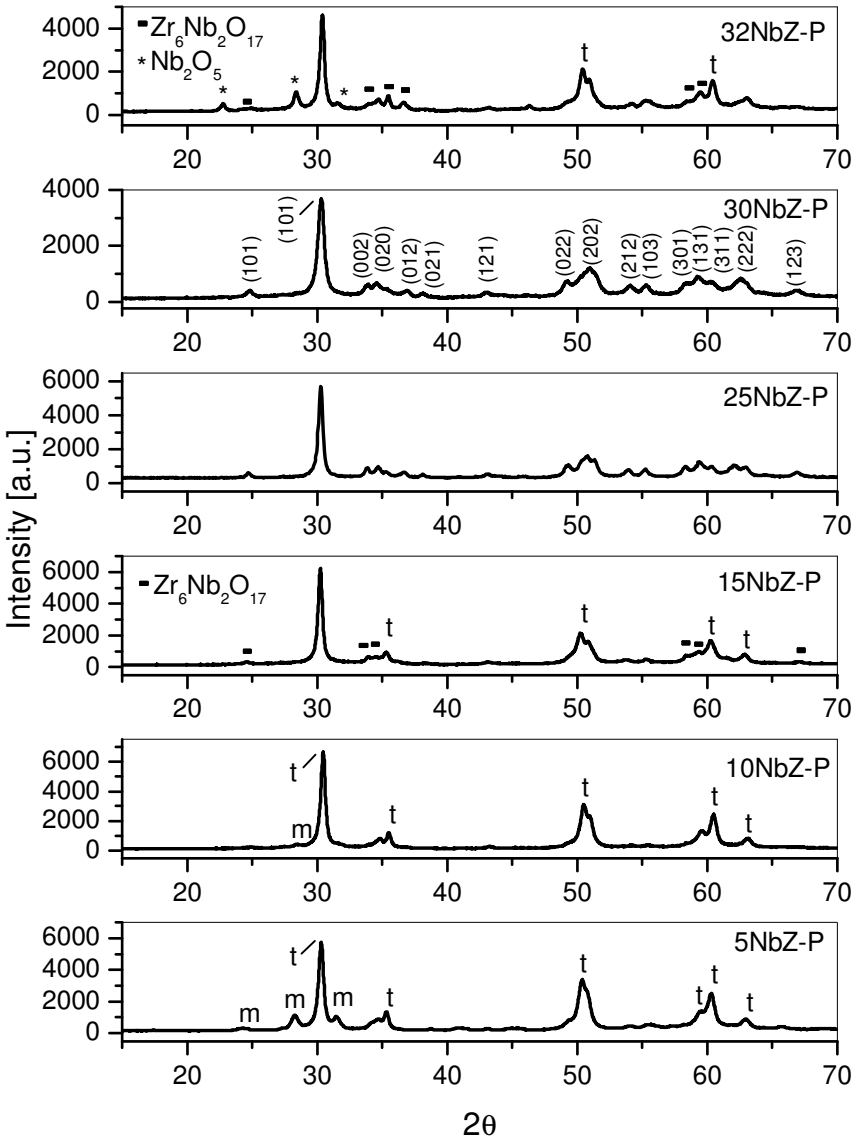


Fig. 6. XRD patterns of samples prepared from the peroxoniobium(V) precursor.
(m: monoclinic; t: tetragonal)

The $ZrO_2$-$Nb_2O_5$ solid solutions with $ZrO_2$:$Nb_2O_5$ mole ratios ranging from 5.1:1 to 10:1 have been reported in the literature [95]. These materials were synthesized by a ceramic process from mixtures of zirconia and niobia powders at temperatures exceeding 1270 K. Kominami et al. [96] obtained a single phase of $Zr_6Nb_2O_{17}$ directly by a glycothermal method. Recently, Lu et al. [97] synthesized crystallized mesoporous $Zr_6Nb_2O_{17}$ using block copolymer surfactant and chlorides of Zr(IV) and Nb(V).

*III.1.1.3. Micro-Raman spectroscopy*

Fig. 7 shows the Raman spectra of $ZrO_2$ (monoclinic), $Nb_2O_5$ (TT), 30NbZ-O and xNbZ-P samples. The spectrum of $Nb_2O_5$ contains strong band at 700 $cm^{-1}$ corresponding to Nb—O—Nb stretching vibrations of ordered niobia polyhedra [98]. The Raman band with maximum at 695 $cm^{-1}$ observed in the spectrum of the 30NbZ-O sample is due to bulk $Nb_2O_5$ [99]. In agreement with the XRD data, this signal is indicative of the presence of $Nb_2O_5$ crystallites on zirconia. The broadening of the band at 695 $cm^{-1}$ is associated with the stretching modes of Nb—O—Nb bonds of hydrated surface $NbO_x$ species [99]. The weak signal between 1000 – 800 $cm^{-1}$ in the spectrum of the 30NbZ-O sample could be attributed to terminal Nb=O bonds of surface polyniobate structures with different degree of hydration. The band at 695 $cm^{-1}$ is absent in the spectra of the xNbZ-P samples. This confirms that these materials do not contain crystalline $Nb_2O_5$. This is in agreement with the fact that the structure of $Nb_2Zr_{x-2}O_{2x+1}$ solid solutions (x = 7.1–12) is described as a superstructure made up of subcells of metal and oxygen atoms allowing the accommodation of various Nb concentrations [95]. The samples prepared from the peroxo precursor exhibit a broad signal between 1000 and 700 $cm^{-1}$ and poorly resolved shoulder at about 590 $cm^{-1}$ observed in the Nb-containing zirconia. These bands become more distinct with increase in the Nb content and are attributed to $NbO_x$ polyhedra of

$Zr_6Nb_2O_{17}$. The Raman spectra in the 700 – 400 $cm^{-1}$ region of the samples containing the single phase of $Zr_6Nb_2O_{17}$ (25NbZ-P and 30NbZ-P), exhibit bands at 664-655, 590 (broad), 440 – 430 and 380 $cm^{-1}$, which differ from those of tetragonal $ZrO_2$ [100]. The Raman spectrum of monoclinic zirconia has a band at 475 $cm^{-1}$, which is stronger than the band at 634 $cm^{-1}$ (Fig. 7) and the reverse is observed for the tetragonal phase [100] (the band at 640 $cm^{-1}$ is stronger than that at 470 $cm^{-1}$). The spectra of the xNbZ-P samples (Fig. 7) show that the increase in the niobium content causes: (i) shift of zirconia bands and (ii) appearance of a new signal at 380 $cm^{-1}$. Most probably these changes are associated with the formation of Zr–O–Nb linkages.

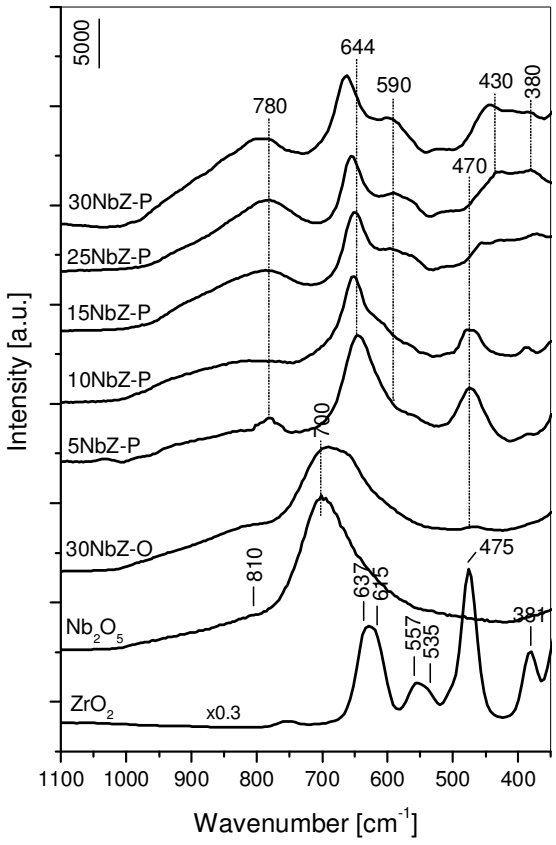


Fig. 7. Raman spectra of $Nb_2O_5$, 30NbZ-P and xNbZ-P samples.

*III.1.1.4. DR-UV-vis spectroscopy*

The DR-UV-vis spectra of the samples (Fig. 8) contain broad absorption in the 290 – 325 nm region associated with $O^{2-} \rightarrow Nb^{5+}$ charge transfer transition [98,101,102]. This band shifts to lower energy with increase in the niobium loading.

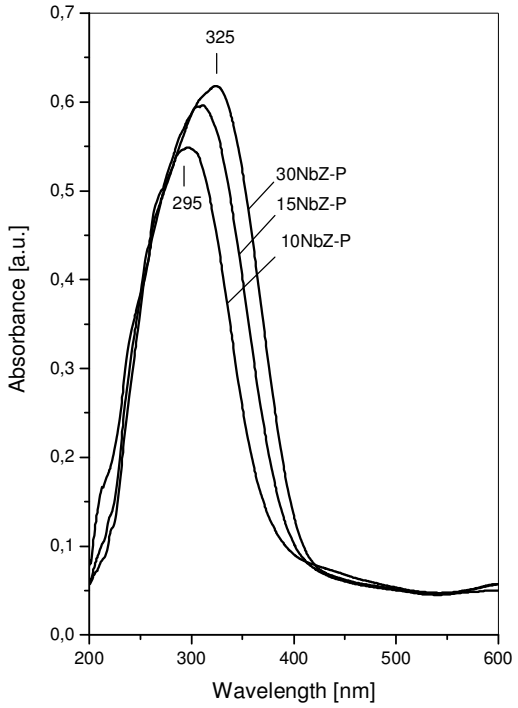


Fig. 8. DR-UV-vis spectra of xNbZ-P samples.

The absorption edge energies of the samples with $ZrO_2$:$Nb_2O_5$ mole ratios from 150:1 to 4:1 (from 1.3 to 33.5 mol % of Nb) decrease linearly with the Nb content (Fig. 9) i. e. with the increase in the amount of $Zr_6Nb_2O_{17}$ formed. For the samples with $ZrO_2$:$Nb_2O_5$ mole ratios less than 5:1 the absorption edge energy remains close to that of the stoichiometric $Zr_6Nb_2O_{17}$ (3.25 eV). However, the degree of polymerization of the $NbO_x$ domains in the structure of $Zr_6Nb_2O_{17}$ cannot be established because long-range metal ordering is negligible in this compound and niobium is randomly distributed over the metal sites [95].

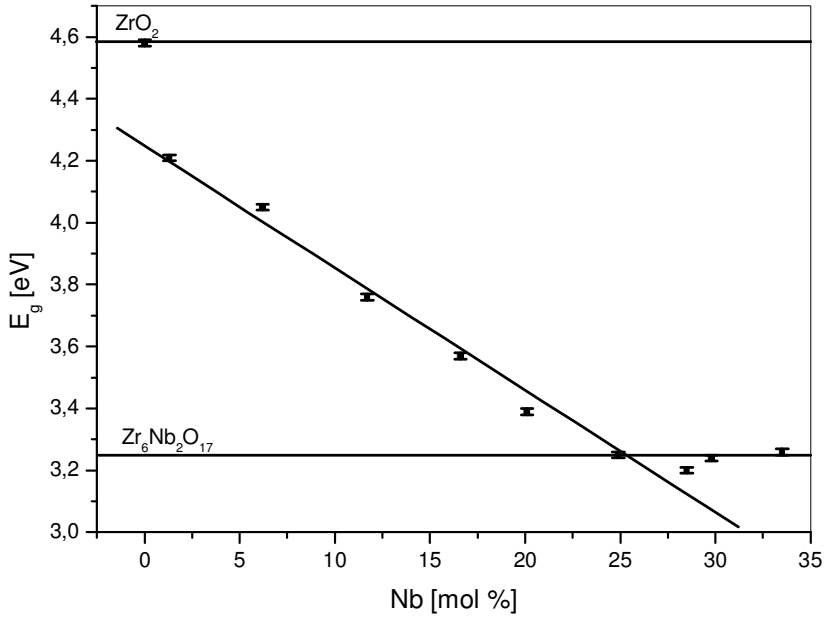


Fig. 9. Absorption edge energies of the xNbZ-P samples (Error: ±0.01).

*III.1.1.5. Brønsted acidity*

The FT-IR spectra of the activated samples in the ν(OH) stretching region are shown in Fig. 10A. According to the XRD data the $ZrO_2$-P sample represents a mixture of monoclinic and tetragonal zirconia. The spectrum of the $ZrO_2$-P sample contains sharp bands at 3675 and 3638 $cm^{-1}$, which are typical of tribridged OH groups observed in samples containing both monoclinic and tetragonal zirconia [103]. The intensities of the isolated $Zr^{4+}$–OH groups decrease with increase in the Nb loading with simultaneous development of a wide signal, which extends from 3600 $cm^{-1}$ down to 2400 $cm^{-1}$. The latter absorption is ascribed to the ν(OH) stretching vibrations of H-bonded surface hydroxyls.

The Brønsted acidity of the samples has been tested by the adsorption of lutidine. This probe molecule, because of its higher basicity and steric hindrance of the methyl groups, is more sensitive to Brønsted acidity than pyridine [104,105]. Fig. 10B compares

the spectra of $ZrO_2$-P and xNbZ-P samples obtained after the admission of 2.4 mbar of the base followed by evacuation for 15 min at 423 K. The broad absorption with poorly resolved maxima at 1575, 1565 and 1550 $cm^{-1}$ detected on the $ZrO_2$-P sample characterizes lutidine adduct with Lewis acid sites [102,106,107]. The former two bands correspond to the 8a mode of the adsorbed base coordinated to two types of $Zr^{4+}$ ions differing in their coordinative unstauration. This assignment agrees with the result of CO adsorption (see below, Fig. 11, spectrum a). The 8b partners of the bands at 1575 and 1565 $cm^{-1}$ overlap and are located at 1550 $cm^{-1}$. The NbZ-P samples with Nb loading between 5 and 19 wt %, in addition to the absorption characteristic of Lewis acidity, contain bands at 1642 and 1627 $cm^{-1}$ whose intensities grow with the Nb loading. These absorptions correspond to the 8a and 8b ring vibrational modes, respectively, of protonated lutidine species (lutidinium cation) [102,106,107] and testify the existence of

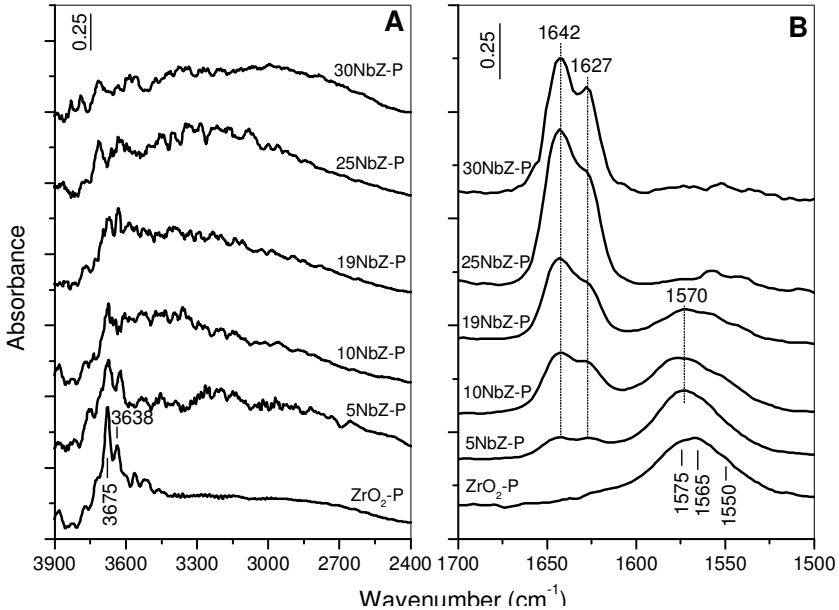


Fig. 10. Panel A: FT-IR spectra of the activated samples. Panel B: FT-IR spectra of lutidine (2.4 mbar) adsorbed at room temperature for 10 min followed by evacuation at 423 K for 15 min.

Brønsted acid sites on the surface of the NbZ-P samples. The amount of the Lewis acid sites decrease with the increase of the Nb content and for the samples containing 25 and 30 wt% of niobium only Brønsted acidity has been detected. The protonated lutidine species giving the bands at 1642 and 1627 $cm^{-1}$ are strongly held and resist the evacuation at 723K.

*III.1.1.6. Lewis acidity*

Since the lutidine may not probe the existence of Lewis acid sites if their concentration is low, adsorption of CO has been used to test the presence of coordinatively unsaturated (cus) $Zr^{4+}$ sites on the surface of the 25NbZ-P sample. This probe molecule cannot detect Lewis acidity arising from (cus) $Nb^{5+}$ ions [108]. Fig. 11 shows the spectra of adsorbed CO (17 mbar) on the 25NbZ-P (a) and $ZrO_2$ (b) samples. The bands at 2195 and 2183 $cm^{-1}$ are due to two types of $Zr^{4+}$–CO carbonyls. The incorporation of niobium into the zirconia lattice causes strong decrease in the (cus) $Zr^{4+}$ sites.

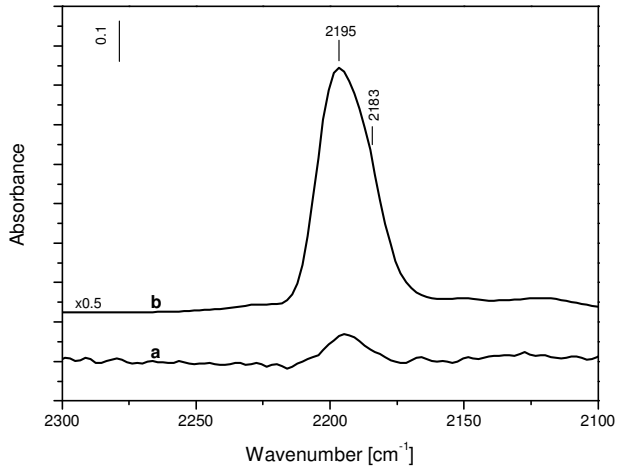


Fig. 11. FT-IR spectra of CO (17 mbar) adsorbed on the 25NbZ-P (a) and $ZrO_2$ (b) samples at room temperature.

III.1.2. $WO_3/Nb_2O_5$

The mixed oxides were prepared using acidic solutions of the peroxoniobium(V) complex, $[Nb_2(O_2)_3]^{4+}$ and AMT as precursors.

*III.1.2.1. XRD Characterization*

The 20WN773 sample has the pseudo-hexagonal (TT) crystalline phase of $Nb_2O_5$ (ICDD Card No 27-1312) and small amount of amorphous part (Fig. 12, T =773 K). The pseudo-hexagonal (TT) crystalline phase is stable solely in the presence of stabilizers (e.g. $OH^-$, $F^-$, $Cl^-$) [109,110]. In this system the hydroxide ($OH^-$) ions and the vacancies are the possible stabilizing impurities. The heat treatment at 873 K results in (Fig. 12):

- decrease in the background, which implies that the 20WN873 is completely crystalline, and
- narrowing of the peak at 28.70°, which indicates the grain growth of TT-$Nb_2O_5$.

After further heating at 973 K (Fig. 12) the single peaks (circled) at 50.82° and 71.17° (2θ) split into two peaks, which indicates the beginning of pseudo-hexagonal (TT-$Nb_2O_5$) phase to orthorhombic (T-$Nb_2O_5$) phase transformation. Weissman et al. [110] showed by HRTEM that the crystalline phases of TT-$Nb_2O_5$ and T-$Nb_2O_5$ have nearly identical structures and T-$Nb_2O_5$ can be thought as an ordered TT-$Nb_2O_5$ structure. Because no other phase is observed, except the polymorphs of $Nb_2O_5$, it can be concluded that the 20WNy sample can accept 20 wt % $WO_3$ (22 mole %) into either the TT-$Nb_2O_5$ or the T-$Nb_2O_5$ lattices as a solid solution denoted as $Nb_2O_{5(SS)}$.

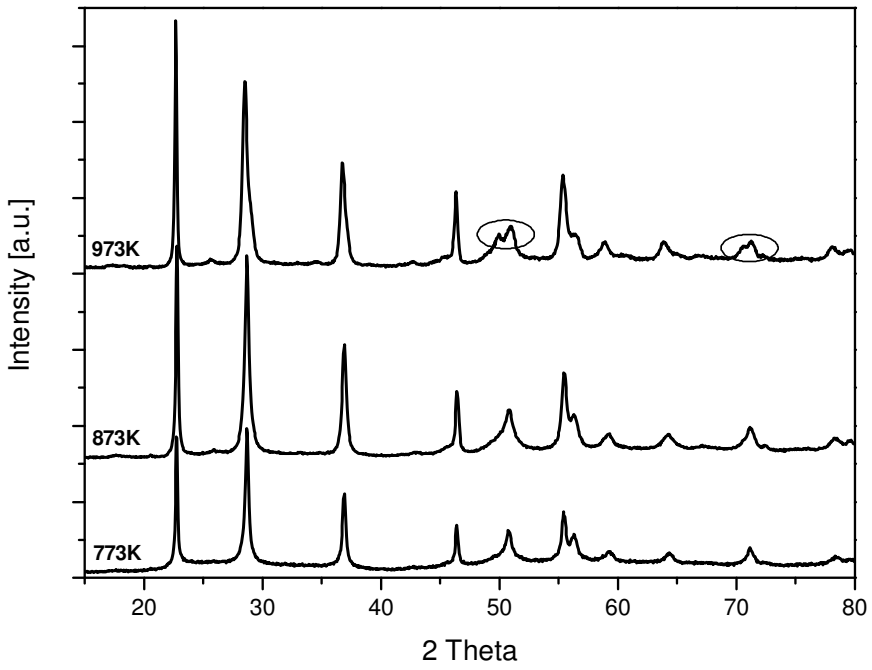


Fig. 12. Diffractograms of the 20WNy samples exposed to the heat treatment at 773, 873, and 973 K.

The 40WN773 sample contains TT-$Nb_2O_5$ phase and the amorphous part, which is seen as a high background in Fig. 13, T = 773 K. Heating at 873 K causes an increase in the amount of the crystalline TT- $Nb_2O_5$ at the expense of some amorphous part. Further heat treatment at 973 K results in the formation of the new compound, $4Nb_2O_5.7WO_3$ [ICDD card No. 18-1421]. Moreover, it might cause the TT-$Nb_2O_5$ to transform into T-$Nb_2O_5$, which is revealed by the splitting of the high angle peaks at around 50° and 71°. However, the peaks belonging to the new compound, $4Nb_2O_5.7WO_3$, overlap with the T-$Nb_2O_5$ peaks, which makes it difficult to reach a conclusion. Taking into account the $Nb_2O_5$ : $WO_3$ mole ratio in the $4Nb_2O_5.7WO_3$, we estimated roughly that the 40WN973 sample contains 50 wt % of the $Nb_2O_5$- based solid solution and 50 wt % of the mixed oxide.

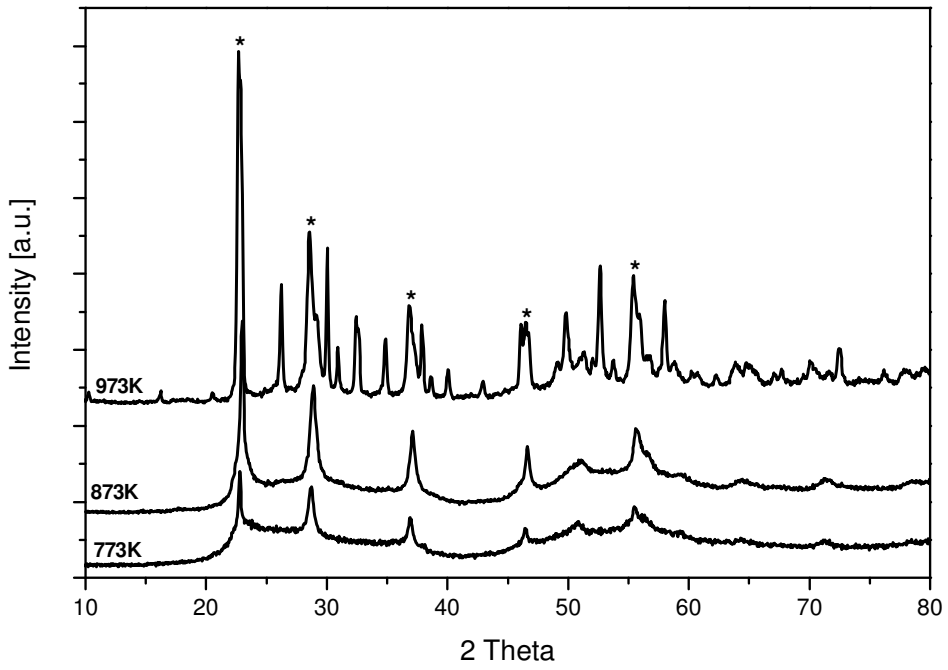


Fig. 13. Diffractograms of 40WNy samples exposed to the heat treatment at 773, 873, and 973 K. (* indicates either the TT- $Nb_2O_5$ phase or T- $Nb_2O_5$ phase).

The 60WN973 sample crystallizes into the orthorhombic phase of the stoichiometric mixed oxide, $4Nb_2O_5.7WO_3$ [ICDD card No. 18-1421] at 973K (Fig. 14) with unit cell parameters of a = 12.220Å, b = 36.660 Å, c = 3.940 Å and $\alpha = \beta = \gamma = 90°$.

After the calcinations at 773, 873 and 973 K, the 80WN sample is mainly amorphous and contains negligible amount of crystallinity. Heating of the sample at 1073 K results in the formation of the orthorhombic $4Nb_2O_5.7WO_3$ phase and monoclinic $WO_3$ phase, which contains $Nb_2O_5$ as a solute. However, it has relatively high background (Fig. 15, T = 1073 K). It means that further heat treatment is required in order to get fully crystalline sample. The amounts of each component in the phases determined for the 80WN1073 sample cannot be calculated because the maximum weight percentage of niobia dissolved in m-$WO_3$ is not known.

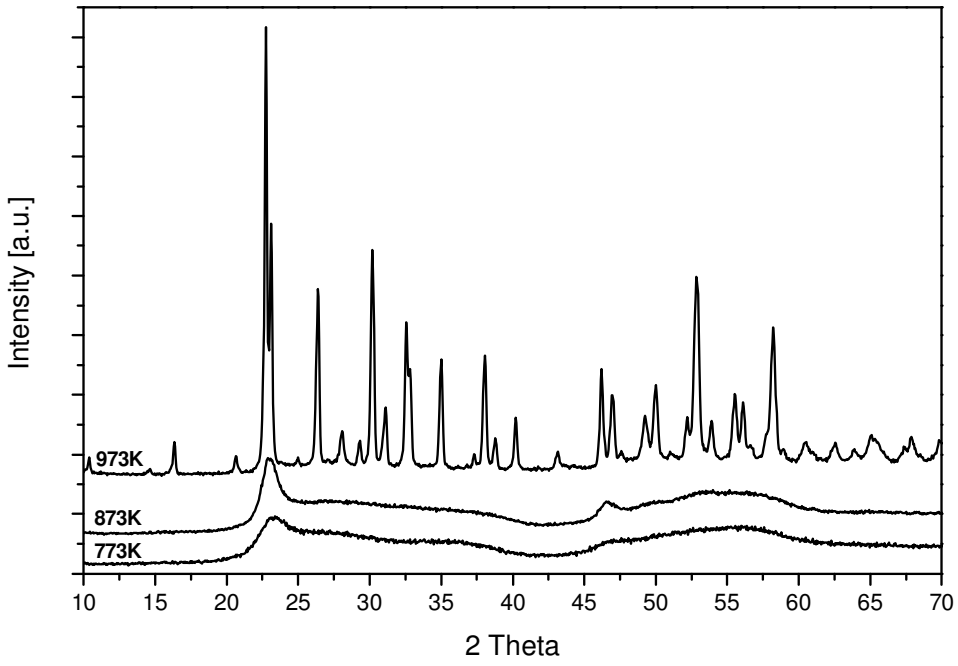


Fig. 14. Diffractograms of 60WNy samples exposed to the heat treatment at 773, 873, and 973 K.

Table 7 summarizes the phase composition of the xNWy samples.

Fiegel et al. [111] studied the phase equilibria in the $WO_3$-$Nb_2O_5$ system between 973 and 1473 K. They found that the monoclinic (H-) $Nb_2O_5$ can make solid solution with maximum of 30 wt % of tetragonal tungsta. However, the solubility of H-$Nb_2O_5$ in tetragonal $WO_3$ is lower than 2.3 wt %. Furthermore, Roth et al. [112] showed that in the high-temperature (1248 K and above) equilibrium diagram of the system $Nb_2O_5$-$WO_3$ the presence of the solid solution could not be stated definitely for $Nb_2O_5$, though 3.4 wt % of H-$Nb_2O_5$ can incorporate into the lattice of the tetragonal $WO_3$ to form the $WO_3$-based solid solution. However, our method of synthesis (using Nb(V) peroxo precursor) allows studying the metastable phases (e.g. TT-$Nb_2O_5$, m-$WO_3$) and the solid solutions of each component with different contents. This method allows us to observe a TT-$Nb_2O_5$-based solid solution with at least 20 wt % of m-$WO_3$ at room temperature. Moreover, it gives

possibility to synthesize the mixed oxides at lower calcination temperatures (max. 1073 K) and to stabilize them at ambient temperature.

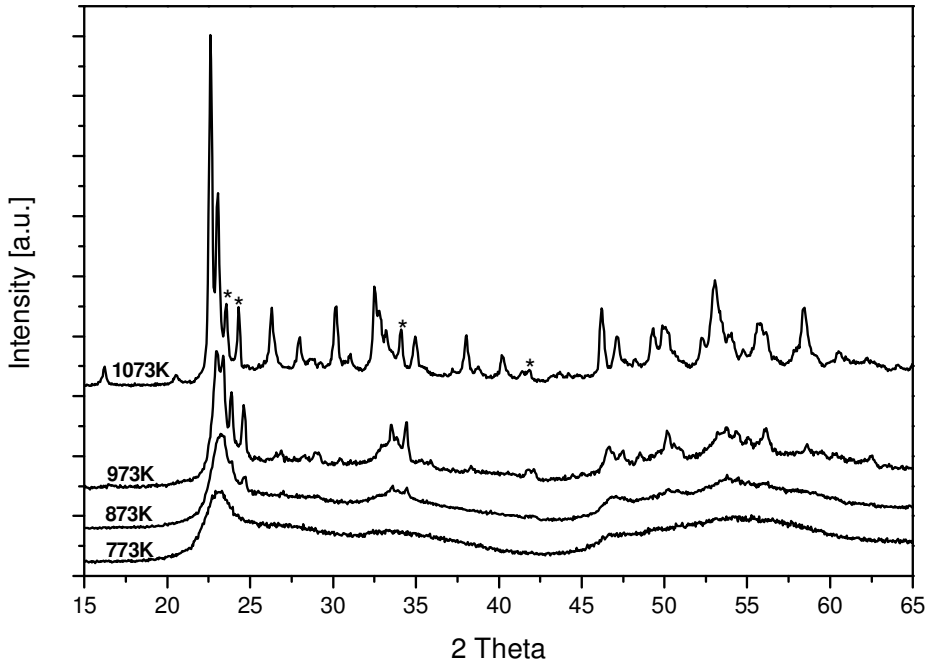


Fig. 15. Diffractograms of the 80WNy samples exposed to the heat treatment at 773, 873, 973 and 1073 K. (* indicates the monoclinic phase of $WO_3$).

**Table 7.** Phase composition of the xNWy samples.

| | **773K** | **873K** | **973K** | **1073K** |
|---|---|---|---|---|
| **20WN** | Amorphous + TT-$Nb_2O_5$ | TT-$Nb_2O_5$ | TT-$Nb_2O_5$ + T-$Nb_2O_5$ | - |
| **40WN** | Amorphous + TT-$Nb_2O_5$ | Amorphous + TT-$Nb_2O_5$ | TT-$Nb_2O_5$/T-$Nb_2O_5$ + $4Nb_2O_5.7WO_3$ | - |
| **60WN** | Amorphous | Amorphous | $4Nb_2O_5.7WO_3$ | - |
| **80WN** | Amorphous | Amorphous | Amorphous + $4Nb_2O_5.7WO_3$ | $4Nb_2O_5.7WO_3$ + m-$WO_3$ |

*III.1.2.2. Micro-Raman spectroscopy*

The Raman spectra of the xWNy samples heat-treated at different temperatures are shown in Fig. 16. The pseudo-hexagonal phase of niobia has three characteristic bands at 700, 314 and 250 $cm^{-1}$, which are due to the symmetric stretching, asymmetric and symmetric bending modes of niobia polyhedra [113]. The unresolved, weak band at ~900 $cm^{-1}$ is due to the terminal Nb=O stretching vibration [113]. The Raman spectrum of the 20WN773 sample shows features similar to that of $Nb_2O_5$. Heating at 873 K results in decrease in the intensity of the band at 900 $cm^{-1}$, which suggests lowering in the Nb=O surface concentration caused by reduction of the surface area of powder particles. Because the TT-$Nb_2O_5$ and T-$Nb_2O_5$ have similar structures, the Raman spectra of the 20WNy sample taken after the calcination at 873 and 973 K (Fig. 16, Panel A, spectra b and c) possess the same characteristic features. Thus, it is inferred that $WO_3$ at loading of 20 wt % incorporates well into the niobia matrix, which is consistent with the XRD result.

It is deduced from the XRD data that the 40WN873 sample is composed of amorphous and TT-$Nb_2O_5$ phases. Therefore, its Raman spectrum resembles that of the 20WN773 sample (compare the spectra a and b in panels A and B of Fig. 16). After the calcination at 973 K, new bands at 994, 820, 728 and 320 $cm^{-1}$ are observed due to the formation of the orthorhombic $4Nb_2O_5.7WO_3$ phase.

The Raman spectra of the 60WN773 and 60WN873 samples show the characteristic signals of the amorphous phase because the 60WNy sample forms the mixed oxide, $4Nb_2O_5.7WO_3$, at 973 K (Fig. 16, Panel C). To the best of our knowledge, Raman studies on the $4Nb_2O_5.7WO_3$ compound are not available in the literature. Our investigation shows for the first time that the Raman bands at 994, 820, 728 and 320 $cm^{-1}$ can be attributed to the mixed oxide, $4Nb_2O_5.7WO_3$.

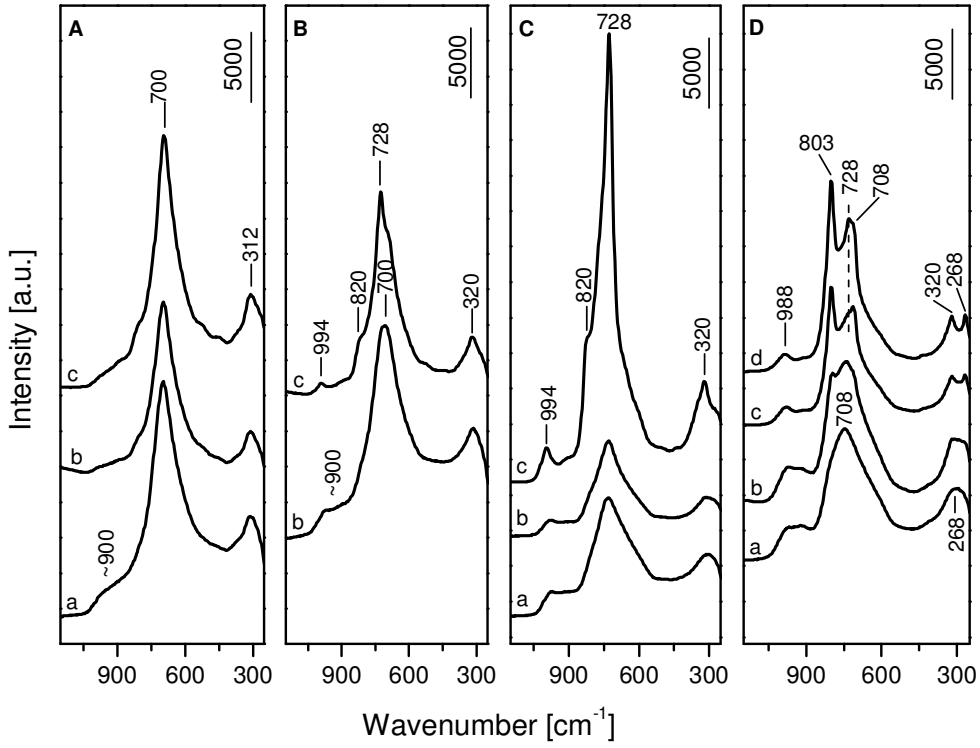


Fig. 16. Raman spectra of the 20WNy (Panel A), 40WNy (Panel B), 60WNy (Panel C) and 80WNy samples (Panel D) calcined at 773 K (a), 873 K (b), 973 K (c) and 1073 K (d). The peak intensities are normalized with respect to the internal standard BN.

The Raman spectrum of the 80WN973 sample has bands at 988, 803, 728, 708, 320 and 268 $cm^{-1}$ (Fig. 16, Panel D, spectrum c), which show the presence of m-$WO_3$ and $4Nb_2O_5.7WO_3$ phases. The broadening of all these bands is associated with the beginning of the crystallization process. These bands sharpen after the calcination at 1073 K, which indicates the continuation of crystallization. These results agree with the XRD data.

*III.1.2.3. DR-UV-vis spectroscopy*

The DR-UV-vis spectra of the xWNy samples and bulk $WO_3$ and $Nb_2O_5$ are shown in Fig. 17. The absorptions at 336 ($Nb_2O_5$) and 384 nm ($WO_3$) originate from a $O^{2-} \rightarrow M^{n+}$ charge transfer process from the valence band (manly 2p orbitals of the oxide

ions) to the conduction band, formed by the valence orbitals of the cations [114-117]. The spectra recorded for the xWN973 (x = 20 - 60) samples closely match with that of pure niobia.

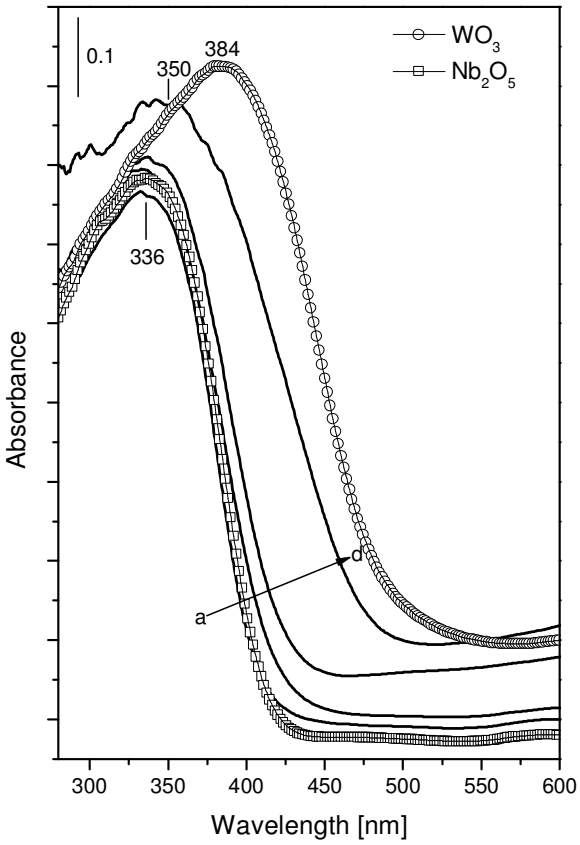


Fig. 17. Diffuse reflectance UV-vis spectra of $Nb_2O_5$, $WO_3$ and xWNy samples: (a) 20WN973, (b) 40WN973, (c) 60WN973, (d) 80WN1073.

In Fig. 18, the absorption edge energies are shown as a function of the $WO_3$ loading at different calcination temperatures. The samples, which have $WO_3$ content up to 40 wt % and heat-treatments between 773 and 973 K, have absorption edge energies close to that of $Nb_2O_5$. The 60WN973 sample owning the single phase of the stoichiometric mixed oxide, $4Nb_2O_5.7WO_3$, has 3.09 eV of the absorption edge energy. Since the extent of crystallinity depends on the calcination temperature, the HOMO-LUMO gap of the

80WNy samples decreases with the increasing of the heat treatment temperature. Besides, the presence of the m-$WO_3$, whose absorption edge energy is 2.59 eV, results in further reduction.

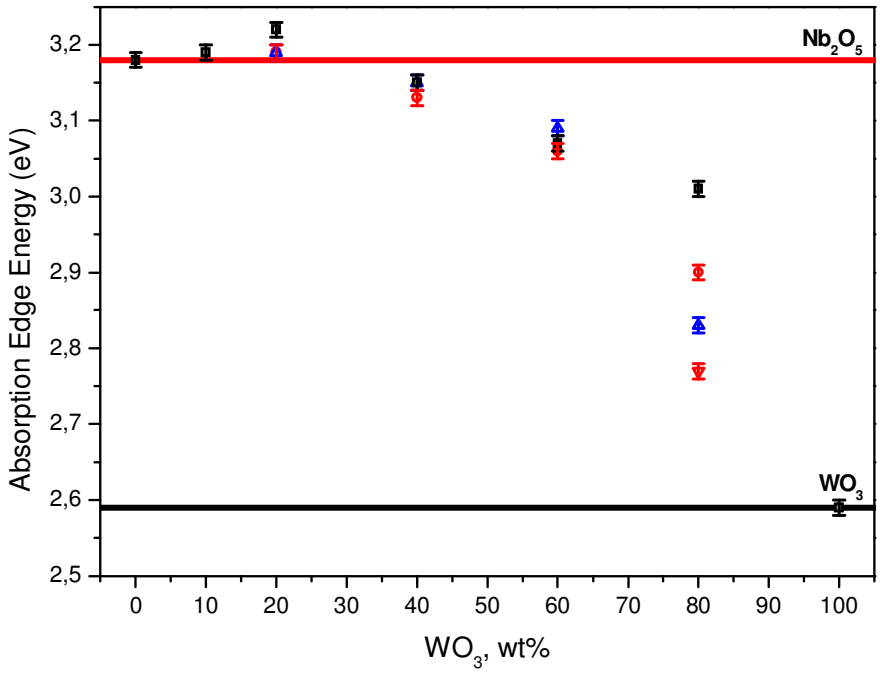


Fig. 18. Band gap energy as a function of $WO_3$ loading at different calcination temperatures: □: 773, **O**: 873, **Δ**:973, **∇**:1073 (Error: ±0.01).

*III.1.2.4. Brønsted acidity*

The FT-IR spectra of the heat-treated samples, which were obtained after the adsorption of 2.4 Torr of lutidine and followed by evacuation for 15 min at 423 K, are shown in Fig. 19. The bands at 1641 and 1628 $cm^{-1}$ are due to the 8a and 8b vibrations of the protonated lutidine [102,106,107]. The amount of Brønsted acid sites is the highest on the 0WN773 sample whereas the 100WN773 sample does not have any acidity. The highest Brønsted acidity of the 0WN773 sample stems from the presence of the TT-$Nb_2O_5$ phase, in which the main stabilizing impurity is the $OH^-$ ions. Furthermore, the protonated lutidine is stable on the surface of the 0WN773 sample up to 673 K. Even though the

crystallite sizes decrease with the increase in the tungsta content in the solid solution region of niobia, the Brønsted acidity decreases due to the incomplete crystallization (Fig. 19).

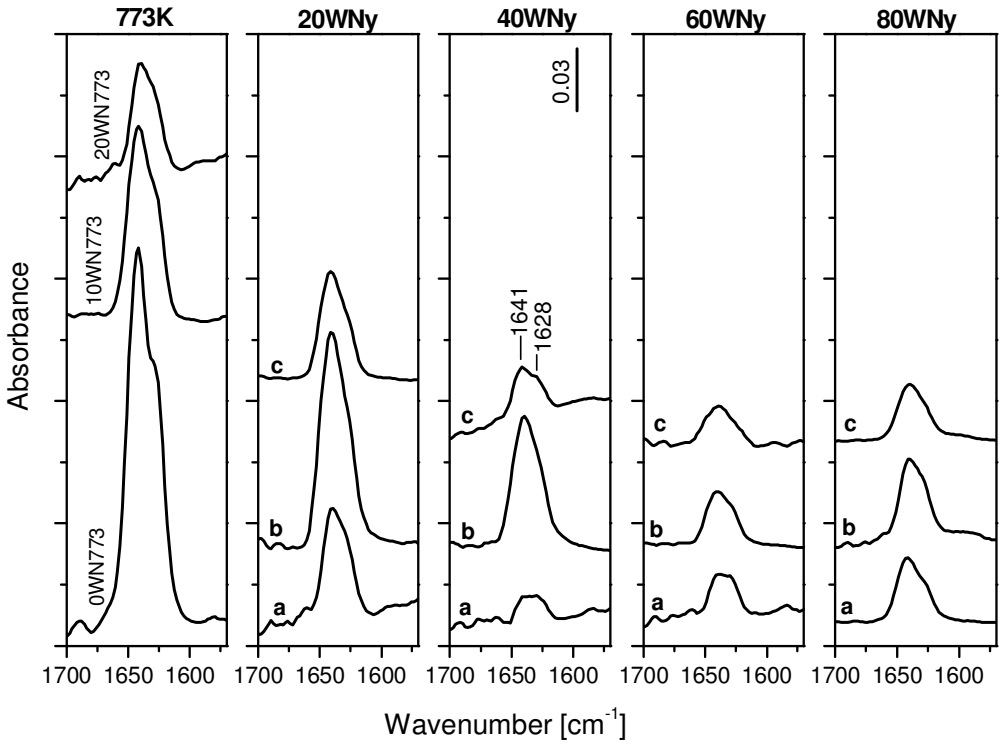


Fig. 19. FT-IR spectra of 2,6-lutidine (2.4Torr) adsorbed at RT for 10 min followed by evacuation at 423 K for 15 min: (a) xWN773 samples, (b) xWN873 samples and (c) xWN973 samples. The spectra are normalized with respect to the pellet weight.

Successive heat treatments at 873 and 973 K result in, first, an increase and then a decrease in the amount of Brønsted acid sites for the 20WNy samples (Fig. 19, 20WNy). The possible reasons are the following:

- the 20WN873 sample is free of amorphous phase and has only TT-$Nb_2O_5$ structure with larger grains (see section *III.1.2.1. XRD Characterization*), which is expected to cause reduction of surface area and increase in the density of surface OH groups,

- the TT-$Nb_2O_5$ phase transforms into the T-$Nb_2O_5$ phase accompanied by either further grain growth or sintering of the 20WN973 sample, both of which result in smaller surface area. During disordered to ordered transformation, the stabilizer, the OH ions, is lost, which is the main difference between the two structures [110]. This explains the predominant reason for the drastic reduction in the Brønsted acidity.

Moreover, phase transformation affects the stability of the protonated lutidine. TT-$Nb_2O_5$ phase makes the lutidinium cation stable up to 773 K, whereas protonated lutidine is observed for the T-$Nb_2O_5$ phase up to 673 K.

For the 40WNy samples (Fig. 19, 40WNy) the maximum amount of TT-$Nb_2O_5$ is obtained by the calcination at 873 K. Thus, it culminates in the maximum amount of Brønsted acid sites and the highest strength of the protonated lutidine, which is stable up to 773 K. Heat treatment at 973 K causes a severe decrease in the Brønsted acidity due to the formations of the compound, $4Nb_2O_5.7WO_3$, and most probably the T-$Nb_2O_5$ phase. Both phases cause a lowering of the stability of the lutidinium cation. The Brønsted acidity practically stays constant and has, somewhat, low strength for both, 60WNy and 80WNy samples, at all calcination temperatures.

## III.2. Catalytic Properties

### III.2.1. Catalytic Activity

The catalytic tests in the $C_3H_6$-SCR of $NO_x$ have been performed with Pd-free and Pd-promoted catalysts (0.1 wt % of Pd). The unpromoted oxide systems are characterized by the highest concentration of Brønsted acid sites, namely the 25NbZ-P and 20WN-873 samples. It has been shown [74] that the 25NbZ-P sample has a sufficient amount of Brønsted acid sites necessary for the stabilization of dispersed Pd(II) species.

Pd-free and Pd-promoted 20WN873 samples are inactive in the SCR of $NO_x$ with propene.

Fig. 20A shows the activity of 25NbZ-P and 0.1Pd/25NbZ-P catalysts in the reduction of $NO_x$ with propene at various temperatures. The $NO_x$ conversion over the Pd-free sample (Fig. 20A, curve a) passes through a maximum at 493 K reaching 62%. The promotion with palladium lowers the $NO_x$ conversion and makes the maximum of the curve more flat (Fig. 20A, curve b). Maximum $NO_x$ conversion of 37 – 40% is achieved at 473 – 523 K.

Fig. 20B displays the conversions of propene into $CO_2$ over both catalysts. It seems that the addition of palladium is favorable for activating the reductant molecule at temperatures below 473 – 493 K. Both catalysts display stable activity at the temperature of maximum $NO_x$ conversion (the duration of catalytic activity tests was limited to 10 h).

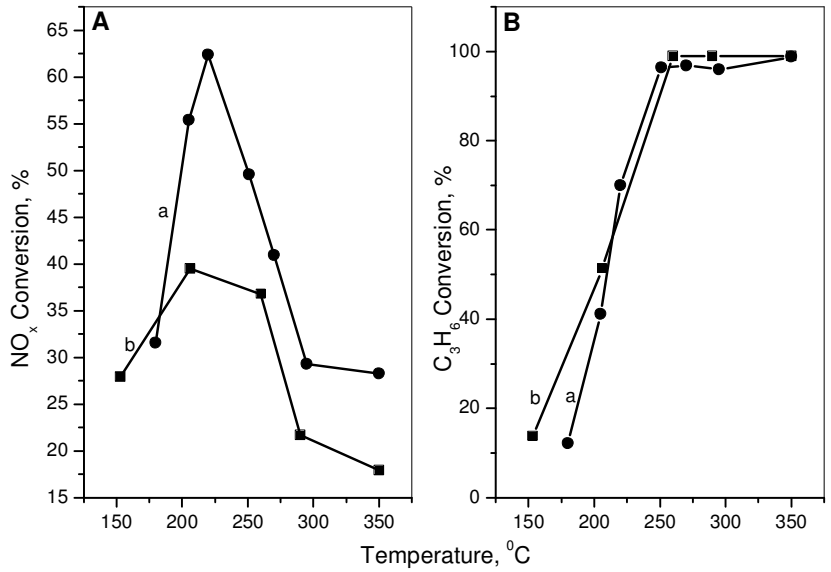


Fig. 20. Panel A: Catalytic activity for $NO_x$ reduction with propene over 25NbZ-P (a) and 0.1Pd/25NbZ-P catalysts (b) at various temperatures. Panel B: Conversion of propene into $CO_2$ over 25NbZ-P (a) and 0.1Pd/25NbZ-P catalysts (b). Reaction conditions: 245 ppm $NO_x$ ($NO/NO_2$ = 1.77), 504 ppm $C_3H_6$, 9 vol.% $O_2$, GHSV = 10 000 $h^{-1}$).

The 25NbZ-P catalyst shows good resistance to $SO_2$ poisoning (Fig. 21, Panel A). There is no loss in the $C_3H_6$-SCR activity for 2 h after the addition of 56 ppm of $SO_2$ to the reaction mixture. The concentration of $SO_2$ is increased to 200 ppm, so-called *fast poisoning experiment*. If the catalyst does not have any resistance to $SO_2$ poisoning under the conditions of fast poisoning experiment, it deactivates completely. The activity of the 25NbZ-P catalyst decreases to approximately 54 % of $NO_x$ conversion and the activity remains unchanged for more than 5 h under these conditions.

The presence of $H_2O$ vapour (1.2 vol. %) in the reaction mixture results in 50 % of $NO_x$ conversion and it does not change for 3h (Fig. 21, Panel B).

These results show that the catalytic properties of the 25NbZ-P sample could be of interest regarding the development of efficient noble-metal free HC-SCR catalyst that could be active at typical diesel exhaust-gas temperatures (≤ 573 K).

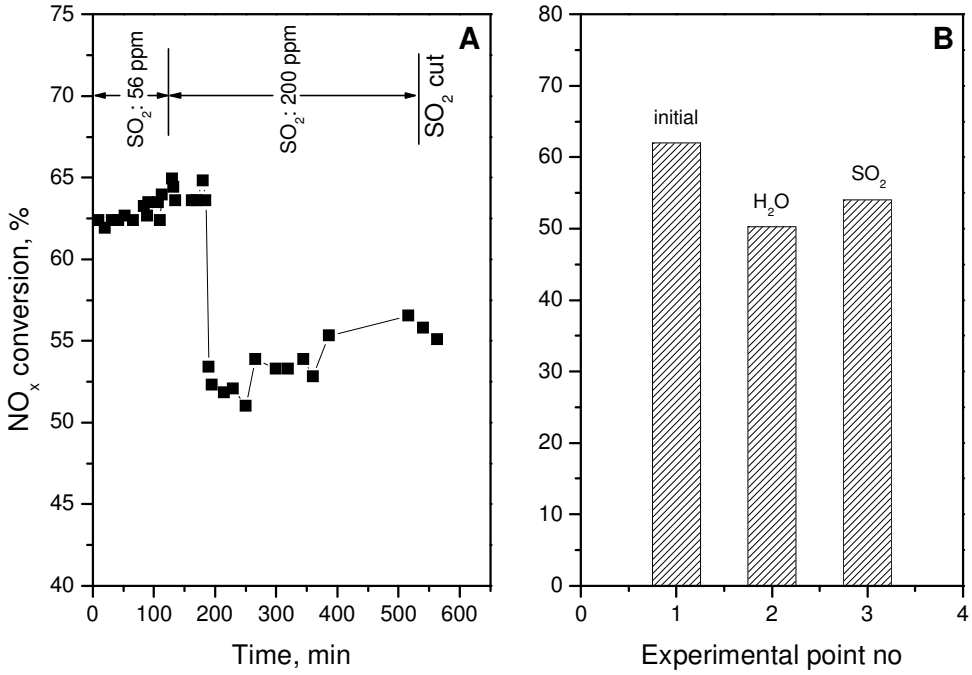


Fig. 21. Results of the $SO_2$ poisoning experiment (Panel A), and effect of $H_2O$ and $SO_2$ on the conversion of $NO_x$ over the 25NbZ-P catalyst (Panel B).

III.2.2. Mechanistic Studies

According to our knowledge, there are no reports dealing with the $DeNO_x$ properties as well as with NO interaction with propene in the presence of oxygen on $Zr_6Nb_2O_{17}$ solid solution (25NbZ-P sample). As shown above, this material can be of interest for developing low-temperature catalysts for the selective reduction of $NO_x$ with hydrocarbons. Therefore, in order to determine the reaction route, we carried out in situ FTIR investigations of the adsorption and co-adsorption of the reagents followed by their interactions at various temperatures over the Pd-free and Pd-promoted 25NbZ-P samples.

*III.2.2.1. Co-adsorption of ($NO+O_2$)*

III.2.2.1.1. The $ZrO_2$ sample

The FT-IR spectrum of $NO_x$ species adsorbed on $ZrO_2$ and the corresponding gas phase spectrum obtained after the exposure of the sample at room temperature for 20 min to a (10 mbar NO+20 mbar $O_2$) gas mixture are presented in Fig. 22A and 22A`. The comparison of the gas phase spectra in the absence (Fig. 22A′, spectrum a) and presence of zirconia (Fig. 22A′, spectrum b) shows that the $ZrO_2$ sample does not promote the formation of $NO_2$ (1617 $cm^{-1}$ [118]) and $N_2O_4$ (1758, 1264 $cm^{-1}$ [118]) at ambient temperature. The gas phase contains some amount of $N_2O$ (2240 $cm^{-1}$ [118]) molecules. Co-adsorption of NO and $O_2$ on the $ZrO_2$ sample causes the formation of surface nitrates differing in the mode of their coordination (Fig. 22A). The bands at 2240, 1934 and 1900 $cm^{-1}$ disappear upon evacuation at room temperature (Fig. 22B, spectrum a). Therefore, the former band could be assigned to adsorbed $N_2O$ and the latter bands could be attributed to two types of $Zr^{4+}$–NO nitrosyls having nitrates in the vicinity [92,119].

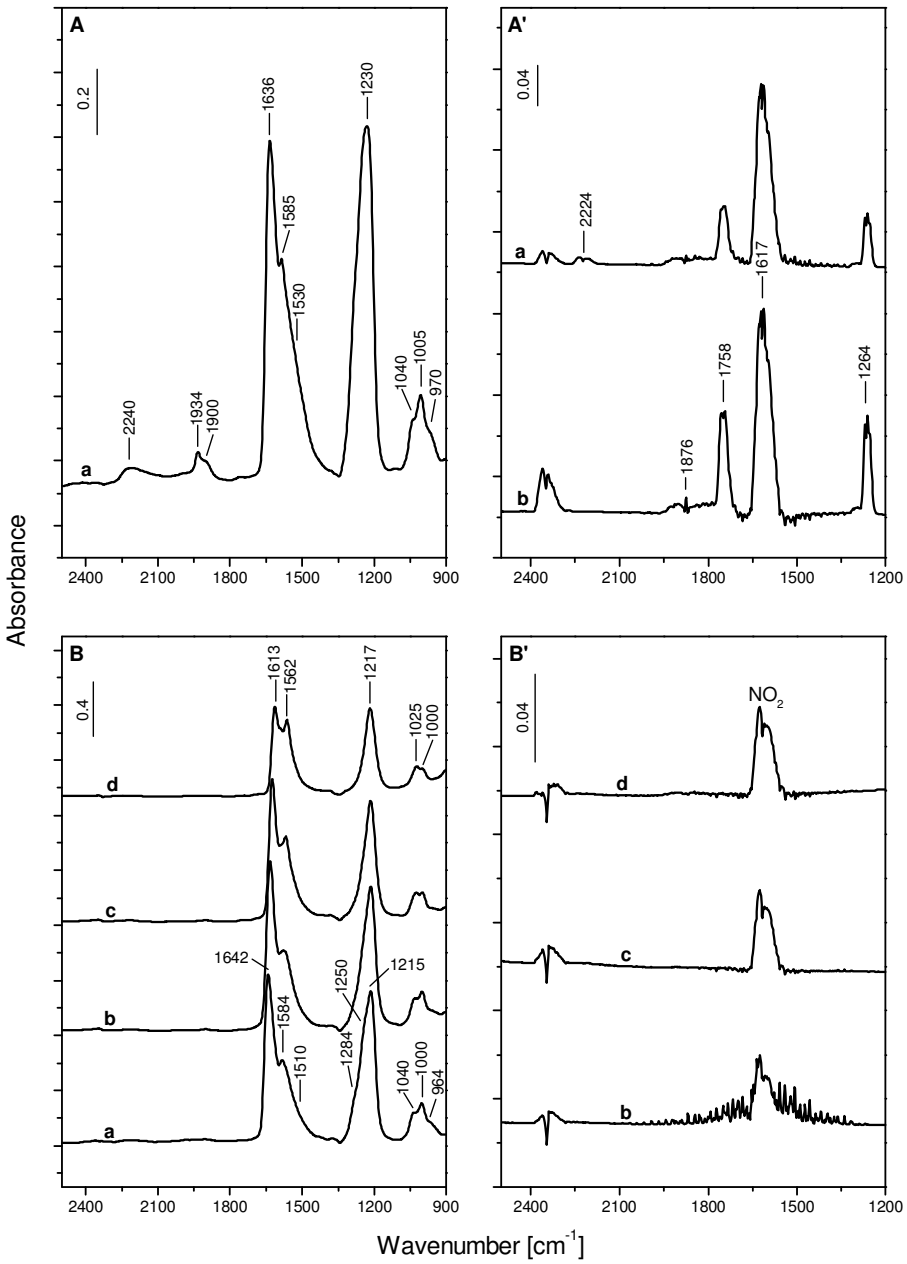


Fig. 22. FT-IR spectrum (a) of the $ZrO_2$ sample taken after the adsorption of a (10 mbar NO+20 mbar $O_2$) mixture for 20 min at rt (Panel A) and gas phase spectra in the presence (a) and absence (b) of $ZrO_2$ sample (Panel A`). FT-IR spectra after the evacuation for 10 min at rt (a), and subsequently heating the isolated IR cell for 15 min at 423 K (b), 523 K (c) and 623 K (d) (Panel B) and corresponding gas phase spectra (Panel B`).

Heating the $ZrO_2$ sample containing surface nitrate species in the closed IR cell in the 298 – 623 K temperature range results in the FT-IR spectra shown in Fig. 25B and B`. The increase in temperature causes the decomposition of the surface nitrates producing

$NO_2$ in the gas phase. The intensities of the bands of bidentate nitrate (1584 – 1562, 1250 and 1031 $cm^{-1}$) do not change considerably upon heating, which means that this species has the highest thermal stability.

**Table 8.** Assignments of the absorption bands in the spectra observed during the NO+$O_2$ coadsorption on the $ZrO_2$ sample at room temperature.

| Species | Band position, $cm^{-1}$ | Vibration |
|---|---|---|
| $N_2O$ | 2240 | ν(NN) |
| Monodentate $NO_3^-$ | 1510<br>1284<br>964 | $\nu_{as}(NO_2)$<br>$\nu_s(NO_2)$<br>ν(NO) |
| Bridged $NO_3^-$ | 1642-1613<br>1215 – 1217<br>1000 | ν(N=O)<br>$\nu_{as}(NO_2)$<br>$\nu_s(NO_2)$ |
| Bidentate $NO_3^-$ | 1585-1562<br>1250<br>1031 | ν(N=O)<br>$\nu_{as}(NO_2)$<br>$\nu_s(NO_2)$ |

III.2.2.1.2. The 25NbZ-P catalyst

Fig. 23A shows the spectrum of the gas phase detected at room temperature immediately after the admission of a gas mixture containing 10 mbar of NO and 20 mbar of $O_2$ to the empty IR cell (spectrum (a)). Gaseous $NO_2$ (band at 1617 $cm^{-1}$ [118]) and $N_2O_4$ (bands at 1758 and 1264 $cm^{-1}$ [118]) are formed by the reaction of NO with $O_2$ in the gas phase ($2NO + O_2 = 2NO_2$). The concentrations of NO and $NO_2$ do not change appreciably after 30 min.

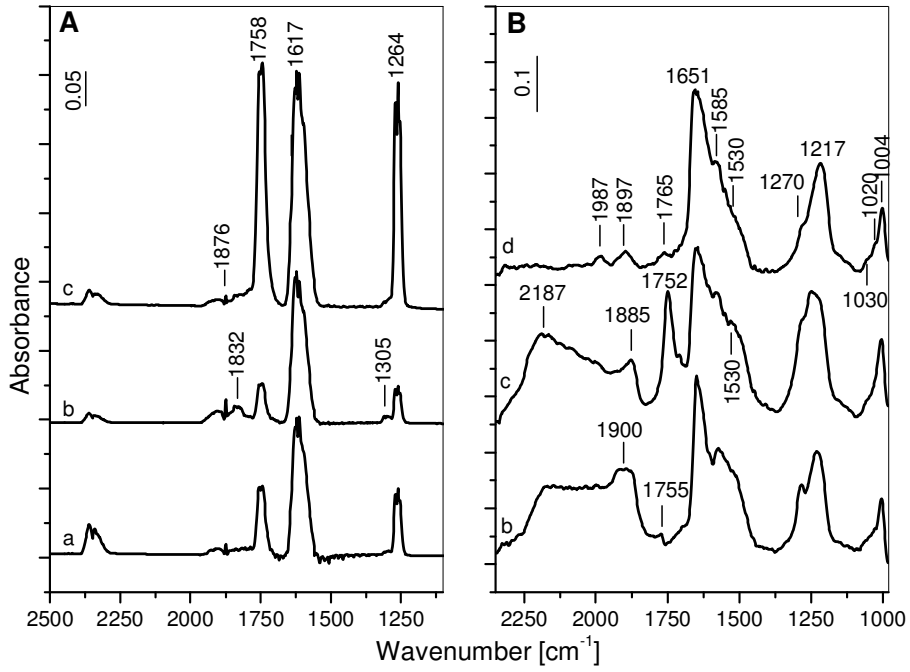


Fig. 23. Panel A: Gas phase spectra recorded at room temperature immediately after the admission of a (10 mbar NO+20 mbar $O_2$) mixture to the empty IR cell (a), after the introduction of the same gas mixture immediately to the IR cell in the presence of the 25NbZ-P catalyst (b), and after 30 min (c). Panel B: FT-IR spectra of adsorbed $NO_x$ species taken immediately during the exposure of the 25NbZ-P catalyst to the same gas mixture at room temperature (b), after 30 min (c) and upon dynamic evacuation for 30 min (d).

The spectrum taken immediately after the exposure of the 25NbZ-P sample at room temperature to the same gas mixture (Fig. 23A, spectrum (b)), in addition to the absorptions of $NO_2$ and $N_2O_4$, contains a pair of bands at 1832 and 1305 $cm^{-1}$ corresponding to the $\nu$(N=O) and $\nu_s(NO_2)$ modes of asymmetric $N_2O_3$ [118]. Since the latter compound was not observed when mixing NO and $O_2$ in the empty IR cell (Fig. 23A, spectrum (a)), it is evident that the 25NbZ-P catalyst favors the comproportionation of NO and $NO_2$ to $N_2O_3$. The contact of the sample for 30 min with the gas mixture leads to strong increase in the amounts of $NO_2$ and $N_2O_4$ and significant lowering of the concentrations of NO and $N_2O_3$ (Fig. 23A, spectrum (c)). This result indicates that the

25NbZ-P sample promotes the oxidation of NO at room temperature. The spectra of the sample obtained immediately (Fig. 23B, spectrum (b)) and 30 min after the admission of the NO+$O_2$ mixture (Fig. 23B, spectrum (c)) contain bands at 1900 – 1885 and 1755 – 1752 $cm^{-1}$ which are attributed to adsorbed $N_2O_3$ and $N_2O_4$, respectively [119]. The broad absorption with maximum at 2187 $cm^{-1}$ is typical of $NO^+$ species [92,119]. The bands at 1651, 1217 and 1004 $cm^{-1}$ are assigned to the $\nu$(N=O), $\nu_{as}(NO_2)$ and $\nu_s(NO_2)$ stretching vibrations of bridged nitrates, whereas the bands at 1585, 1270 and 1020 $cm^{-1}$ indicate the formation of bidentate $NO_3^-$ species [92,119]. The shoulder at about 1530 $cm^{-1}$ (Fig. 23B, spectrum (c)) decreases in intensity during the out-gassing (Fig. 23B, spectrum (d)). This absorption is due, most likely, to the $\nu_{as}(NO_2)$ mode of adsorbed $N_2O_3$ [92,119], which is superimposed to the $\nu$(N=O) stretching vibration of a second bidentate nitrate. The $\nu_s(NO_2)$ modes of the latter species is positioned at 1030 $cm^{-1}$, whereas the $\nu_{as}(NO_2)$ band should fall between 1350 and 1200 $cm^{-1}$ and cannot be resolved. Since the $Zr^{4+}$ ions are considered to be irreducible, the $Nb^{5+}$ species should play the role of oxidizing centers in the processes of $NO_2/N_2O_4$ and surface nitrate generation. Another possibility for the formation of surface $NO_3^-$ species is through self-ionization of $NO_2$ on surface Lewis acid-base pairs according to the reaction [92,119]:

$$2NO_2 \rightarrow NO_3^- + NO^+$$

In general, the $NO_2$, $N_2O_4$ and $N_2O_3$ molecules are weakly adsorbed and they can be removed easily by evacuation [92,119]. Therefore, the weak bands at 1987, 1897 and 1764 $cm^{-1}$ observed in the spectrum upon prolonged evacuation (Fig. 23B, spectrum (d)) are attributed to combination modes of the nitrate species [92,119]. The $NO^+$ species disappear upon the evacuation. The assignment of the absorption bands observed during the NO+$O_2$ coadsorption on the 25NbZ-P sample at room temperature is proposed in Table 9.

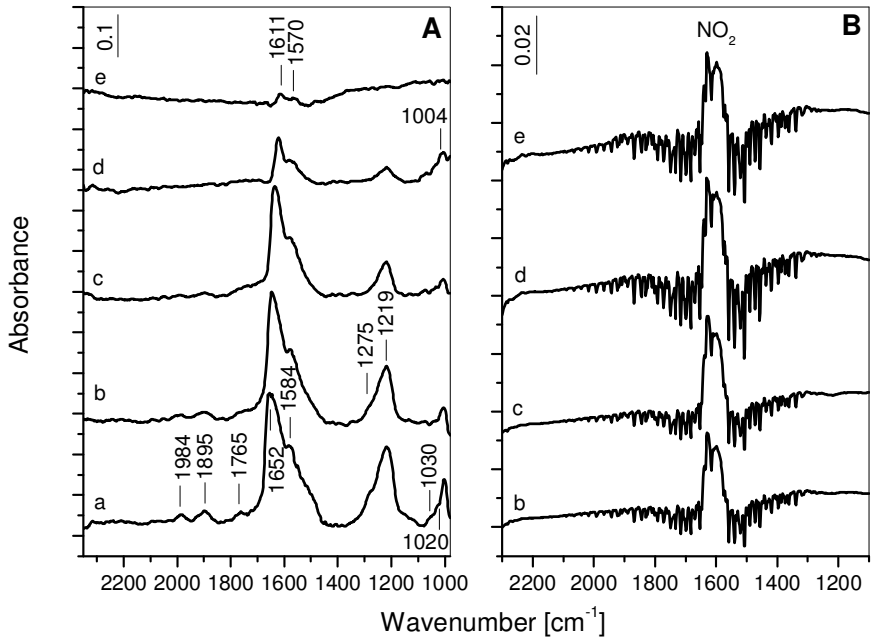


Fig. 24. Panel A: FT-IR spectra of the 25NbZ-P catalyst taken after the adsorption of a (10 mbar NO+20 mbar $O_2$) mixture to the IR cell for 30 min at room temperature followed by evacuation for 30 min (a), and after heating the isolated IR cell for 15 min at 373K (b), 423 K (c), 523 K (d) and 623 K (e). Panel B: Gas phase spectra collected at 373K (b), 423 K (c), 523 K (d) and 623 K (e).

The thermal stability of the nitrate species adsorbed on the 25NbZ-P sample was investigated by heating the isolated IR cell in the 298 – 623 K temperature range for 15 min at each temperature (Fig. 24). A gradual decrease in the intensities of the nitrate bands is observed with the increase in the temperature (Fig. 24A). At 623 K the $NO_3^-$ species almost vanish. The gas phase spectra (Fig. 24B) show that the product of thermal decomposition of the nitrates is $NO_2$. It should be noted that the thermal stability of surface nitrates formed on pure zirconia is significantly higher than that of the nitrate species adsorbed on the 25NbZ-P sample. In the former case the $NO_3^-$ species are observed upon heating at 623 K. The obtained results indicate that the introduction of niobium(V) to zirconia favors the oxidation of NO to $NO_2$ and lowers the thermal stability of the surface nitrates.

**Table 9**. Assignments of the absorption bands in the spectra observed during the NO+$O_2$ coadsorption on the 25NbZ-P catalyst at room temperature.

| Species | Band position, $cm^{-1}$ | Vibration |
|---|---|---|
| $NO^+$ | 2187 | $\nu$(NO) |
| $N_2O_3$(ads) | 1885<br>1530 | $\nu$(N=O)<br>$\nu_{as}(NO_2)$ |
| $N_2O_4$(ads) | 1752 | $\nu_{as}(NO_2)$ |
| Bridged $NO_3^-$ | 1651<br>1217<br>1004<br>1987, 1897 | $\nu$(N=O)<br>$\nu_{as}(NO_2)$<br>$\nu_s(NO_2)$<br>$\nu_s(NO_2)+\delta$(ONO) |
| Bidentate $NO_3^-$<br>(two types) | 1585, 1530<br>1270<br>1020, 1030<br>1765 | $\nu$(N=O)<br>$\nu_{as}(NO_2)$<br>$\nu_s(NO_2)$<br>$\nu_s(NO_2)+\delta$(ONO) |

III.2.2.1.3. Summary of the Results on Coadsorption of NO+$O_2$ on the samples studied

Co-adsorption of NO + $O_2$ on 25NbZ-P sample at room temperature leads to the formation of various surface nitrates and gaseous species such as $NO_2$, $N_2O_4$ or $N_2O_3$. Since the $Zr^{4+}$ ions are considered to be irreducible, the $Nb^{5+}$ species should play the role of oxidizing centers in the processes of $NO_2/N_2O_4$ and surface nitrate generation. Since both, nitrates and nitrosonium ions are observed on the 25NbZ-P sample, another way for the formation of nitrates can be the self ionization of $NO_2$.

The results of the thermal stability of nitrate species show that; (i) the product of thermal decomposition of the nitrates is $NO_2$ and (ii) the incorporation of niobium(V) ions into zirconia matrix lowers the thermal stability of the surface nitrates.

*III.2.2.2. Co-adsorption of ($C_3H_6$+$O_2$) on the 25NbZ-P catalyst*

Fig. 25 shows the development of the spectra in the 298 – 623 K temperature range obtained during the contact of the catalyst with a gas mixture containing 3 mbar of $C_3H_6$ and 10 mbar of $O_2$. The bands at 1619 and 1451 $cm^{-1}$ observed in the spectrum detected at room temperature (Fig. 25, spectrum (a)) are characteristic of propene adsorbed on oxide surfaces and correspond to the ν(C=C) and $\delta_{as}(CH_3)$ modes, respectively [120]. The weak absorption at 2980 – 2950 $cm^{-1}$ is assigned to the $CH_3$ stretching vibrations. Heating the closed IR cell at 373 K for 15 min (Fig. 25, spectrum (b)), causes a decrease in the intensity of the bands at 1619 and 1451 $cm^{-1}$ of adsorbed

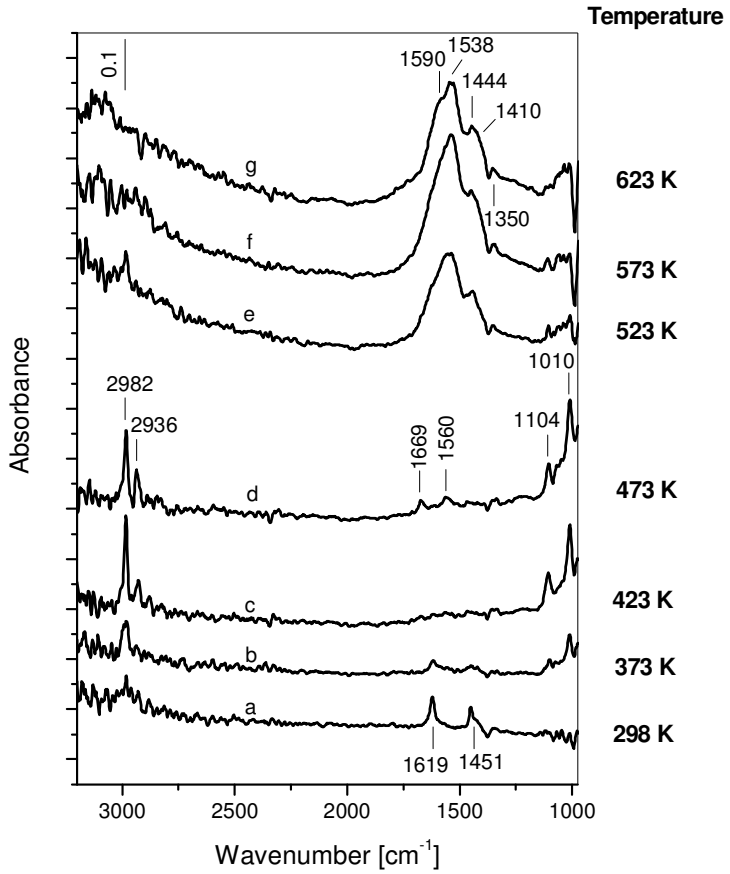


Fig. 25. FT-IR spectra collected during the exposure of the 25NbZ-P catalyst to a (3 mbar $C_3H_6$ +10 mbar $O_2$) mixture for 15 min at room temperature (a) followed by heating the isolated IR cell for 15 min at 373K (b), 423 K (c), 473 K (d), 523 K (e), 573 K (f) and 623 K (g).

propene and appearance of weak bands at 1104 and 1010 $cm^{-1}$. The shape of the absorption in the $CH_3$ stretching region has changed. At 423 K (Fig. 25, spectrum (c)) the adsorbed propene disappears almost completely. The bands at 2982 [$\nu_{as}(CH_3)$] and 2936 $cm^{-1}$ [$\nu_s(CH_3)$] detected under these conditions (Fig. 25, spectrum (c)) are characteristic of two types of isopropoxy species with the $\nu$(C–O) modes at 1104 and 1010 $cm^{-1}$, respectively [121-127]. At 473 K (Fig. 25, spectrum (d)), new absorptions at 1669 and 1560 $cm^{-1}$ are observed. The former band is attributed to the $\nu$(C=O) stretching of adsorbed acetone [122-125,128], which is formed at the expense of the isopropoxy species. This assignment is supported by the observation that the activation of propene over catalysts containing Brønsted acid sites proceeds through formation of surface isopropoxides, which are transformed into acetone followed by oxidation of the latter molecule to acetate species [122,123] – the weak band at 1560 $cm^{-1}$. When the temperature is raised to 523 K (Fig. 25, spectrum (e)), strong absorptions emerge at 1590, 1538, 1444 and 1410 $cm^{-1}$ (shoulder), which are assigned to the COO stretching vibrations of two types of acetate species [122-125,128]. The assignment of the absorption bands is summarized in Table 10.

**Table 10.** Assignments of the adsorption bands in the spectra observed during the high-temperature adsorption of $C_3H_6 + O_2$ mixture on the 25NbZ-P catalyst.

| Species | Band position, $cm^{-1}$ | Vibration |
|---|---|---|
| $C_3H_6$ (ads) | 1619<br>1451 | $\nu$C=C)<br>$\delta_{as}(CH_3)$ |
| Isopropoxide<br>(two types) | 2982, 2936<br>1104, 1010 | $\nu_{as}(CH_3)$, $\nu_s(CH_3)$<br>$\nu$(C–O) |
| Acetone (ads) | 1669 | $\nu$(C=O) |
| $CH_3COO^-$<br>(two types) | 1590, 1560 – 1538<br>1410, 1444<br>1350 | $\nu_{as}$(COO)<br>$\nu_s$(COO)<br>$\delta(CH_3)$ |

*III.2.2.3. Reactivity of the surface species formed upon room-temperature adsorption of $NO+C_3H_6+O_2$ mixture on the 25NbZ-P catalyst*

The 25NbZ-P sample was exposed to a gaseous mixture containing 18 mbar NO + 3 mbar $C_3H_6$ + 10 mbar $O_2$ at room temperature for 20 min followed by evacuation for 10 min. The spectrum obtained under these conditions is shown in Figs. 26A and 26B, spectrum (a). The broad absorption between 3600 and 2500 $cm^{-1}$ is typical of H-bonded hydroxyls and indicates that the oxidation of propene has occurred already at room temperature. The weak bands at 2990 and 2935 $cm^{-1}$ are attributed to the $\nu_{as}(CH_3)$ and $\nu_s(CH_3)$ stretching vibrations of adsorbed propene and partially oxidized derivatives of the hydrocarbon. The bands in the 1800 – 1000 $cm^{-1}$ region overlap heavily and it is difficult to propose an unambiguous assignment. Based on the spectra of adsorbed $NO_3^-$ species (Fig. 23), the absorptions at 1654, 1234, 1570, and 1275 $cm^{-1}$ are all assignable to bridged and bidentate nitrates. However, judging from the relative intensities of the nitrate bands at 1275 and 1234 $cm^{-1}$, it seems that the population of the bidentate nitrates at 1570 and 1275 $cm^{-1}$ formed in the $NO+C_3H_6+O_2$ experiment is higher than that generated during the $NO+O_2$ co-adsorption (compare with Fig. 23). This indicates that there is a competition between the nitrate species and other surface compounds for the same adsorption sites. The absorption at 1610 $cm^{-1}$ can be attributed to both bending mode of adsorbed water and $\nu_{as}(COO)$ stretching vibration of adsorbed acetate [122-125,128]. Most likely, two types of acetate species are formed which is supported by the presence of two bands at 1454 and 1420 $cm^{-1}$ corresponding to their $\nu_s(COO)$ modes [122-125,128]. The $\nu_{as}(COO)$ stretching vibration of the second acetate species is probably covered by the nitrate band at 1570 $cm^{-1}$. The absorption at 1725 $cm^{-1}$ is characteristic of a carbonyl moiety and is attributed to nitroacetone. Arguments for this assignment are given below.

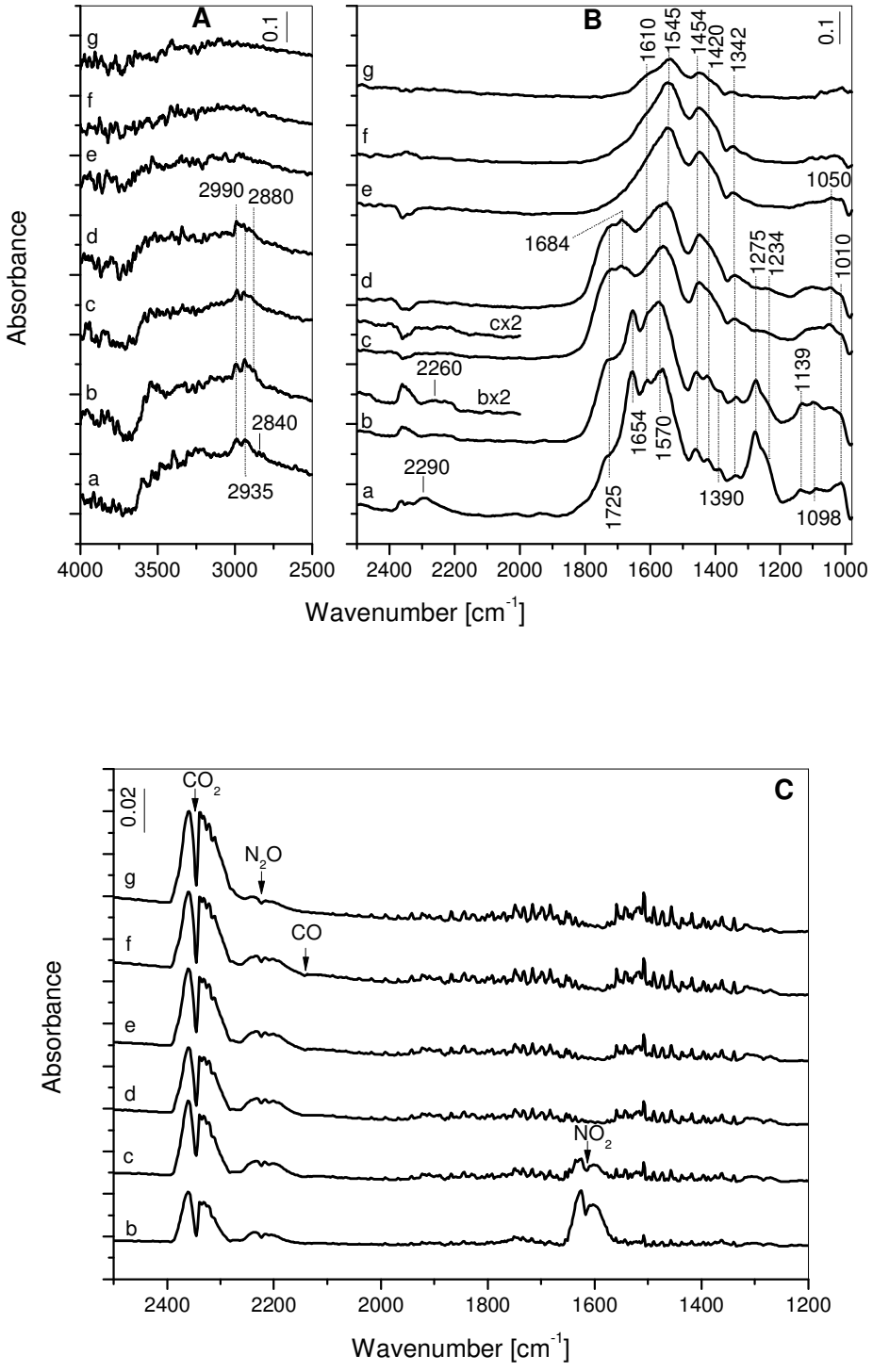


Fig. 26. FT-IR spectra collected during the exposure of the 25NbZ-P catalyst to a (18 mbar NO+3 mbar $C_3H_6$+10 mbar $O_2$) mixture at room temperature for 20 min followed by evacuation for 10 min (a) and heating the isolated IR cell for 15 min at 373 K (b), 423 K (c), 473 K (d), 523 K (e), 573 K (f) and 623 K (g). FT-IR spectra of the catalyst recorded in the 4000 – 2500 $cm^{-1}$ region (Panel A), 2500 – 980 $cm^{-1}$ region (Panel B) and gas phase spectra (Panel C).

Here it should be noted that nitroketones exhibit absorptions at 1730, 1560 and 1380 $cm^{-1}$ corresponding to the ν(C=O), $\nu_{as}(NO_2)$ and $\nu_s(NO_2)$ modes [129]. The antisymmetric $NO_2$ stretching vibration of nitroacetone is covered by the nitrate band at 1570 $cm^{-1}$ and cannot be resolved. The band at 1139 $cm^{-1}$ is assigned to the δ(CCC) mode of the nitroketone. The weak absorptions at 1098 and 1010 $cm^{-1}$ are attributed to the ν(C–O) modes of adsorbed isopropoxides [121-127]. The latter absorption has a contribution from the $\nu_s(NO_2)$ stretching vibration of the bridged nitrates. The broad band at 2290 $cm^{-1}$ is typical of NCO species adsorbed on oxide surfaces [61,130-135]. An argument in support of the assignment of the absorption at 2290 $cm^{-1}$ to a N,C-containing species is the absence of this feature in the spectra obtained during the NO+$O_2$ coadsorption (see Fig. 23B, spectrum (d) and Fig. 24A). The formation of NCO species could be associated with the transformation of nitroacetone. Weingand et al. [134] observed generation of –C=O-containing compounds at 373 K during the interaction between propene and nitrate species adsorbed on $WO_3$-$ZrO_2$. They suggested that the –C=O-containing species are converted into isocyanates with the participation of surface nitrates.

Finally, the fact that no partially oxidized hydrocarbon species were observed at room temperature during the $C_3H_6$+$O_2$ experiment (Fig. 30, spectrum (a)), indicates that the formation of surface nitrates and/or gaseous $NO_2$ during the room-temperature adsorption of NO+$C_3H_6$+$O_2$ mixture facilitates the activation of propene.

Heating the sample for 15 min at 373 K causes the following changes:

(1) increase in the concentrations of partially oxidized hydrocarbons (Fig. 26B, spectrum (b)), which is evident by the enhancement of the intensities of the bands corresponding to the isopropoxides (1098 $cm^{-1}$), acetates (1454 and 1420 $cm^{-1}$) and nitroacetone (1725 and 1139 $cm^{-1}$). This is accompanied by the appearance of a pronounced absorption at 2880 $cm^{-1}$ typical of $CH_2$ stretching vibration (Fig. 26A,

spectrum (b)). The fact that there is enhancement in the concentration of partially oxidized hydrocarbons (isopropoxides, nitroacetone, acetates) at 373 K suggests the presence of adsorbed propene at room temperature.

(2) decrease in the concentration of the surface nitrates and isocyanates (the $\nu_{as}$(NCO) band is shifted to 2260 $cm^{-1}$) which is accompanied by formation of $NO_2$ and $N_2O$ in the gas phase (Fig. 26C, spectrum (b)).

At 423 K (Fig. 26B, spectrum (c)), the nitrate bands at 1275 and 1234 $cm^{-1}$ almost vanished, which is accompanied by strong decrease in the concentration of gaseous $NO_2$ (Fig. 26C, spectrum (c)) and increase in the amount of $CO_2$ and $N_2O$. The intensities of the bands at 1139 and 1098 $cm^{-1}$ (Fig. 26B, spectrum (c)) associated with the adsorbed nitroacetone and isopropoxide are reduced and they appear as unresolved absorption between 1160 and 1070 $cm^{-1}$. The weak band at 1050 $cm^{-1}$ is assigned to the $\delta(CH_3)$ mode of the acetate species [124] whose concentration has increased significantly. The latter is evident by the observed increase in the intensities of the bands at 1454 and 1420 $cm^{-1}$ corresponding to the $\nu_s$(COO) stretching vibrations of the acetates. The absorption at 1684 $cm^{-1}$ is characteristic of the $\nu$(C=O) mode of acetone coordinated to a Lewis acid site [122-125,128]. This assignment is supported by the spectra of acetone adsorbed between 298 and 623 K (see below). Most likely, the acetone is formed below 423 K simultaneously with the nitroacetone but the strong nitrate band at 1654 $cm^{-1}$ hinders the detection of the former compound. The amount of the NCO species detected under these conditions is extremely low (Fig. 26B, traces (c) and (cx2)). The changes in the spectrum taken at 473 K (Fig. 26B, spectrum (d)) are associated with small decrease in the intensities of the absorption bands due to nitroacetone and acetone, which is evident from the subtraction spectrum (d-c). This spectrum is not shown. No appreciable amount of NCO species is detected under these conditions. It should be noted that at 473 K, $NO_2$

disappears from the gas phase. There is some increase in the amount of $CO_2$ (Fig. 26C, spectrum (d)).

Between 523 and 573 K (Fig. 26B, spectra (d) and (f)) the predominant surface species are the acetates. The surface nitrates, acetone and nitroacetone disappear at 523 K (Fig. 26B, spectrum (e)). Further increase in the temperature results in gradual decomposition of the acetate species, which is accompanied by increase in the concentration of $CO_2$ and formation of small amount of CO in the gas phase (Fig. 26C, spectra (e) to (g)). At 623 K, CO disappears and $N_2O$ is detected in lower concentration. The assignment of the absorption bands observed during the interaction of the species obtained by room-temperature adsorption of $NO+O_2+C_3H_6$ mixture over the 25NbZ-P catalyst is summarized in Table 11.

The disappearance of $NO_2$ from the spectrum taken at 473 K is in strong contrast with the results of the thermal stability of the nitrate species in the absence of propene (see Fig. 24). In the latter experiment gaseous $NO_2$ was observed in the whole temperature range between 100 and 623 K. This difference suggests that the $NO_3^-$ species, respectively activated $NO_2$ surface complex, react with the adsorbed propene and/or hydrocarbon oxygenates.

*III.2.2.4. Adsorption of acetone and its interaction with $NO_2$ over the 25NbZ-P catalyst*

In order to confirm the assignment of the absorption band at 1725 $cm^{-1}$ (Fig. 26B) to adsorbed nitroacetone, we investigated the adsorption of acetone and its interaction with $NO_2$ at elevated temperatures.

The adsorption of 1 mbar of acetone on the 25NbZ-P sample at room temperature followed by evacuation for 15 min, results in spectrum (a) shown in Fig. 27. The strong band at 1687 $cm^{-1}$ corresponds to the ν(C=O) stretching vibration of adsorbed acetone

[122-125,127]. This band is red-shifted as compared with the ν(C=O) stretching vibration of gaseous acetone and indicates that the molecule is coordinated to a Lewis acid site [122]. The intensities of the bands at 1419, 1369, 1247, 1192 and 1132 $cm^{-1}$ decrease

**Table 11.** Assignments of the absorption bands observed during the investigation of the reactivity of surface species formed upon room-temperature adsorption of $NO+C_3H_6+O_2$ mixture on the 25NbZ-P catalyst followed by heating of the evacuated IR cell in the 298 – 623 K temperature range.

| Species | Band position, $cm^{-1}$ | Vibration |
|---|---|---|
| Isopropoxide<br>(two types) | 2990, 2935<br>1098, 1010 | $\nu_{as}(CH_3)$, $\nu_s(CH_3)$<br>ν(C–O) |
| Acetone (ads) | 2990, 2935<br>1684<br>1139 | $\nu_{as}(CH_3)$, $\nu_s(CH_3)$<br>ν(C=O)<br>ν(CCC) |
| Nitroacetone (ads) | 2990, 2935<br>2880<br>1725<br>1139 | $\nu_{as}(CH_3)$, $\nu_s(CH_3)$<br>$\nu(CH_2)$<br>ν(C=O)<br>ν(CCC) |
| Bridged $NO_3^-$<br>Bidentate $NO_3^-$ | 1654, 1234, 1010<br>1570, 1275, 1010 | ν(N=O), $\nu_{as}(NO_2)$, $\nu_s(NO_2)$<br>ν(N=O), $\nu_{as}(NO_2)$, $\nu_s(NO_2)$ |
| $CH_3COO^-$<br>(two types) | 1610, 1545<br>1420, 1454<br>1342<br>1050 | $\nu_{as}(COO)$<br>$\nu_s(COO)$<br>$\delta(CH_3)$<br>$\rho(CH_3)$ |
| NCO | 2290 | $\nu_{as}(NCO)$ |

with the temperature simultaneously with the absorption at 1687 $cm^{-1}$. Therefore, all these bands are attributed to various vibrational modes of the adsorbed acetone (see Table 11). The bands at 1579 and 1450 $cm^{-1}$ observed in spectrum (a) are best assigned to bidentate acetates and correspond to the $\nu_{as}(COO)$ and $\nu_s(COO)$ modes, respectively [123-125,128].

This experimental fact indicates that the 25NbZ-P catalyst is able to oxidize the adsorbed acetone already at room temperature. Heating the isolated IR cell for 15 min at 373 K, leads to increase in the amount of the acetates at 1579 and 1450 $cm^{-1}$ at the expense of adsorbed acetone (Fig. 27, spectrum (b)). At 423 (spectrum (c)) and 473 K (spectrum (d)), the population of the $CH_3COO^-$ species grows further. This is evident by the appearance of poorly resolved absorptions at approximately 1605 and 1540 $cm^{-1}$ assigned to the $\nu_{as}(COO)$ modes of two new acetate species. The oxidation of acetone occurs in great extent at temperatures higher than 473 K, which is evident by the significant increase in the concentration of the acetate species at 523 K (Fig. 27, spectrum (e)). The heating at 623 K (spectrum (g)) does not lead to their complete removal, the acetates that give a band at 1540 $cm^{-1}$ being the most stable. Adsorbed acetone is observed up to 573 K (spectrum (f)). The assignment of the absorption bands is summarized in Table 12.

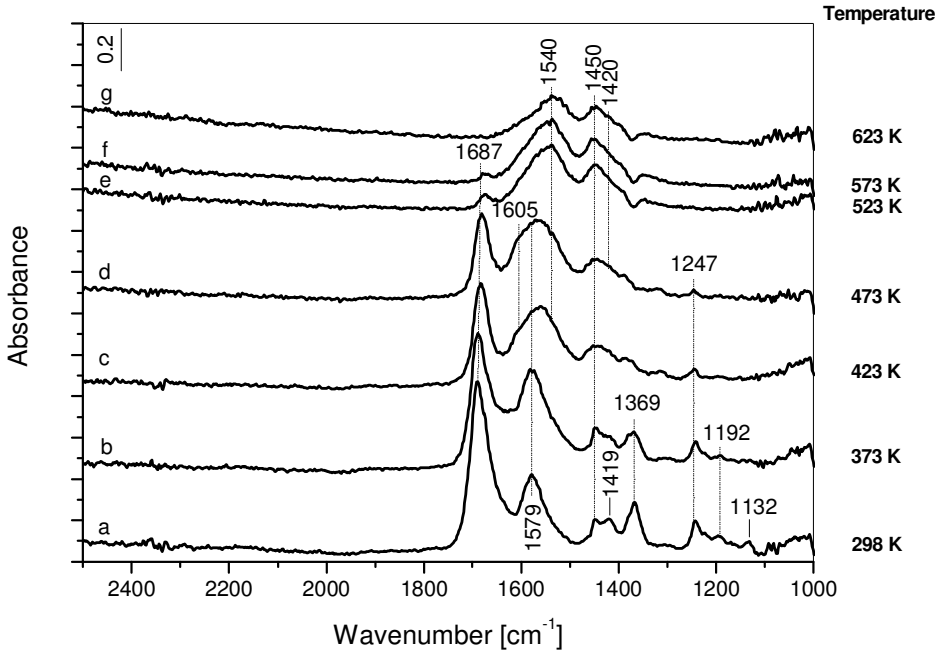


Fig. 27. FT-IR spectra of acetone (1 mbar) adsorbed on the 25NbZ-P catalyst for 10 min at room temperature followed by evacuation for 10 min (a) and after heating the isolated IR cell for 15 min at 373 K (b), 423 K (c), 473 K (d), 523 K (e), 573 K (f) and 623 K (g).

**Table 12.** Assignments of the absorption bands in the spectra observed during the high-temperature adsorption of acetone and its coadsorption with $NO_2$ on the 25NbZ-P catalyst.

| Species | Band position, $cm^{-1}$ | Vibration |
|---|---|---|
| Acetone (ads) | 2985, 2925 | $\nu_{as}(CH_3),\nu_s(CH_3)$ |
| | 1690 – 1687 | $\nu(C=O)$ |
| | 1419 – 1417 | $\delta_{as}(CH_3)$ |
| | 1370 – 1369 | $\delta_s(CH_3)$ |
| | 1247, 1192 | $\nu_{as}(CCC),\nu_s(CCC)$ |
| | 1139 | $\delta(CCC)$ |
| Nitroacetone (ads) | 2985, 2925 | $\nu_{as}(CH_3),\nu_s(CH_3)$ |
| | 2885 | $\nu(CH_2)$ |
| | 1735 | $\nu(C=O)$ |
| | 1130 | $\delta(CCC)$ |
| Bridged $NO_3^-$ | 1660, 1250, 1010 | $\nu(N=O),\nu_{as}(NO_2),\nu_s(NO_2)$ |
| Bidentate $NO_3^-$ | 1573, 1276, 1010 | $\nu(N=O),\nu_{as}(NO_2),\nu_s(NO_2)$ |
| Bidentate $CH_3COO^-$ | 1615 – 1579, 1540 | $\nu_{as}(COO)$ |
| (two types) | 1417 – 1410, 1453 – 1450 | $\nu_s(COO)$ |
| | 1350 | $\nu(CH_3)$ |
| NCO | 2260 | $\nu_{as}(NCO)$ |

The spectra shown in Fig. 28 are obtained during the interaction of $NO_2$ in the 298 – 623 K temperature range with acetone adsorbed at room temperature on the surface of the 25NbZ-P sample. The activated sample was left in contact with 1 mbar of acetone for 10 min at room temperature followed by evacuation for 10 min. Then to the IR cell 1.4 mbar of $NO_2$ were added and the isolated IR cell containing gaseous $NO_2$ was heated between 298 and 623 K for 15 min at each temperature. The spectrum detected at room temperature (Fig. 28A, spectrum (a)) contains bands at 2985 and 2925 $cm^{-1}$ due to the $\nu_{as}(CH_3)$ and $\nu_s(CH_3)$ modes of adsorbed acetone. The latter compound gives rise to the bands at 1690 ($\nu(C=O)$), 1417 ($\delta_{as}(CH_3)$) and 1370 $cm^{-1}$ ($\delta_s(CH_3)$) in the 1700 – 1000

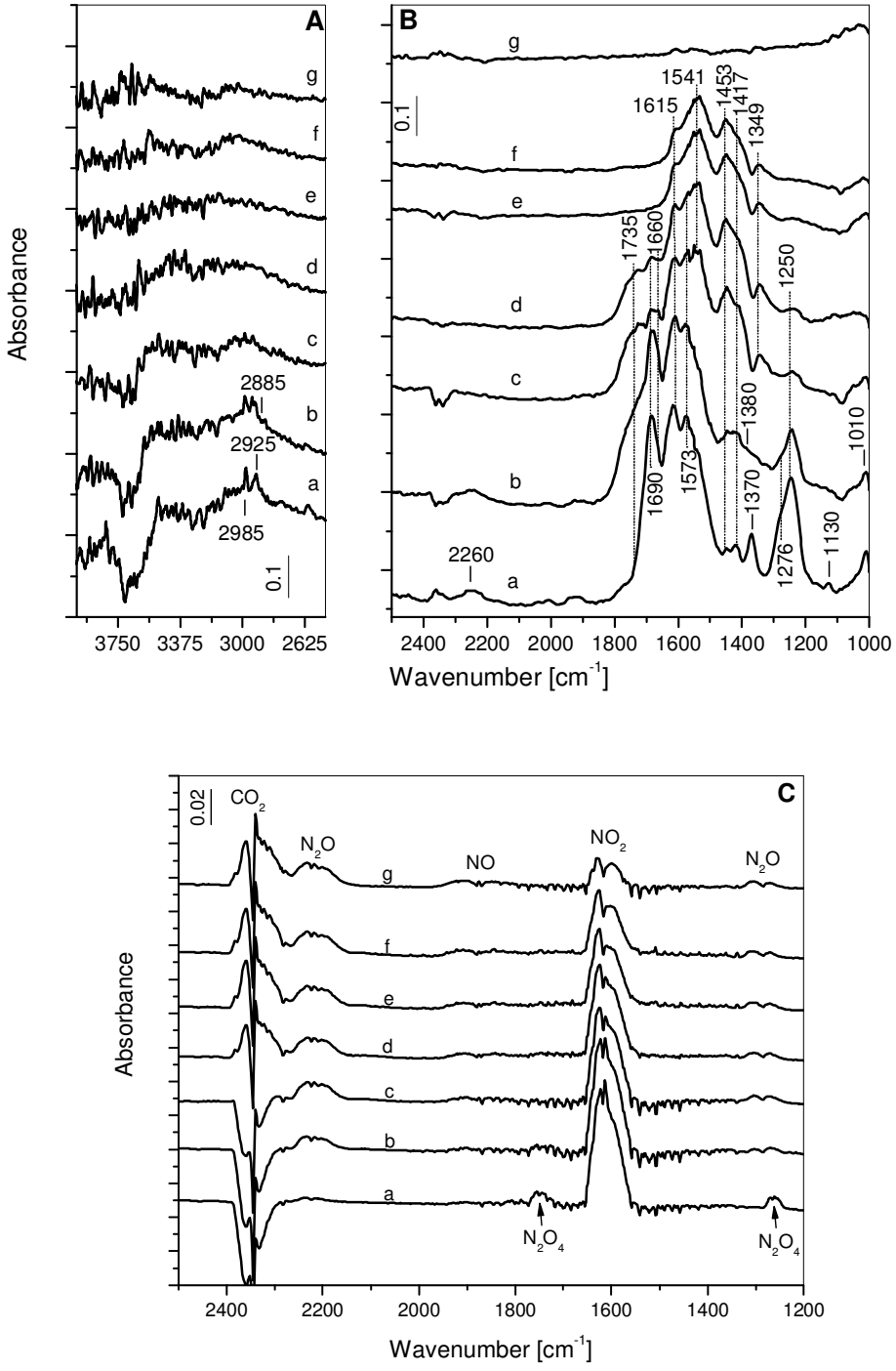


Fig. 28. FT-IR spectra of adsorbed acetone (1 mbar) on the 25NbZ-P catalyst for 10 min at room temperature followed by evacuation for 10 min and addition of 1.4 mbar $NO_2$ (a) and heating the isolated IR cell for 15 min at 373 K (b), 423 K (c), 473 K (d), 523 K (e), 573 K (f) and 623 K (g). FT-IR spectra of the catalyst recorded in the 4000 – 2500 $cm^{-1}$ region (Panel A) and 2500 – 1000 $cm^{-1}$ region (Panel B) and gas phase spectra (Panel C).

$cm^{-1}$ region (Fig. 28B, spectrum (a)). The weak absorption at 1453 $cm^{-1}$ suggests formation of acetate species and is attributed to the $\nu_s(COO)$ mode. As shown above, the bands at 1660 and 1250 $cm^{-1}$ and at 1573 and 1276 $cm^{-1}$ are due mainly to bridged and bidentate nitrate species ($\nu(N=O)$ and $\nu_{as}(NO_2)$ modes). Weak band with maximum at 2260 $cm^{-1}$ and shoulder at approximately 1735 $cm^{-1}$ are detected. As in the case of adsorbed acetone in the absence of $NO_2$ (Fig. 27), the increase in the temperature to 373 K causes increase in the amount of acetate species, which is evident by the enhancement of the intensities of the bands at 1453 and 1417 $cm^{-1}$ (Fig. 28B, spectrum (b)). In addition, there is a strong increase of the absorption at 1735 $cm^{-1}$ and decrease in the intensity of the band at 2260 $cm^{-1}$. The latter two bands are not observed during the adsorption of acetone in the absence of $NO_2$ (see Fig. 27). This confirms the assumption made above that the absorption at 1735 $cm^{-1}$ corresponds to nitroacetone and its transformation leads to the generation of NCO species giving rise to the absorption at 2260 $cm^{-1}$. The formation of nitroacetone from acetone is supported by the observed strong decrease in the intensity of the band at 1370 $cm^{-1}$ due to the $\delta_s(CH_3)$ mode of adsorbed acetone (Fig. 28B, spectrum (b)) and appearance of a pronounced shoulder at 2885 $cm^{-1}$ corresponding to the $\nu(CH_2)$ stretching vibration (Fig. 36A, spectrum (b)). This indicates that substitution of nitro group(s) for hydrogen atom(s) in the methyl group(s) of acetone has occurred.

The development of the absorption bands between 423 and 623 K is analogous to that observed during the adsorption of $NO+C_3H_6+O_2$ mixture on the surface of the 25NbZ-P catalyst (compare with Fig. 26B). However, no NCO species are detected at 423 K in the presence of gaseous $NO_2$ (compare spectra (c) in Figs. 26B and 28B). The acetone and its nitro substituent disappear from the surface of 25NbZ-P sample at 523 K (Fig. 28B, spectrum (e)). The spectra detected at this temperature and 573 K (spectrum (f)) contain bands due mainly to adsorbed acetate species (1615, 1541, 1453, 1417 and

1349 $cm^{-1}$). The decomposition of surface acetates begins at 523 K, which causes decrease in their concentration and disappearance at 623 K. The spectra of the gas phase taken between 298 and 623 K are shown in Fig. 28C. The amount of $NO_2$ gradually decreases with the temperature which could be attributed to shift of the equilibrium $NO_2 \leftrightarrow NO + 0.5O_2$ to the right and interaction of $NO_2$ with the adsorbed acetone, nitroacetone and NCO species. The latter processes account for the formation of significant amount of $CO_2$ at 473 K (Fig. 28C, spectrum (d)).

Table 12 summarizes the assignment of the absorption bands observed in the spectra detected during the adsorption of acetone and its co-adsorption with $NO_2$ on the 25NbZ-P sample.

*III.2.2.5. Adsorption of 1-Nitropropane on the 25NbZ-P catalyst*

We studied the adsorption of 1-nitropropane and its transformation over the 25NbZ-P catalyst at high temperatures. Formation of nitropropane has been often observed during the interaction of $NO+C_3H_6+O_2$ mixtures with oxide catalysts [8,61,63,66,80,134,136-138,140-142,144]. This compound transforms at higher temperatures to NCO species, which is considered as reaction intermediate [8,57,137-140,145]. The goal is to confirm that the nitroacetone formed on the 25NbZ-P catalyst is the origin of the NCO species.

The adsorption of N-nitropropane (0.1 mbar) on the 25NbZ-P sample at room temperature followed by evacuation for 10 min results in spectrum (a) shown in Fig. 29. The bands at 1680, 1423, 1375, 1244 and 1048 $cm^{-1}$ are attributed to the $\nu$(N=O), $\delta_{as}(CH_3)$, $\delta_s(CH_3)$, $\nu_{as}$(CCC) and $\nu$(CO) modes of nitritopropane, respectively. It shows that the adsorbed nitropropane is not stable on the surface of the 25NbZ-P catalyst and isomerizes immediately to nitritopropane at room temperature. The heating between 373

and 623 K causes the oxidation of the adsorbed nitritopropane to surface acetates (spectra b-g in Fig. 29) and above 473 K the spectra contain only the characteristic bands of the latter species. No NCO groups are detected in the whole temperature range. Thus, these results confirm that the source of isocyanates over the 25NbZ-P sample is the nitroacetone. The assignment of the absorption bands is summarized in Table 13.

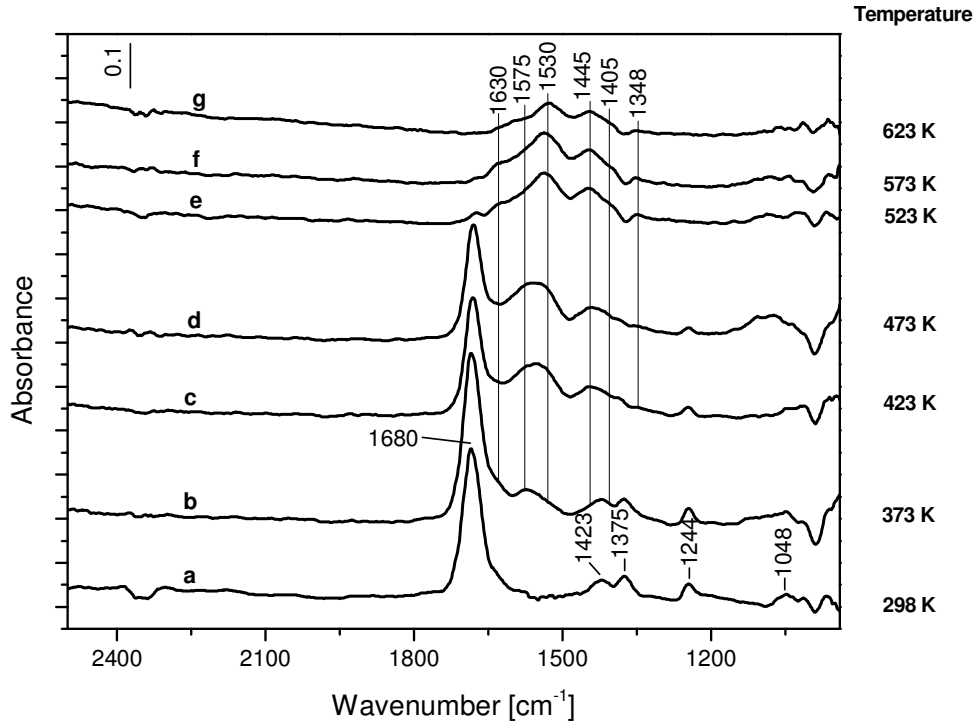


Fig. 29. FT-IR spectra of 1-nitropropane (0.1 mbar) adsorbed on the 25NbZ-P catalyst for 10 min at room temperature followed by evacuation for 10 min (a) and after heating the isolated IR cell for 15 min at 373 K (b), 423 K (c), 473 K (d), 523 K (e), 573 K (f) and 623 K (g).

*III.2.2.6. Reactivity of the surface species formed upon room-temperature adsorption of $NO+C_3H_6+O_2$ mixture on the 0.1Pd/25NbZ-P catalyst*

Fig. 30 shows the results of the reactivity of surface species formed upon room-temperature adsorption of ($NO+O_2+C_3H_6$) mixture on the 0.1Pd/25NbZ-P catalysts in the 298 – 623 K temperature range. The experimental conditions are the same as those for the

Pd-free sample. The gas phase spectra (not shown) and the band envelope in the 1800 – 1000 $cm^{-1}$ range at different temperatures (Fig. 30B) are similar to that observed for the Pd-free sample. The same types of surface complexes (isocyanates, nitrates, isopropoxide,

**Table 13.** Assignments of the adsorption bands in the spectra observed during the high-temperature adsorption of 1-Nitropropane on the 25NbZ-P catalyst.

| Species | Band position, $cm^{-1}$ | Vibration |
|---|---|---|
| Nitritopropane | 1680 | $\nu$(N=O) |
| | 1423 | $\delta_{as}(CH_3)$ |
| | 1375 | $\delta_s(CH_3)$ |
| | 1244 | $\nu_{as}$(CCC) |
| | 1048 | $\nu$(C–O) |
| $CH_3COO^-$ | 1630, 1575, 1530 | $\nu_{as}$(COO) |
| (three types) | 1445, 1405 | $\nu_s$(COO) |
| | 1345 | $\delta(CH_3)$ |

nitroacetone and acetates) are formed. The identical frequencies of the $\nu_{as}$(NCO) modes observed on both samples shows that the NCO species at 2290 $cm^{-1}$ are located on the support. The isocyanates disappear at 373 K (Fig. 30B, spectrum (b)). At 423 K a new band at 2182 $cm^{-1}$ is detected on the 0.1Pd/25NbZ-P sample (Fig. 30B, spectrum (c)), which is attributed to Pd–NCO species [25]. Other possibility for the interpretation of the band at 2182 $cm^{-1}$ is to assign it to CO adsorbed on Pd sites. This assumption was checked by adsorbing CO (10 mbar) on the 0.1Pd/25NbZ-P sample in the 373 – 623 K temperature range (the spectra are not shown). At 423 K only one absorption band at1940 $cm^{-1}$ was detected between 2400 and 1800 $cm^{-1}$, which disappeared at 523 K. This band is characteristic of CO bridging two Pd sites [25,119]. In addition, between 423 and 523 K, no absorption bands were observed in the 2400 – 1800 $cm^{-1}$ region during the contact of a (5 mbar NO+10 mbar CO) mixture with the 0.1Pd/25NbZ-P sample. This fact rules out

the possibility that a reaction between NO and CO over the 0.1Pd/25NbZ-P sample could lead to the formation of Pd–NCO species.

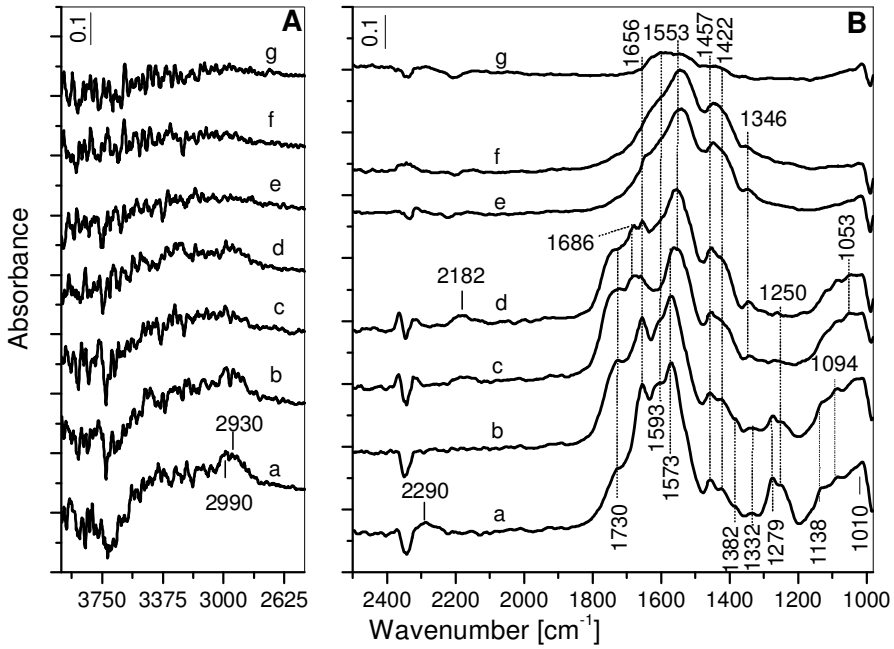


Fig. 30. FT-IR spectra collected during the exposure of the 0.1Pd/25NbZ-P catalyst to a (18 mbar NO+3 mbar $C_3H_6$+10 mbar $O_2$) mixture at room temperature for 20 min followed by evacuation for 10 min (a) and heating the isolated IR cell for 15 min at 373 K (b), 423 K (c), 473 K (d), 523 K (e), 573 K (f) and 623 K (g). FT-IR spectra of the catalyst recorded in the 4000 – 2500 $cm^{-1}$ region (Panel A) and 2500 – 980 $cm^{-1}$ region (Panel B).

It can be proposed that at temperatures higher than 373 K, some of the isocyanates located on the support migrate on the Pd sites. The concentration of the Pd–NCO species increases at 473 K (Fig. 30B, spectrum (d)) and they vanish at 523 K (spectrum (e)) together with the nitroacetone and the remaining surface nitrates. The assignment of the absorption bands is proposed in Table 14.

**Table 14.** Assignments of the absorption bands observed during the investigation of the reactivity of surface species formed upon room-temperature adsorption of $NO+C_3H_6+O_2$ mixture on the 0.1Pd/25NbZ-P catalyst followed by heating of the evacuated IR cell in the 298 – 623 K temperature range.

| Species | Band position, $cm^{-1}$ | Vibration |
|---|---|---|
| Isopropoxide<br>(two types) | 2990, 2930<br>1094, 1010 | $\nu_{as}(CH_3)$, $\nu_s(CH_3)$<br>$\nu(C–O)$ |
| Acetone (ads) | 2990, 2930<br>1686<br>1332, 1138 | $\nu_{as}(CH_3)$, $\nu_s(CH_3)$<br>$\nu(C=O)$<br>$\delta_s(CH_3)$, $\delta(CCC)$ |
| Nitroacetone (ads) | 2990, 2930<br>1730<br>1332, 1138 | $\nu_{as}(CH_3)$, $\nu_s(CH_3)$<br>$\nu(C=O)$<br>$\delta_s(CH_3)$, $\delta(CCC)$ |
| Bridged $NO_3^-$<br>Bidentate $NO_3^-$ | 1656, 1250, 1010<br>1573, 1279, 1010 | $\nu(N=O)$, $\nu_{as}(NO_2)$, $\nu_s(NO_2)$<br>$\nu(N=O)$, $\nu_{as}(NO_2)$, $\nu_s(NO_2)$ |
| $CH_3COO^-$<br>(two types) | 1593, 1553<br>1457, 1422<br>1346, 1053 | $\nu_{as}(COO)$<br>$\nu_s(COO)$<br>$\delta(CH_3)$, $\rho(CH_3)$ |
| $NCO/Zr_6Nb_2O_{17}$<br>Pd–NCO | 2290<br>2182 | $\nu_{as}(NCO)$<br>$\nu_{as}(NCO)$ |

*III.2.2.7. Summary of the Results on the Mechanistic studies on the $C_3H_6$-SCR of $NO_x$ on the 25NbZ-P sample*

The FT-IR spectra obtained during the adsorption of ($NO+C_3H_6+O_2$) and (acetone + $NO_2$) mixtures on the 25NbZ-P catalyst show formation of NCO species already at room temperature. The surface isocyanates are considered to be reactive intermediates in the selective reduction of $NO_x$ with hydrocarbons [8,57,137-140,145]. In the case of supported copper catalysts, which are among the most active non-noble metal oxide catalysts in the selective reduction of $NO_x$ with propene, the formation of NCO species is

detected at higher temperatures (423 – 523 K) [57,63,80,131,141,146,147]. Their generation through transformation of organic nitro compound, $C_xH_yNO_z$, has been proposed for various catalytic systems [8,61,66,80,133,134,137-144]. The results of the nitropropane adsorption on the 25NbZ-P sample (Fig. 29) show that it immediately isomerizes to nitritopropane at room temperature, then it is oxidized to surface acetates upon the heating between 373 and 623 K and above 473 K the spectra contain only the characteristic bands of the latter species. No NCO groups are detected in the whole temperature range. Therefore, it can be proposed that the source of isocyanates over the 25NbZ-P sample is the nitroacetone. Pearson et al. [144] have shown that in a weak basic medium nitroacetone produces aci-anion of nitromethane ($CH_2NO_2^-$) and acetate species. The former compound in turn can transform into NCO groups [8,134,140,143,144]. Most likely, the decomposition of nitroacetone to aci-nitromethane and $CH_3COO^-$ species occurs on basic $O^{2-}$ sites of the 25NbZ-P sample:

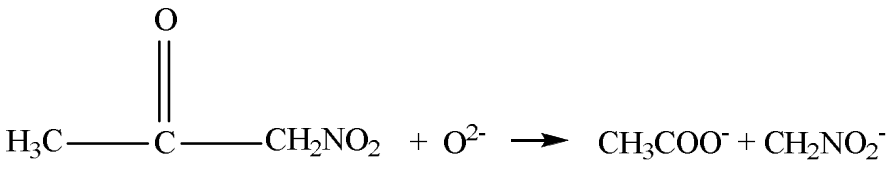

(1)

The characteristic vibrations of aci-nitromethane fall in the 1650 – 1200 $cm^{-1}$ region [134,143,144] and if they are present, they cannot be located due to overlapping with the nitrate-carboxylate bands. However, the product of aci-nitromethane transformation, the NCO species, is clearly observable at 2290 – 2260 $cm^{-1}$ in the spectra taken at 298 and 373 K (Figs. 26B and 28B, spectra (a) and (b)). It is well known that the surface isocyanates react easily with $NO+O_2$ mixtures and/or $NO_2$ yielding molecular nitrogen and $N_2O$ as reaction products [8,80,131,133,135,137,138,142,145]. This fact can account for the disappearance of the NCO species and $NO_2$ at temperatures higher than 373 – 423 K. Therefore, we are of the opinion that the low-temperature activity of the

25NbZ-P catalyst is associated with the nature of the organic nitro compound formed during the course of the reaction. Most probably, the transformation route of nitropropane to isocyanate species over the majority of oxide-based catalysts is energetically more expensive than that of nitroacetone via aci-nitromethane to NCO as proposed for the 25NbZ-P catalyst.

The experimental results show that the nitroacetone and acetone disappear simultaneously at 523 K (Figs. 26B and 28B, spectrum (e)). It can be proposed that under these conditions both compounds are further oxidized to acetates. The latter species begin to decompose at 523 K causing an increase in the amount of $CO_2$ (Figs. 26C and 28C, spectrum (e)). It seems that the nitroacetone and acetone have the same thermal stability when adsorbed on the 25NbZ-P catalyst. As shown above, the oxidation of adsorbed acetone to $CH_3COO^-$ species occurs in large extent at 523 K (see Fig. 27). In other words, we assume that the nitroacetone can undergo transformations through two parallel reactions: path (1) consisting of acid-base reaction (reaction 1) and path (2) involving the oxidation of nitroacetone. The latter process is important most likely at temperatures higher than 473 K. The products of high-temperature transformation of nitroacetone would be $NO_x$ species, presumably $NO_2$ or surface nitrate, in addition to the acetates and $CO_x/H_2O$. The $NO_2/NO_3^-$ surface complex formed in path (2) can be involved in interactions with propene and/or surface isocyanates.

A mechanism for the surface reaction of propene and $NO_x$ species adsorbed on the 25NbZ-P catalyst, deduced from the in situ FT-IR measurements, is proposed in Scheme 2. It is assumed that the interaction of the isopropoxide species with the surface nitrates or/and activated $NO_2$ generates the nitroacetone. It should be noted that it is difficult to present direct evidence that the NCO species react with the surface $NO_3^-/NO_2$ complexes. The experimental results show that the NCO species are somewhat more stable in the

absence of gaseous $NO_2$ and they produce a very weak band between 2300 and 2150 $cm^{-1}$ at 423 K (Fig. 26B, spectrum (c)). This absorption is absent in the spectrum taken at 423 K upon $NO_2$ atmosphere (Fig. 28B, spectrum c) implying that the isocyanates react with $NO_2$ or activated $NO_2$ surface complex. Although the experimental conditions of the FT-IR investigation and catalytic test are different, it can be proposed that the nitroacetone and isocyanates could be the main reaction intermediates. This is supported by the facts that the NCO consumption is observed by in situ FT-IR spectroscopy already at 373 K and the $NO_x$ reduction over the 25NbZ-P catalyst with propene is significant at 453 K (~30% of $NO_x$ conversion). This assumption is in agreement with the currently accepted general mechanism of HC-SCR of $NO_x$ [8,137,138], in which the participation of NCO species formed via organo-nitrogen compound is observed more readily under static conditions [133].

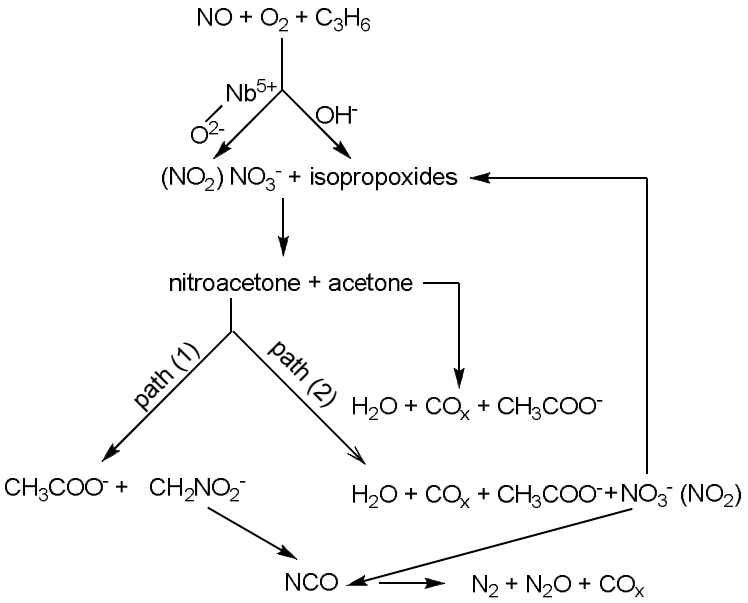


Scheme 2

The disappearance of the isocyanates on the unpromoted 25NbZ-P catalyst already at 373 K implies that the NCO species coordinated to the cationic sites of the mixed oxide have higher reactivity than that of the Pd–NCO species. The NCO species stabilized on the Pd sites need higher temperature (523 K) in order to participate in the reaction. The Pd–NCO species are present in the spectra as long as adsorbed nitroacetone exists on the surface (473 K, spectrum (d) in Fig. 30). The simultaneous disappearance of the NCO groups and nitroacetone at 523 K (Fig. 30, spectrum (e)) supports the assumption made above (see Scheme 2) that the NCO species react with the $NO_2/NO_3^-$ surface complex produced during the oxidation of nitroketone.

Based on the in situ FT-IR results, it is difficult to propose an unambiguous explanation about the lower $NO_x$ conversion observed over the Pd-containing sample (Fig. 20). It is possible that the surface concentration of the $O^{2-}$ ions involved in the transformation of nitroacetone to aci-nitromethane (reaction 2) decreases after the deposition of Pd(II) as a result of formation of $Pd(O)_n^{2+}$ entities. This could lead to lowering of the concentration of the NCO species, which causes decrease in the $NO_x$ conversion. This assumption is supported by the somewhat lower intensity of the NCO band observed at room temperature on the 0.1Pd/25NbZ-P sample than that in the case of the Pd-free sample (compare Figs. 26 and 30, spectra a).

The results of the investigation show that the catalytic properties of the $Zr_6Nb_2O_{17}$ solid solution could be of interest regarding the development of noble metal-free, low-temperature catalyst for the SCR of $NO_x$ with hydrocarbons.

III.2.3. FT-IR Study on the Effect of $SO_2$ on the SCR of $NO_x$ with Propene over the 25NbZ-P Catalyst

*III.2.3.1. Co-adsorption of $SO_2$+$O_2$ over $ZrO_2$ and 25NbZ-P samples*

In order to find out the effect of modification of zirconia with Nb(V) on the formation of surface $SO_x$ species we investigated the adsorption of (0.5 mbar $SO_2$+10 mbar $O_2$) mixture on $ZrO_2$ and 25NbZ-P samples for 15 min at various temperatures. The predominant surface $SO_x$ compounds observed in the spectra of zirconia taken below 473 K are adsorbed $SO_3^{2-}$ species (the spectra are not shown). The weak band at 1362 $cm^{-1}$

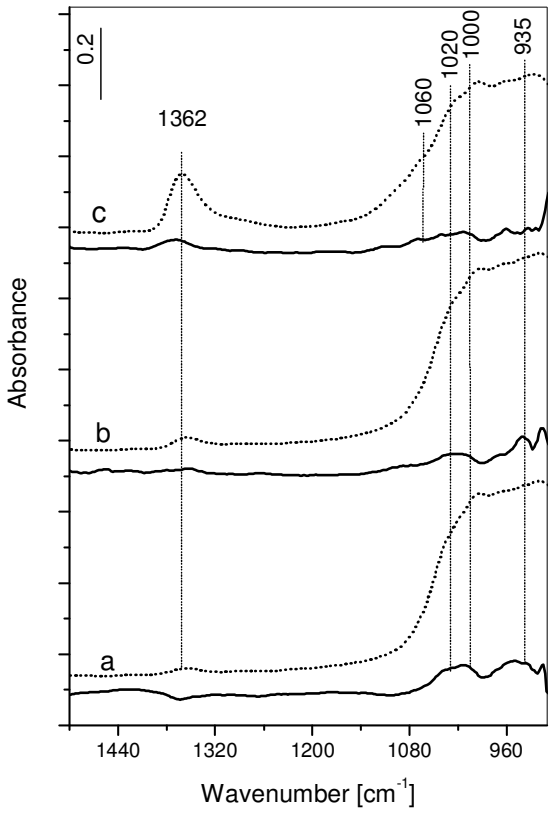


Fig. 31. FT-IR spectra collected during the exposure of zirconia (dotted line) and 25NbZ-P samples (solid line) to a (0.5 mbar $SO_2$ + 10 mbar $O_2$) mixture for 10 min at 473 K (a), 523 K (b) and 573 K (c).

detected on zirconia at 473 K (Fig. 31, dotted spectrum (a)) is characteristic of the high-frequency component of the split $\nu_3$ mode of highly covalent surface sulfates [92,148,149]. The strong absorption between 1100 and 900 $cm^{-1}$ with maxima at 1000 and 935 $cm^{-1}$ is present also in the spectra detected below 473 K and is attributed to vibrational modes of $SO_3^{2-}$ ions coordinated through the S atom to the surface [90]. The heating at 573 K causes significant increase in the intensity of the sulfate band at 1362 $cm^{-1}$ at the expense of the absorption corresponding to the sulfite species (Fig. 31, dashed spectrum (c)). The band at 1000 $cm^{-1}$ is attributed to the $\nu_1$ mode, whereas the bands at 1020 and 935 $cm^{-1}$ correspond to the split $\nu_3$ stretching vibrations of $SO_3^{2-}$ ions [90]. The shoulder at 1060 $cm^{-1}$ is assigned to the low-frequency component of the split $\nu_3$ mode of the $SO_4^{2-}$ groups [92,148,149]. These results show that noticeable oxidation of $SO_2$ over zirconia starts at 573 K. In this process, most likely, surface oxygen vacancies are involved facilitating the activation of $O_2$. Between 473 and 573 K, the same type of surface $SO_x$ species are detected on the 25NbZ-P sample, however with significantly lower concentrations (Fig. 31, solid traces). This indicates that the $SO_x$ species are coordinated to the exposed $Zr^{4+}$ ions on the surface of 25NbZ-P sample and the incorporation of Nb(V) ions into zirconia suppresses the oxidation of $SO_2$ to $SO_3$.

*III.2.3.2. Co-adsorption of $C_3H_6$+$O_2$+$SO_2$ on the 25NbZ-P catalyst*

Fig. 32 shows the development of the spectra in the 298 – 573 K temperature range obtained during the contact of the catalyst with a gas mixture containing 0.5 mbar of $SO_2$, 3 mbar of $C_3H_6$ and 10 mbar of $O_2$. Upon adsorption at room temperature bands characteristic of physisorbed $SO_2$ (1330 $cm^{-1}$), adsorbed propene (1640 $cm^{-1}$) and surface sulfites (strong absorption between 1030 and 930 $cm^{-1}$) are observed in Fig. 32, spectrum a. The intensity of the band at 1640 $cm^{-1}$ in Fig. 32, spectrum a is weaker than that of the

band at 1619 $cm^{-1}$ in Fig. 25, spectrum a. It implies that both, $C_3H_6$ and $SO_2$, compete for the same adsorption sites. Heating the closed IR cell at 373K for 15 min (Fig. 32, spectrum b) causes the appearance of two weak bands at 1672 and 1618 $cm^{-1}$, which are due to the ν(C=O) mode of acetone and $\nu_{as}$(COO) mode of acetate (or bending mode of adsorbed water), respectively. The absorption between 3000 and 2860 $cm^{-1}$ is assigned to

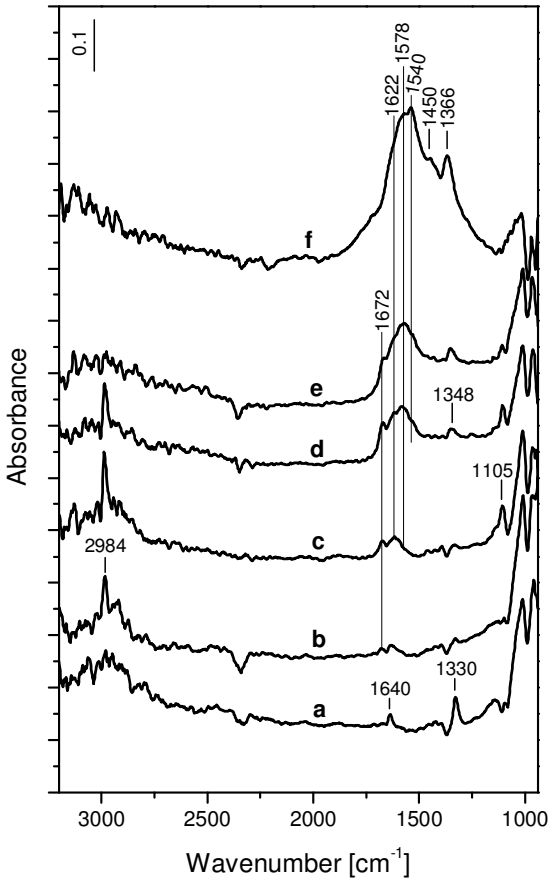


Fig. 32. FT-IR spectra recorded during the exposure of 25NbZ-P sample to a gas mixture (0.5 mbar $SO_2$ + 3 mbar $C_3H_6$ + 10 mbar $O_2$) for 20 min at rt (a) followed by heating the isolated IR cell for 15 min at 373 K (b), 423 K (c), 473 K (d), 523 K (e) and 573 K (f).

the $CH_3$ stretching vibrations, which indicates the presence of isopropoxy species. Their characteristic ν(C–O) mode cannot be detected due the strong absorptions of sulfite species covering the 1070 – 1000 $cm^{-1}$ range. At 423 K (Fig. 32, spectrum c) the surface

concentration of acetone and acetate species increases. Moreover, the ν(C–O) mode of isopropoxy species appears as weak band at 1105 $cm^{-1}$. The intensity of the absorption between 1070 and 1000 $cm^{-1}$ is strongly reduced. At 473 K (Fig. 32, spectrum d) the oxidation of $SO_2$ starts producing $SO_4^{2-}$ species identified by the band at 1348 $cm^{-1}$. As the temperature increases, the amount of surface acetates (the bands at 1622, 1578, 1540, 1450 and 1366 $cm^{-1}$) and sulfate species (the band at 1366 $cm^{-1}$) increases. It can be concluded that the activation of propene is facilitated in the presence of $SO_2$.

*III.2.3.3. Effect of $SO_2$ on the $C_3H_6$+NO+$O_2$ surface reaction*

Fig. 33 compares the spectra of the 25NbZ-P sample obtained at various temperatures during the adsorption for 15 min of gaseous mixture containing (2 mbar $C_3H_6$ + 6 mbar NO + 4 mbar $O_2$) in the absence (dotted lines) and presence of 0.5 mbar $SO_2$ (solid lines). The spectra are detected in the presence of gaseous phase and are gas-phase corrected. The spectra taken at room temperature, contain weak absorption at 2270 $cm^{-1}$ indicating the formation of NCO species in both cases, in the presence and absence of $SO_2$ (Fig. 33, spectra (a)). The broad band at 1900 $cm^{-1}$ is characteristic of adsorbed $N_2O_3$ (see Fig. 23). Some amounts of adsorbed nitroacetone (1740 $cm^{-1}$) and acetone (1680 $cm^{-1}$) are observed as well. The difference between both spectra is in the concentration of the surface nitrates (bands at 1655, 1610, 1570, 1277 and 1245 $cm^{-1}$), which is lower in the presence of $SO_2$. In addition, the appearance of absorption bands at 1346 and 1044 – 1013 $cm^{-1}$ reveal formation of surface sulfates at room temperature and correspond to the split $\nu_3$ mode of multidentate $SO_4^{2-}$ groups coordinated to $Zr^{4+}$ sites [92,148,149]. No sulfite species are observed, which exhibits vibrational modes below 1000 $cm^{-1}$. This indicates that the nitrate species or activated $NO_2$ lower significantly the oxidation temperature of $SO_2$. Most likely, the sulfates species formed block the active

sites ($Nb^{5+}$ ions) for the oxidation of NO to $NO_2$ leading to decrease in the concentration of the surface nitrates. As a consequence, the amount of nitroacetone formed at 423 K in the presence of $SO_2$ is lower than that in the absence of the poison (Fig. 33, spectra (b)). The spectrum taken at 473 K in the presence of $SO_2$ (Fig. 33, spectrum c, solid trace) shows further increase in the amount of sulfate species, which is evident by the enhancement of the absorptions at 1044 and 1013 $cm^{-1}$. The decrease in the surface concentrations of acetone and nitroacetone at 473 K measured against the concentrations

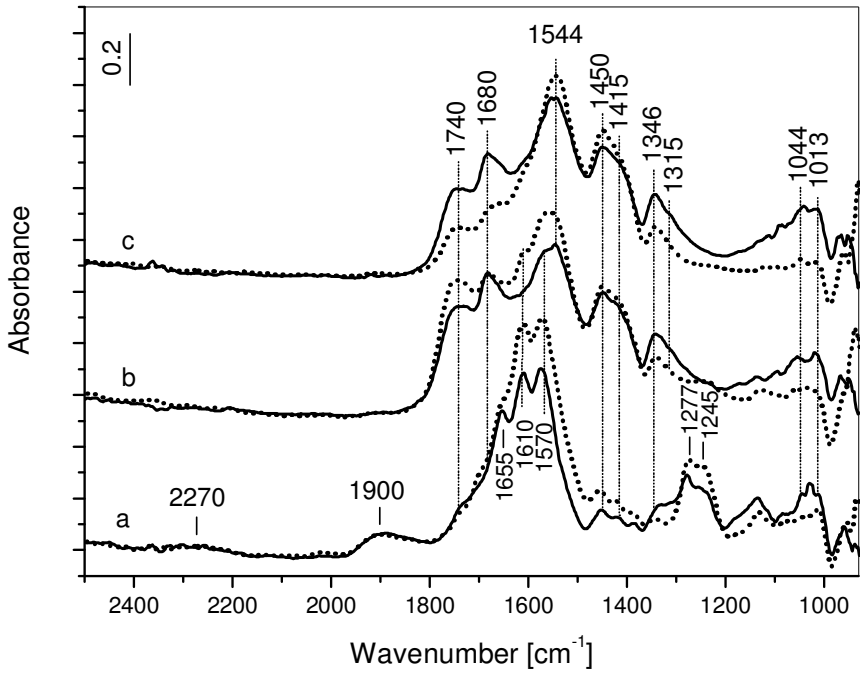


Fig. 33. FT-IR spectra of the 25NbZ-P sample collected during the exposure for 10 min to a (2 mbar $C_3H_6$ + 6 mbar NO + 4 mbar $O_2$) mixture in the absence (dotted line) and presence of 0.5 mbar $SO_2$ (solid line) at 298 K (a), 423 K (b) and 473 K (c).

at 423 K is considerably smaller than the corresponding decrease observed in the absence of $SO_2$ (Fig. 33, compare spectra (b) and (c)). This fact leads to the conclusion that the surface sulfates hinder the transformation of nitroacetone to NCO species. According to the mechanism proposed above (Scheme 2), the low concentration of nitroacetone and

hindrance of its transformation will result in low concentration of the NCO species and decrease in the catalyst activity (see Fig. 21).

It should be pointed out that, according to the catalytic activity measurements (section III.2.1) the mechanism proposed for $SO_2$ poisoning should be effective at high concentration of $SO_2$.

## III.3. Investigation of the possibility for application of the 25NbZ-P and 20WN873 samples as catalysts for alcohol transformations

Solid acids can find applications as catalysts for dehydration and dehydrogenation of alcohols [35-38,150-152]. This section describes the results of interaction of propan-2-ol (iso-propanol) with the 25NbZ-P and 20WN873 samples at various temperatures in the absence and presence of oxygen in order to evaluate their potential as catalysts for transformations of alcohols. The interaction of $ZrO_2$ with isopropanol has been studied as well for comparison. Among the materials investigated, the 25NbZ-P and 20W873 samples contain the highest amount of Brønsted acid sites.

Two main paths for alcohol transformation have been established [153]:

(i) dehydration with the formation of alkene and water, and

(ii) dehydrogenation with the formation of carbonyl compound(s) and hydrogen.

The following mechanisms for the dehydration of iso-propanol leading to the formation of propene have been proposed [153-159]:

1. With the participation of a Brønsted acid site.

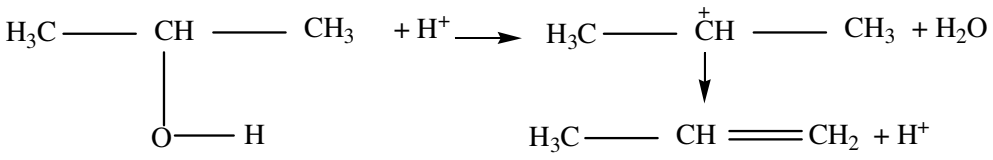

Scheme 3

In this mechanism a carbenium ion is produced with the intermediacy of $H^+$ ion.

2. Involvement of acid-base sites.

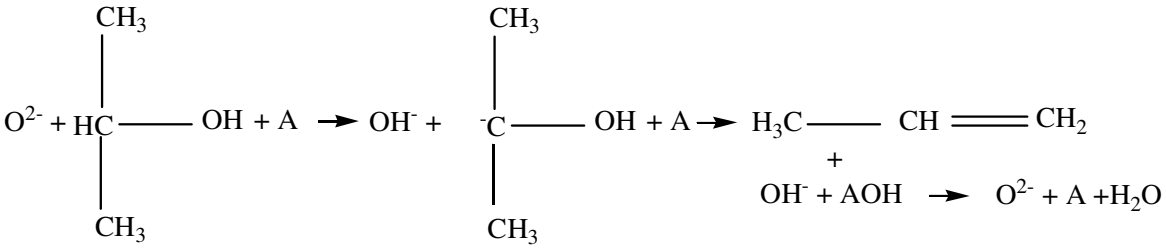

Scheme 4

where A can be either a Lewis acid site (cus metal cation) or Brønsted acid site ($H^+$). In this mechanism a carbanion is formed by the participation of strong basic site ($O^{2-}$)

The dehydrogenation of isopropanol is promoted by strong basic (nucleophilic) sites (Brønsted and/or Lewis) [153-159]. Scheme 3 incorporates the main ideas proposed in the literature, where the basic sites are the oxide ions:

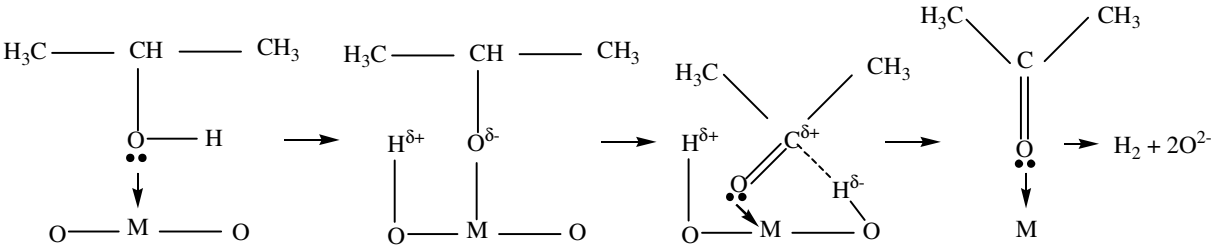

Scheme 5

III.3.1. Adsorption of Propan-2-ol over the $ZrO_2$ sample

The adsorption of isopropanol (1 mbar) on the $ZrO_2$ sample at room temperature followed by evacuation for 10 min results in the spectrum a shown in Fig. 34A. Three types of isopropoxy species [121-127] give rise to all absorptions (see Table 15 for the assignments) except for the bands at 1680 and 1622 $cm^{-1}$. The former is due to the ν(C=O) stretching vibration of adsorbed acetone [122-125,128], whereas the latter one is attributed to adsorbed water. The adsorbed acetone disappears at 523 K (Fig. 34A,

spectrum e). The gas phase spectrum taken at the same temperature indicates the presence of propene. The latter molecule is identified by its strongest absorption at 912 $cm^{-1}$. These results reveal that zirconia used in this study is characterized by a low concentration of strong basic sites ($O^{2-}$/$OH^-$ ions), which lead to generation of some amount of acetone already at room temperature and contains mainly strong acid sites causing the transformation of isopropanol to propene at high temperatures. Since zirconia does not possess Brønsted acidity (see Section *III.1.1.5. Brønsted acidity*), the strong acid sites promoting the formation of propene are the cus $Zr^{4+}$ ions.

**Table 15.** Assignments of the adsorption bands in the spectra observed during the high-temperature adsorption of propan-2-ol on the $ZrO_2$ sample.

| Species | Band position, $cm^{-1}$ | Vibration |
|---|---|---|
| Isopropoxy species (three types) | 2965 | $\nu_{as}(CH_3)$ |
| | 2932 | $\nu_s(CH_3)$ |
| | 2864 | $\nu(CH_2)$ |
| | 1464 | $\delta_{as}(CH_3)$ |
| | 1373, 1333 | $\delta_s(CH_3)$ |
| | 1172, 1130, 1014 | $\nu$(C–O) |
| Acetone (ads) | 1680 | $\nu$(C=O) |
| $CH_3COO^-$ (three types) | 1602, 1543 | $\nu_{as}(COO)$ |
| | 1440 | $\nu_s(COO)$ |
| $H_2O$ | 1620 | $\delta(H_2O)$ |

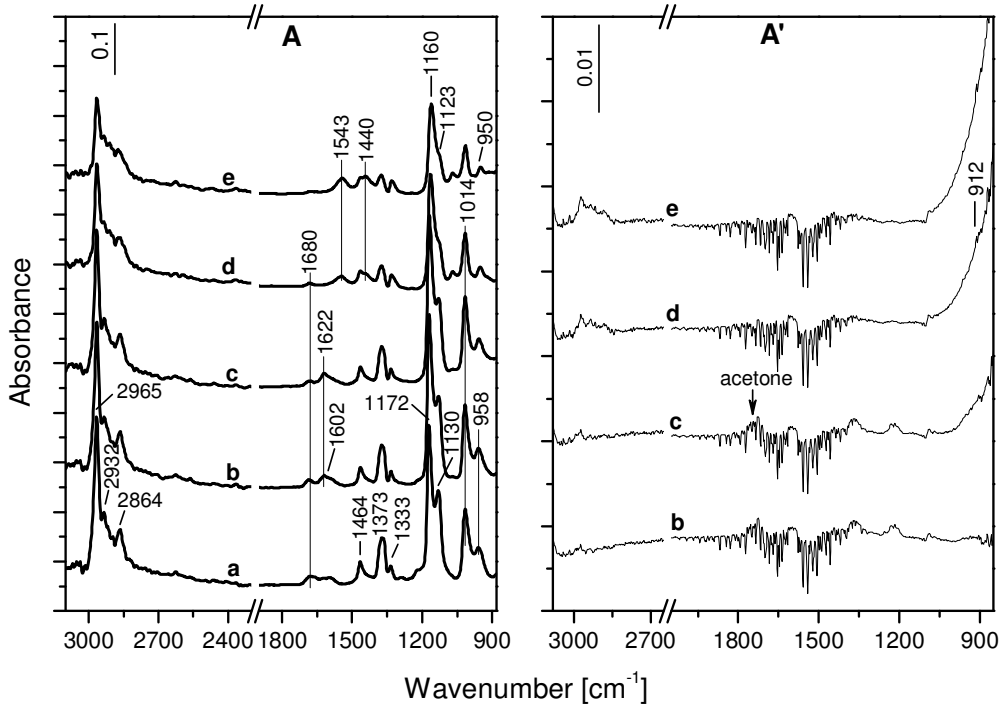


Fig. 34. Panel A: FT-IR spectra collected during the exposure of the $ZrO_2$ sample to 1 mbar $CH_3CH_2OHCH_3$ for 10 min at room temperature followed by evacuation for 10 min (a), and after heating the isolated IR cell for 15 min at 373K (b), 423 K (c), 473 K (d) and 523 K (e). Panel A`: Gas phase spectra at each temperature.

III.3.2. Adsorption of Propan-2-ol over the $Zr_6Nb_2O_{17}$ sample

The adsorption of propan-2-ol on the 25NbZ-P catalyst at room temperature for 10 min followed by evacuation for 10 min gives rise of spectrum a in Fig. 35. The interaction between the sample and isopropyl alcohol results in the appearance of surface isopropoxy species, adsorbed acetone and acetate species (see Table 16 for the assignments of the bands). The weak absorption at 1240 $cm^{-1}$ is typical of the δ(OH) bending mode of the isopropanol molecule, which indicates the presence of non-dissociatively adsorbed alcohol [159]. Note that this feature is absent in the spectrum of isopropanol adsorbed on zirconia (Fig. 34, spectrum a). The intensity of the band at 1688 $cm^{-1}$ corresponding to the ν(C=O) stretching vibration of acetone generated at room temperature on the 25NbZ-P

catalyst is much stronger than that on zirconia (see Fig. 34, spectrum a). As shown by Scheme 5, the formation of acetone is promoted by strong basic sites on the catalyst surface. However, the incorporation of Nb(V) into zirconia causes the appearance of strong Brønsted acidity (see Section *III.1.1.5. Brønsted acidity*), which is associated with lowering in the density of surface basic sites. This conclusion is supported by the $CO_2$ chemisorption experiments on alumina-supported niobia [160], which reveals that the concentration of basic sites decreases with niobium content. The answer to this apparent contradiction may be the presence of reducible niobium sites on the surface of 25NbZ-P sample. Zaki and coworkers [159] have shown that the availability of redox Lewis sites favors the isopropanol dehydrogenation activity. The following reaction scheme for the formation of acetone during the interaction of isopropanol with the surface of the 25NbZ-P sample can be proposed:

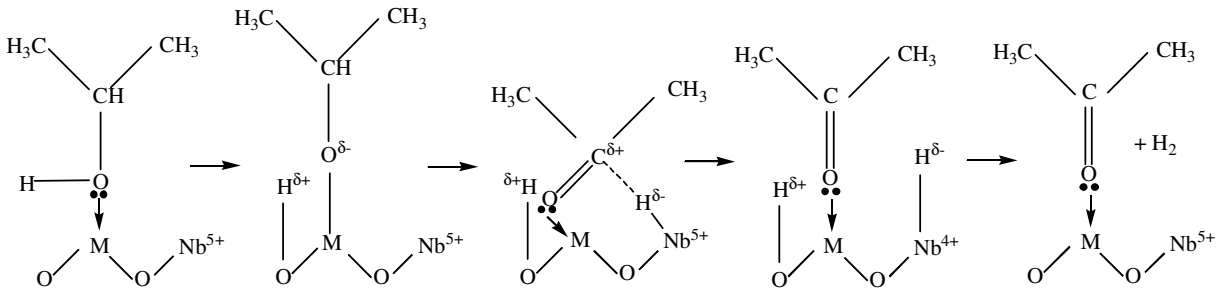


Scheme 6

where M = $Zr^{4+}$ or $Nb^{5+}$.

Simultaneously with the appearance of adsorbed acetone at room temperature, acetate species are formed with $\nu_{as}$(COO) mode at 1579 $cm^{-1}$. The ability of the 25NbZ-P catalyst to oxidize the adsorbed acetone already at room temperature has been shown in Section III.2.2.4. The increase in the temperature up to 473 K leads to increase in the

amount of the acetates at the expense of adsorbed acetone (Fig. 35A, spectra b-d). The concentrations of molecularly adsorbed isopropanol and isopropoxy species decrease also in this temperature range and at 523 K (spectrum e) they disappear almost completely.

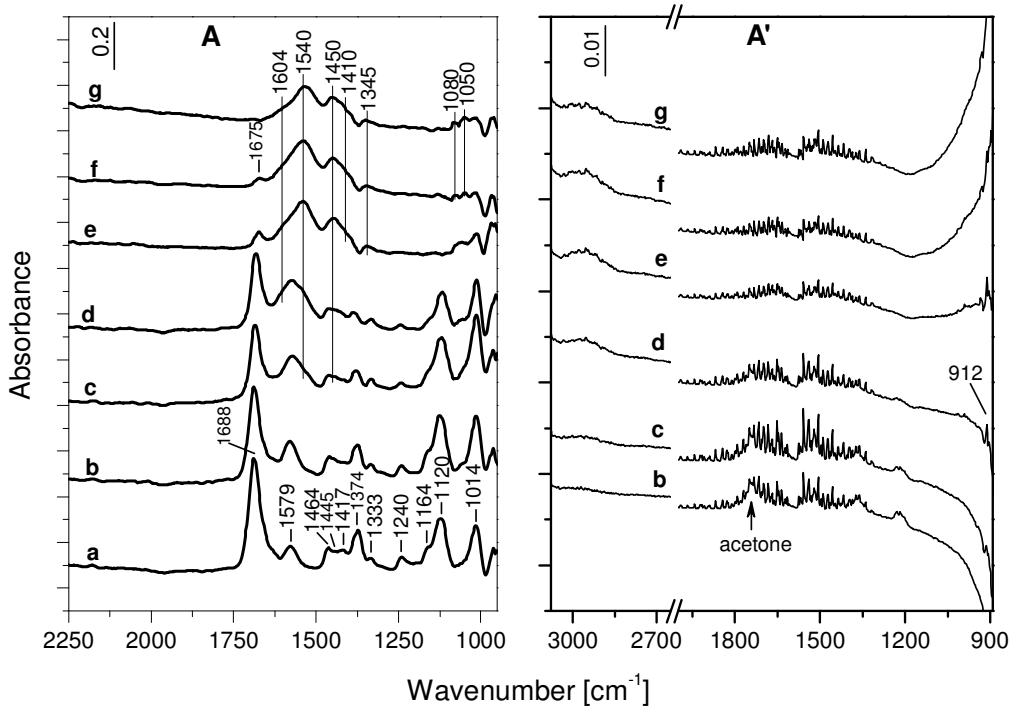


Fig. 35. Panel A: FT-IR spectra collected during the exposure of the 25NbZ-P catalyst to 1 mbar isopropanol for 10 min at room temperature followed by evacuation for 10 min (a) (in Panel A), and after heating the isolated IR cell for 15 min at 373 K (b), 423 K (c), 473 K (d), 523 K (e), 573 K (f) and 623 K (g). Panel A´: Gas phase spectra at each temperature.

Further increase in the temperature to 623 K does not cause considerable changes in the spectrum. The gas phase spectra show that gaseous acetone is present up to 473 K (Fig. 35A, spectra b-d). At 423 K small amount of propene is detected at 912 $cm^{-1}$. The concentration of propene increases with the temperature and parallels the decrease in the amount of adsorbed isopropoxy species. It should be noted that the temperature of formation of propene is significantly lower than that in the case of zirconia (523 K). This

fact confirms that the density of surface acid sites of the 25NbZ-P sample is higher than that of zirconia.

The obtained results suggest that the 25NbZ-P sample could find application as low-temperature catalyst for oxidant-free catalytic dehydrogenation of isopropanol to acetone and molecular hydrogen. This process is important from viewpoint of safety of the reaction. To the best of our knowledge supported Ru, Ag and Cu catalysts are reported to be active in the reaction of oxidant-free dehydrogenation of alcohols [161-165]. Further studies are needed in order to find if the niobia-zirconia solid solutions have the potential of noble metal-free dehydrogenation catalysts.

**Table 16.** Assignments of the adsorption bands in the spectra observed during the high-temperature adsorption of propan-2-ol on the 25NbZ-P catalyst.

| Species | Band position, $cm^{-1}$ | Vibration |
|---|---|---|
| Molecularly ads. isopropanol | 1240 | $\delta$(OH) |
| Isopropoxy species (three types) | 1464, 1446<br>1373, 1333<br>1164, 1120, 1014 | $\delta_{as}(CH_3)$<br>$\delta_s(CH_3)$<br>$\nu$(C–O) |
| Acetone (ads) | 1688 – 1675<br>1417<br>1374 | $\nu$(C=O)<br>$\delta_{as}(CH_3)$<br>$\delta_s(CH_3)$ |
| $CH_3COO^-$ (three types) | 1604, 1579, 1540<br>1410, 1450, 1445<br>1345<br>1080, 1050 | $\nu_{as}(COO)$<br>$\nu_s(COO)$<br>$\delta(CH_3)$<br>$\rho(CH_3)$ |

III.3.3. Adsorption of Propan-2-ol over the 20WN873 sample

The results of interaction of isopropanol with the 20WN873 sample show that this material is inactive in the alcohol transformation reaction. Small amount of gaseous

acetone has been detected at room temperature. The increase in the temperature up to 623 K did not cause any increase in the amount of acetone or formation of other gaseous products like propene. Therefore, we investigated the possibility of the 20WN873 sample to catalyze the oxidative dehydration and dehydrogenation of isopropanol, which has been evaluated by in situ FTIR spectroscopy following the transformation of surface species and product formation.

The spectrum obtained after the adsorption of a gas mixture (1 mbar isopropanol+10 mbar $O_2$) for 10 min at room temperature is shown in Fig. 36A, spectrum a. The bands at 1164, 1128 and 1112 $cm^{-1}$ are due to the ν(C–O) stretching vibration of three types of isopropoxy species. The isopropoxides display the antisymmetric bending $\delta_{as}(CH_3)$ modes at 1487, 1468 and 1445 $cm^{-1}$, symmetric bending $\delta_s(CH_3)$ modes at 1382, 1370 and 1335 $cm^{-1}$. The weak band at 1222 $cm^{-1}$ corresponds to the OH deformation of molecularly adsorbed isopropanol [159]. The spectrum in the OH stretching region contains broad absorption between 3500 and 2500 $cm^{-1}$ (not shown) due to H-bonded OH groups. This allows assigning the bands at 1640 and 1607 $cm^{-1}$ to coordinated water molecules. The bending mode of isolated water molecule is at 1597 $cm^{-1}$ [90]. This mode shifts upward upon formation of hydrogen bonds [166]. It can be proposed that the water molecules adsorbed on the 20WN873 sample exist in two different environments providing different extent of H-bonding. These water molecules are produced according to the reaction depicted by Scheme 3. The weak band at 1545 $cm^{-1}$ is best assigned to the $\nu_{as}(COO)$ mode of acetate species. The negative band at 1018 $cm^{-1}$ indicates the presence of altered wolframyl ($W^{6+}$=O) species [119]. All absorptions in Fig. 36A`, spectrum a, correspond to different modes of gaseous 2-propanol and the band at 1746 $cm^{-1}$ is due to the ν(C=O) mode of gaseous acetone. The formation of acetone in the gas phase indicates that the dehydrogenation of isopropanol takes place already at room temperature and

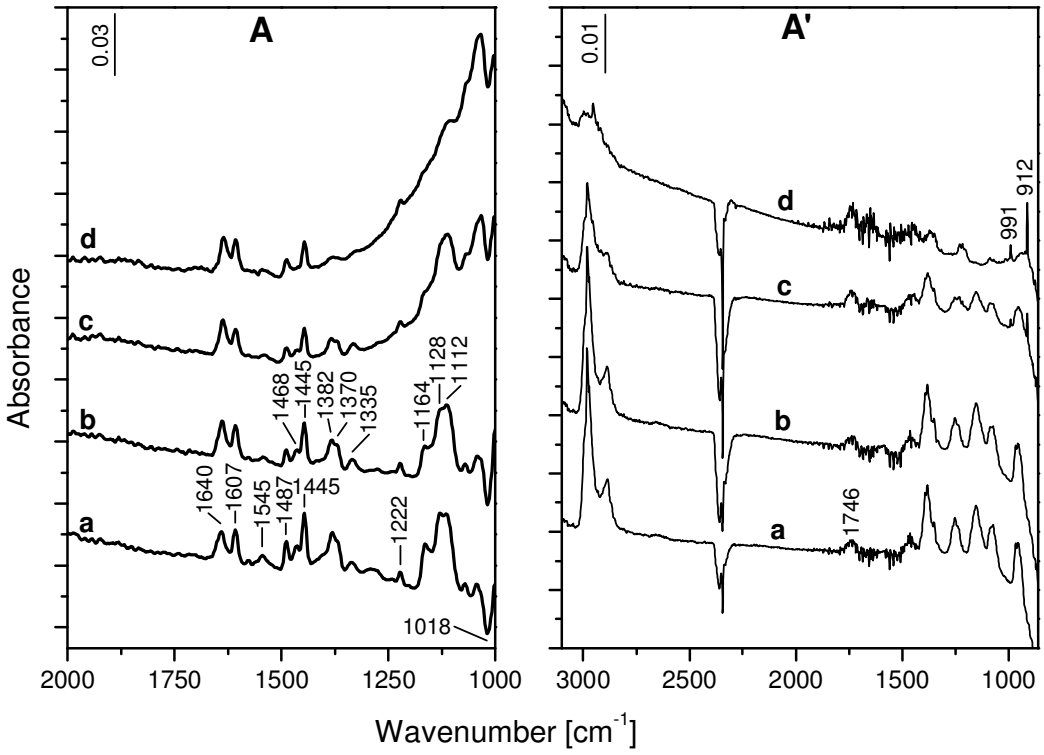


Fig. 36. Panel A: FT-IR spectra collected during the exposure of the 20WN873 sample to a (1 mbar $CH_3CHOHCH_3$ +10 mbar $O_2$) mixture for 1 min at room temperature (a) followed by heating the isolated IR cell for 15 min at 373 K (b), 423 K (c) and 473 K (d). Panel A`: Gas phase spectra at each temperature.

involves surface redox sites ($W^{6+}/W^{5+}$ and $Nb^{5+}/Nb^{4+}$) analogous to the 25NbZ-P sample. However, in contrast to the niobia-zirconia mixed oxide, small amount of adsorbed acetone has been detected. The reason for this could be the unavailability of adsorption sites, which are most likely occupied by the adsorbed water molecules. Increasing the temperature to 423 K (Fig. 36A, spectrum c) causes decrease in the concentration of the adsorbed isopropoxides, which is evident by the lowering in the intensities of the absorption bands in the 1500 – 1250 $cm^{-1}$ range. At the same time, a new band at 1040 $cm^{-1}$ is detected, which could be associated with reoxidized wolframyl groups differing in the localization from the original ones. If this assumption is correct the negative band at

1018 $cm^{-1}$ should be present in spectrum c (Fig. 36A). However, analogous reoxidation of reduced niobium ions should be expected to occur and the $\nu(Nb^{5+}=O)$ mode of restored $Nb^{5+}=O$ groups may cancel the negative $\nu(W^{6+}=O)$ stretching vibration. The gas phase spectrum taken at 423 K shows the appearance of propene identified by the weak sharp bands at 991 and 912 $cm^{-1}$. Increasing the temperature to 473 K (Fig. 36A`, spectrum d) results in further increase in the amounts of gaseous acetone and propene. These experimental facts lead to the conclusion that the role of oxygen is to keep the catalyst surface oxidized ensuring sufficient amount of strong acid sites (Lewis and Brønsted) necessary for the dehydration and dehydrogenation of isopropanol over the 20WN873 catalyst. This mixed oxide could be of interest regarding the development of new catalysts for oxidative transformations of alcohols.

**Table 17.** Assignments of the adsorption bands in the spectra observed during the high-temperature adsorption of propan-2-ol on the 20WN873 catalyst.

| Species | Band position, $cm^{-1}$ | Vibration |
|---|---|---|
| Molecularly ads. isopropanol | 1222 | $\delta$(OH) |
| Isopropoxy species<br>(three types) | 1487, 1468, 1445<br>1382, 1370, 1333<br>1164, 1128, 1112 | $\delta_{as}(CH_3)$<br>$\delta_s(CH_3)$<br>$\nu$(C–O) |
| $H_2O$ (ads) | 1640, 1607 | $\delta(H_2O)$ |
| $CH_3COO^-$ | 1545 | $\nu_{as}$(COO) |

# IV. Conclusions

The nature of the Nb(V) species in two different precursor solutions used for synthesis of $Nb_2O_5$-$ZrO_2$ and $WO_3$-$Nb_2O_5$ mixed oxides has been identified. The precursor solutions prepared by dissolution of ammonium niobium(V) oxalate contain the $[Nb(OH)_2(C_2O4)_2]^-$ ions. The species $[Nb_2(O_2)_3]^{4+}$ are present in the solutions obtained by decomposition of the $[Nb(OH)_2(C_2O_4)_2]^-$ complex by excess $H_2O_2$. Using $H_2O_2$ as a solvent increases the solubility of ammonium niobium(V) oxalate and allows preparation of concentrated solutions containing Nb(V) ions.

The impregnation of hydrated zirconia with concentrated peroxoniobium(V) precursor solutions allows the synthesis of $Nb_2O_5$-$ZrO_2$ samples with high niobium loading (up to 30 wt %) without formation of $Nb_2O_5$ as a separate phase. The materials with Nb(V) content below 25 wt % contain two phases: tetragonal zirconia and $Zr_6Nb_2O_7$. The presence of a single phase of $Zr_6Nb_2O_{17}$ has been observed for samples with 25 and 30 wt % of Nb. The formation of $Zr_6Nb_2O_{17}$ is favored by the partial solubility of hydrated zirconia in the $H_2O_2$ solution.

The surface acidity of the $Nb_2O_5$-$ZrO_2$ samples depends on the amount of niobia. The samples with content of Nb between 4 and 19 wt % possess both Lewis and Brønsted acidity, whereas the 25NbZ-P and 30NbZ-P samples are characterized mainly by Brønsted acidity. The $Zr_6Nb_2O_{17}$ sample has the highest amount of Brønsted acid sites allowing a good dispersion of deposited Pd(II) species.

The structural characterization of the $WO_3$-$Nb_2O_5$ system prepared by the peroxo route shows that the TT-$Nb_2O_5$ or the T-$Nb_2O_5$ phases can accept at least 20 wt % $WO_3$ (22 mol %) into their lattices as a solid solution and no phase separation is observed after the calcination between 773 and 973 K. The 40WN sample calcined at 773 and 873 K contains crystalline TT-$Nb_2O_5$ phase and amorphous part. The latter gives rise to the

stoichiometric mixed oxide $4Nb_2O_5.7WO_3$ after the calcination at 973 K. The same compound as a pure phase is observed after the crystallization of the 60WN sample at 973 K. The 80WN sample is mainly amorphous and contains negligible amount of crystallinity after the calcination at 973 K. Heating the sample at 1073 K results in the formation of the orthorhombic $4Nb_2O_5.7WO_3$ phase and monoclinic $WO_3$ phase, which contains $Nb_2O_5$ as a solute. The peroxo route developed by us gives the possibility to synthesize $WO_3$-$Nb_2O_5$ mixed oxides at low calcination temperatures (max. 1073 K) and to stabilize them at ambient temperature.

The surface acidity of the xWNy samples depends on the amount of tungsta and the calcination temperature, which affects the degree of crystallization. The maximum amount and the highest strength of Brønsted acid sites are observed for the TT-$Nb_2O_5$ phase. Furthermore, the presence of other phases, e.g. T-$Nb_2O_5$, $4Nb_2O_5.7WO_3$, $WO_3$, decreases the strength of Brønsted acidity of the samples. Among the fully crystallized materials the 20WN873 sample has the highest and strongest Brønsted acidity.

The conversion of $NO_x$ in the SCR of $NO_x$ with propene in excess oxygen over the solid solution $Zr_6Nb_2O_{17}$ passes through a maximum at 493 K. The results of detailed in situ FT-IR investigation have shown that over the $Zr_6Nb_2O_{17}$ sample, characterized by strong Brønsted acidity, the activation of propene in the presence of adsorbed $NO_x$ species is quite easy at low temperatures, producing surface isopropoxides. The interaction of the latter species with the surface nitrate complexes leads to the formation of nitroacetone. It is proposed that nitroacetone transforms through two parallel reactions: (i) with the involvement of basic oxide sites of the catalyst producing acetate species and aci-nitromethane (path (1)) and (ii) oxidation to acetates and $CO_x/H_2O$ with release of $NO_2$ (path (2)). The latter process is important at temperatures higher than 473 K. The aci-nitromethane generates NCO species coordinated to the cationic sites of the mixed oxide.

The surface isocyanates are detected already at room temperature. It is proposed that the isocyanates react with the $NO_3^-/NO_2$ surface complex formed by both oxidation of NO and oxidation of nitroacetone. The facts that the NCO consumption is observed by in situ FT-IR spectroscopy already at 373 K and the $NO_x$ reduction over the $Zr_6Nb_2O_{17}$ catalyst is significant at temperatures below 473 K suggest that the nitroacetone and isocyanates could be the main reaction intermediates.

Pd-promoted (0.1 wt %) $Zr_6Nb_2O_{17}$ solid solution has lower $NO_x$ conversion than the 25NbZ-P sample. It is possible that the surface concentration of the $O^{2-}$ ions involved in the transformation of nitroacetone to aci-nitromethane decreases after the deposition of Pd(II) as a result of formation of $Pd(O)_n^{2+}$ entities. This could lead to lowering of the concentration of the NCO species, which causes decrease in the $NO_x$ conversion.

The $Zr_6Nb_2O_{17}$ catalyst displays good resistance toward $SO_2$ poisoning. The activity declines from 62 to 54 % in the fast poisoning experiment (200 ppm of $SO_2$ in the feed gas) and remains unchanged for more than 5 h. The in situ FT-IR investigations show that the nitrate species or activated $NO_2$ lower(s) the oxidation temperature of $SO_2$ to sulfate species. The presence of surface $SO_4^{2-}$ groups decreases the amount of adsorbed nitrates, respectively nitroacetone, and hinders the transformation of the latter compound to NCO species. This causes decrease in the catalytic activity.

The results of the investigation show that the catalytic properties of the $Zr_6Nb_2O_{17}$ solid solution could be of interest regarding the development of sulfur-tolerant, low-temperature catalysts for the SCR of $NO_x$ with hydrocarbons.

The potential of 25NbZ-P and 20WN873 samples is investigated as low-temperature catalysts for alcohol transformations by means of FTIR spectroscopy. The 25NbZ-P sample has potential as catalyst for the oxidant-free dehydrogenation of isopropanol to acetone and molecular hydrogen. The 20WN873 sample shows the ability

to transform isopropanol to propene in the oxidative atmosphere. This material could be a candidate for a new mixed oxide catalyst in the oxidative transformation of alcohols.

# V. References


1. J. P. A. Neeft, M. Makkee and J. A. Moulijn, *Fuel Process. Technol.* **47** (1996) 1-69.
2. www.dieselnet.net.
3. http://en.wikipedia.org/wiki/European_emission_standards.
4. http://www.roadtransport.com.
5. A. C. Lloyd and T. A. Cackette, *J. Air and Waste Manage. Assoc.* **51** (2001) 809.
6. C. C. Pounder and D. F. Woodyard, *Pounder's Marine Diesel Engines and Gas Turbines*, 9th Edition, 2009, Elsevier Butterworth Heinemann Press.
7. J. Kaspar, P. Fornasiero, N. Hickey, *Catal. Today* **77** (2003) 419.
8. R. Burch, *Catal. Rev.* **46** (2004) 271.
9. http://herkules.oulu.fi/isbn9514269543/html/c299.html.
10. http://openlearn.open.ac.uk.
11. M. Twigg, *Platinum Metals Rev.* **45** (2001) 176.
12. http://autozine.org/technical_school/engine/petrol1.html.
13. N. Miyoshi and S. Mastumoto, Sci. Technol. Catal. (1998).
14. Z. Liu, S. I. Woo, Catalysis Reviews, 48 (2006) 43.
15. M. Ghaffarpour, M. Azarfam and A. Noorpoor, *JSME Int J. Ser. B*, **49** (2006) 1298.
16. J. Suzuki, S. Matsumoto, *Top. Catal.* **28** (2004) 171.
17. http://www.greencarcongress.com/2007/08/toyota-enhancin.html.
18. D. Fino and V. Specchia, *Powder Technol.* **180** (2008) 64.
19. J. M. Trichard, *Stud. Surf. Sci. Catal.* **171** (2007) 211.
20. O. Kröcher, *Stud. Surf. Sci. Catal.* **171** (2007) 261.
21. G. Centi, S. Perathoner, *Stud. Surf. Sci. Catal.* **171** (2007) 1.

22. P.L.T. Gabrielsson, *Top. Catal.* **28** (2004) 177.

23. F. Klingstedt, K. Arve, K. Ernen, D.Y. Murzin, *Acc. Chem. Res.* **39** (2006) 273.

24. E. Jobson, *Top. Catal.* **28** (2004) 191.

25. R. Burch, J.P. Breen, F.C. Meunier, *Appl. Catal. B* **39** (2002) 283.

26. J. C. Lavalley, *Catal. Today* **27** (1996) 377.

27. M. Waqif, A. M. Saad, M. Bensitel. J. Bachelier, O. Saur and J. C. Javalley, *J. Chem. Soc. Faraday Trans.* **88** (1992) 2931.

28. T. Ushikubo, *Catal. Today* **57** (2000) 331.

29. S. Okazaki, H. Kuroha, T. Okuyama, *Catal. Lett.* (1985) 45.

30. M. Ziólek, I. Sobczak, I. Nowak, M. Daturi and J.C. Lavalley, *Top. Catal.* **11/12** (2000) 343.

31. I. Sobczak, M. Ziólek, and M. Nowacka, *Microp. Mesopor. Mater.* **78** (2005) 103.

32. J. Goscianska, P. Bazin, O. Marie, M. Daturi, I. Sobczak, M. Ziolek, *Catal. Today* **119** (2007) 78.

33. J. Goscianska, M. Ziolek, *Catal. Today* **137** (2008) 197.

34. K. Tanabe, *Catal. Today* **78** (2003) 65.

35. P. Viparelli, P. ciambelli, L. Lisi, G. Ruoppolo, G. Russo and J.C. Volta, *Appl. Catal. A* **184** (1999) 291.

36. M. Hino, M. Kurashige and K. Arata, *Catal. Commun*. **5** (2004) 107.

37. S. R. G. Carrazan, C, Martin, G. Solana and V. Rives, *Langmuir* **17** (2001) 6968.

38. D. S. Kim, M. Osrimetcki, I. E. Wachs, *J. Mol. Catal. A* **106** (1996) 93.

39. I. E. Wachs, *Catal. Toda*y **27** (1996) 437.

40. J,-H. Jehng, A. M. Turek and I.E. Wachs, *Appl. Catal.* A **23** (1992) 179.

41. C. Martin, G. Solana, P. Malet and V. Rives, *Catal. Today* **78** (2003) 365.

42. M. Ziolek, *Catal. Today* **78** (2003) 47.

43. J. Mitadera and H. Hinode, *Appl. Catal. B* **39** (2002) 205.

44. H. Kawai and H. Hinode, *React. Kinet. Catal. Lett.* **93** (2008) 67.

45. T. Kikuchi, M. Kumagai, *J. Japan Petr. Inst.* **44** (2001) 145.

46. T. Kikuchi, M. Kumagai, *J. Japan Petr. Inst.* **44** (2001) 340.

47. M. A. Abdel-Rehim, A. C. B. dos Santos, V. L. L. Camorim and A. da Costa Faro, Jr., *Appl. Catal. A* **305** (2006) 211.

48. K. Tanabe, *Catal. Today* **78** (2003) 65.

49. N. Adler and C. F. Hiskey, *J. Am. Chem. Soc.* **79** (1956) 1827.

50. N. Adler and C. F. Hiskey, *J. Am. Chem. Soc.* **79** (1956) 1831.

51. N. Adler and C. F. Hiskey, *J. Am. Chem. Soc.* **79** (1956) 1834.

52. Y. Narendar and G. L. Messing, *Chem. Mater.* **9** (1997) 580.

53. D. Bayot, M. Degand, B. Tinant and M. Devillers, *Inorg. Chem. Acta* **359** (2006) 1390.

54. M. Kantcheva and C. Koz, *J. Mater. Sci.* **42** (2007), p. 6074.

55. T. Chafik, S. Kameoka, Y. Ukisu and T. Miyadera, *J. Mol. Catal. A* **136** (1998) 203.

56. T. Tanaka, T. Okuhara and M. Misono, *Appl. Catal. B* **4** (1994) L1.

57. T. Okuhara, Y. Hasada and M. Misono, *Catal. Today* **35** (1997) 83.

58. K.A. Bethke, C. Li, M.C. Kung, B. Yang and H.H. Kung, *Catal. Lett.* **31** (1995) 287.

59. Y. Ukisu, S. Sato, A. Abe and K. Yoshida, *Appl. Catal. B* **2** (1993) 147

60. B. Djonev, B. Tsyntsarski, D. Klissurski and K. Hadjivanov, *J. Chem. Soc. Faraday Trans.* **93** (1997) 4055.

61. M. Yamaguchi, *J. Chem. Soc. Faraday Trans.* **93** (1997) 3581.

62. A.D. Cowan, N.W. Cant, B.S. Haynes and P.F. Nelson, *J. Catal.* **176** (1998) 329.

63. S. Kameoka, T. Chafik, Y. Ukisu and T. Miyadera, *Catal. Lett.* **51** (1998) 11.

64. M. Haneda, Y. Kintaichi, M. Inaba and H. Hamada, *Catal. Today* **42** (1998) 127.

65. F.C. Meunier, J.P. Breen, V. Zuzaniuk, M. Olsson and J.R.H. Ross, *J. Catal.* **187** (1999) 493.

66. V. Zuzaniuk, F.C. Meunier and J.R.H. Ross, *J. Catal.* **202** (2001) 340.

67. M. Haneda, E. Joubert, J.-C. Ménézo, D. Duprez, J. Barbier, N. Bion, M. Daturi, J. Saussey, J.-C. Lavalley and H. Hamada, *J. Mol. Catal. A* **175** (2001) 179.

68. V. A. Sadykov, S.L. Baron, V.A. Matyshak, G.M. Alikina, R.V. Bunina, A.Y. Rozovskii, V.V. Lunin, E.V. Lunina, A.N.Kharlanov, A.S. Ivanova, S.A. Veniaminov, *Catal. Lett.* **37** (1996) 157.

69. V. A. Sadykov, V.V. Lunin, V.A. Matyshak, E. A. Paukshtis, A.Y. Rozovskii, N. N. Bulgakov, J. R. H. Ross, *Kinet. Katal.* **44** (2003) 379.

70. V. A. Matyshak, V. F. Tret'yakov, K. A. Chernishev, T. N. Burdeinaya, V. N. Korchak and V. A. Sadykov, *Kinet. Katal.* **47** (2006) 747.

71. O. Gorce, F. Baudin, C. Thomas, P. Da Costa and G. Djega-Mariadassou, *Appl. Catal. B* **54** (2004) 69.

72. N. El Kolli, C. Potvin and C. Thomas, J. *Catal.* **259** (2008) 240.

73. M. Kantcheva and I. Cayirtepe, *Catal. Lett.* **115** (2007) 148.

74. M. Kantcheva, H. Budunoğlu and O. Samarskaya, *Catal. Commun.* **9** (2008) 874.

75. I. Cayirtepe, A. Naydenov, G. Ivanov and M. Kantcheva, *Catal. Lett.* **132** (2009) 438.

76. G. R. Bamwenda, A. Obuchi, S. Kushiyama and K. Mozono, *Stud. Surf. Sci. Catal*. **130** (2000) 1271.

77. K.-I. Shimizu, H. Kawabata, A. Satsuma and T. Hattori, *J. Phys. Chem. B* **103** (1999) 5240.

78. K.-I. Shimizu, J. Shibata, H. Yoshida, A. Satsuma and T. Hattori, *Appl. Catal. B* **30** (2001) 151.

79. J.-H. Lee, A. Yezerets, M.C. Kung and H.H. Kung, *Chem. Commun*. **15** (2001) 1404.

80. M. Kantcheva, *J. Catal.* **204** (2001) 479.

81. M. Kantcheva, *Appl. Catal. B* **42** (2003) 89.

82. H. Hamada, Y. Kintaichi, M. Sasaki and T. Ito, *Appl. Catal.* **75** (1991) L1.

83. H. Hamada, Y. Kintaichi, M. Sasaki, T. Ito and T. Yoshinari, *Appl. Catal. A* **88** (1992) L1.

84. T. Miyadera, *Appl. Catal. B* **2** (1993) 199.

85. M. Tabata, H. Tsuchida, K. Miyamoto, T. Yoshinari, H. Yamazaki, H. Hamada, Y. Kintaichi, M. Sasaki and T. Ito, *Appl. Catal. B* **6** (1995) 169.

86. Y. Ukisu and T. Miyadera, *Catal. Lett.* **39** (1996) 265.

87. R. Burch, E. Halpin and J.A. Sullivan, *Appl. Catal. B* **17** (1998) 115.

88. T.J. Toops, A.B. Walters and M.A. Vannice, *Catal. Lett.* **64** (2000) 65.

89. K.I. Hadjiivanov, *Catal. Rev.-Sci. Eng.* **42**(1&2) (2000) 71-144.

90. K. Nakamoto, "Infrared and Raman Spectra of Inorganic and Coordination compounds" Part B, 5$^{th}$ edition, Wiley, New York, 1997.

91. S.J. Huang, A.B. Walters and M.A. Vannice, *J. Catal.* **192** (2000) 29-47.

92. M. Kantcheva and E. Z. Ciftlikli, *J. Phys. Chem. B* **106** (2002) 3941.

93. R. Srinivasan, R. J. De Angelis, M. B. Harris, S. F. Simpson and B. H. Davis, *J. Mater. Res.* **3** (1988) 787.

94. F. J. Berry, S. J. Skinner, I. M. Bell, R. J. H. Clark and C. B. Ponton, *J. Solid State Chem.* **145** (1999) 394.

95. K. Fütterer, S. Schmid, J. G. Thompson and R. L. Withers, *Acta Cryst. B* **51** (1995) 688.

96. H. Kominami, M. Inoue and T. Inui, *Catal. Today* **16** (1993) 309.

97. D. Lu, B. Lee, J. N. Kondo and K. Domen, *Micropor. Mesopor. Mater.* **75** (2004) 203.

98. R. Brayner and F. Bozon-Verduraz, *Phys. Chem. Chem. Phys.* **5** (2003) 1457.

99. J.-M. Jehng and I. E. Wachs, *J. Phys. Chem.* **95** (1991) 7373.

100. M. Li, Z. Feng, G. Xiong, P. Ying, Q. Xin and C. Li, *J. Phys. Chem. B* **105** (2001) 8107.

101. X. Gao, I. E. Wachs, M. S. Wong and J. Y. Ying, *J. Catal.* **203** (2001) 18.

102. T. Onfroy, G. Clet and M. Houalla, *J. Phys. Chem. B* **109** (2005) 14588.

103. K. T. Jung, A.T. Bell, J. Molec. Catal. A 163 (2000) 27.

104. M. H. Healy, L. F. Wieserman, E. A. Arnett and K. Wefers, *Langmuir* **5** (1989) 114.

105. A. Travert, O. V. Manoilova, A. A. Tsyganenko, F. Maugé and J. C. Lavalley, *J. Phys. Chem. B* **106** (2002) 1350.

106. C. Morterra, G. Meligrana, G. Cerrato, V. Solinas, E. Rombi and M. F. Sini, *Langmuir* **19** (2003) 5344.

107. A. Rakai, D. Tessier and F. Bozon-Verduraz, *N. J. Chem.* **16** (1992) 869.

108. G. Busca, *Catl. Today* **41** (1998) 191.

109. S. Tamura, *J. Mater. Sci.* **7** (1972) 298.

110. J.G. Weissman, E.I. Ko, P. Wynblatt and J.M. Howe, *Chem. Mater.* **1** (1989) 187.

111. L. J. Fiegel, G. P. Mohanty and J. H. Healy, *J. Chem. Eng. Data* **9** (1964).

112. R. S. Roth and J. L. Waring, *J. Research Nation. Bureau Stand. A. Physics and Chemistry* **70A** (1966) 281.

113. J.-M. Jehng and I. E. Wachs, *Chem. Mater.* **3** (1991) 100.

114. D. G. Barton, M. Shtein, R. D. Wilson, S.L. Soled and E. Iglesia, *J. Phys. Chem B* **103** (1999) 630.

115. M. Valigi, D. Gazzoli, I. Pettiti, G. Matei, S. Colonna, S. De Rossi and G. Ferraris, *Appl. Catal. A* **231** (2002) 159.

116. M. Valigi, D. Gazzoli, A. Cimino and E. Proverbio, *J. Phys. Chem. B* **103** (1999) 11318.

117. D. Gazzoli, M. Valigi, R. Dragone, A. Marucci and G. Mattei, *J. Phys. Chem. B* **101** (1997) 11129.

118. J. Laane, J. R. Ohlsen, *Progr. Inorg. Chem.* **28** (1986) 465.

119. M. Kantcheva, I. Cayirtepe, *J. Mol. Catal. A* **247** (2006) 88.

120. G. Busca, G. Ramis, V. Lorenzelli, A. Janin, J. C. Lavalley, *Spectrochim. Acta* **43A** (1987) 489.

121. P. F. Rossi, G. Busca, V. Lorenzelli, O. Saur, J. C. Lavalley, *Langmuir* **3** (1987) 52.

122. V. Sanchez Escribano, G. Busca,V. Lorenzelli, *J. Phys. Chem.* **94** (1990) 8939.

123. E. Finocchio, G. Busca, V. Lorenzelli, V. Sanchez Escribano, *J. Chem. Soc. Faraday Trans.* **92** (1996) 1587.

124. E. Finocchio, R. J. Willey, G. Busca, V. Lorenzelli, *J. Chem. Soc. Faraday Trans.* **93** (1997) 175.

125. G. Busca, E. Finocchio, V. Lorenzelli, G. Ramis, M. Baldi, *Catal. Today* **49** (1999) 453.

126. Y. Toda, T. Ohno, F. Hatayama, H. Miyata, *Phys. Chem. Chem. Phys.* **1** (1999) 1615.

127. M. I. Zaki, M. A. Hasan, L. Pasupulety, *Langmuir* **17** (2001) 4025.

128. M. A. Hasan, M. I. Zaki and L. Pasupulety, *Appl. Catal. A* **243** (2003) 81.

129. L. L. Adams, F. A. Luzzio, *J. Org. Chem*. **54** (1989) 5387.

130. F. Solymosi, T. Bánsági, *J. Phys. Chem.* **83** (1979) 552.

131. Y. Ukisu, S. Sato, G. Muramatsu, K. Yoshida, *Catal. Lett.* **16** (1992) 11.

132. M. Haneda, Y. Kinaichi, M. Inaba, H. Hamada, *Catal Today* **42** (1998) 127.

133. A. Satsuma, A. D. Cowan, N. W. Cant, D. L. Trimm, *J. Catal.* **181** (1999) 165.

134. T. Weingand, S. Kuba, K. Hadjiivanov and H. Knözinger, *J. Catal.* **209** (2002) 539.

135. K. Almusaiteer, S. S. C. Chuang, J. Catal. **184** (1999) 189.

136. V.A. Matysak, V.A. Sadykov, K.A. Chernyshov and J. Ross, *Catal. Today* **145** (2009) 152.

137. M. C. Kung, H. H. Kung, *Top. Catal.* **28** (2004) 105.

138. C. Li, K. A. Bethke, H. H. Kung, M. C. Kung, *J. Chem. Soc. – Chem. Commun.* (1995) 813.

139. S. Sumiya, H. He, A. Abe, N. Takezawa, K. Yoshida, *J. Chem. Soc. Faraday Trans.* **94** (1998) 2217.

140. F. Radtke, R.A. Koeppel, E.G. Minardi and A. Baiker, *J. Catal*. **167** (1997) 127.

141. P. A. Kumar, M. P. Reddy, L. K. Ju, B. Hyun-Sook and H. H. Phil, *J. Molec. Catal. A* **291** (2008) 66.

142. S. A. Beloshapkin, V. A. Matyshak, E. A. Paukshtis, V. A. Sadykov, A. N. Ilyichev, A. A. Ukharskii and V. V. Lunin, *React. Kinet. Catal. Lett.* **66** (1999) 297.

143. Y. H. Yeom, M. Li, W. M. H. Sachtler and E. Weitz, *J. Catal.* **238** (2006) 100.

144. R. G. Pearson, D. H. Anderson and L. L. Alt, *J. Am. Chem. Soc.* **77** (1955) 527.

145. K. Shimizu, H. Kawabata, H. Maeshima, A. Satsuma, T. Hattori, *J. Phys. Chem. B* **104** (2000) 2885.

146. Y. Chi, S. S. C. Chuang, *J. Catal.* **190** (2000) 75.

147. J. A. Anderson, C. Marquez-Alvarez, M. J. Lopez-Minoz, I. Rodriguez-Ramos and A. Guerrero-Ruiz, *Appl. Catal. B* **14** (1997) 189.

148. M. Kantcheva, A. S. Vakkasoglu, *J. Catal.* **223** (2004) 352.

149. C. C. Chang, *J. Catal.* **53** (1978) 374.

150. K. Tanabe, M. Misono, Y. Ono and H. Hattori, "Solid Acids and Bases Their Catalytic Properties", Elsevier Science Publishers, 1989.

151. C. Resini, T. Montanari, G. Busca, J.-M. Jehng and I.E. Wachs, *Catal. Today* **99** (2005) 105.

152. E.A. El-Sharkawy, A.S. Khder, A.I. Ahmed, *Micropor. Mesopor. Mat.* **102** (2007) 128.

153. A. Davydov, "Moleculer Spectroscopy of Oxide Catalyst Surfaces", Wiley, 2003.

154. H. Knozinger, A. Scheglila, *J. Catal.* **17** (1970) 252.

155. A. Gervasini, G. Belussi, J. Fenyvesi, A. Auroux, *J. Phys. Chem.* **99** (1995) 5117.

156. C. Lahousse, J. Bachelier, J.-C. Lavalley, H. Lauron-Pernot, A. M. Le Govic, *J. Mol. Catal.* **87** (1994) 329.

157. B. Shi, H. A. Dabbagh, B. H. Davis, *J. Mol. Catal. A* **141** (1999) 257.

158. B. H. Davis, B. Shi *J. Catal.* **157** (1995) 359.

159. M. A. Hasan, M. I. Zaki, L. Pasupulety, *J. Mol. Catal. A* **178** (2002) 125.

160. M. A. Abdel-Rehim, A. C. B. dos Santos, V. L. L. Camorim, A. C. Faro Jr., *Appl. Catal. A* **305** (2006) 211.

161. Y. Ando, M. Yamashita and Y. Saito, *Bull. Chem. Soc. Jpn.* **76** (2003) 2045.

162. W.-H. Kim, I. Park and J. Park, *Org. Lett.* **8** (2006) 2543.

163. T. Mitsudome, S. Arita, H. Mori, T. Mizugaki, K. Jitsukawa and K. Kaneda, *Angew. Chem. Int. Ed.* **47** (2008) 7938.

164. T. Matsudome, Y. Mikami, K. Ebata, T. Mizugaki, K. Jitsukawa and K. Kaneda, *Chem. Commun.* **39** (2008) 4804.

165. K. Shimizu, K. Sugino and A. Satsuma, *Chem. Eur. J.* **15** (2009) 2341.

166. H. A. Al-Abadleh, V. H. Grassian, *Langmuir* **19** (2003) 341

**SPRINGER LICENSE**
**TERMS AND CONDITIONS**

Jan 22, 2010

This is a License Agreement between ilknur cayirtepe ("You") and Springer ("Springer") provided by Copyright Clearance Center ("CCC"). The license consists of your order details, the terms and conditions provided by Springer, and the payment terms and conditions.

**All payments must be made in full to CCC. For payment instructions, please see information listed at the bottom of this form.**

| | |
|---|---|
| License Number | 2354070063281 |
| License date | Jan 22, 2010 |
| Licensed content publisher | Springer |
| Licensed content publication | Catalysis Letters |
| Licensed content title | Characterization of Niobium-zirconium Mixed Oxide as a Novel Catalyst for Selective Catalytic Reduction of $NO_x$ |
| Licensed content author | I. Cayirtepe |
| Licensed content date | Jan 1, 2009 |
| Volume number | 132 |
| Issue number | 3 |
| Type of Use | Thesis/Dissertation |
| Portion | Full text |
| Number of copies | 1 |
| Author of this Springer article | Yes and you are the sole author of the new work |
| Order reference number | 75 |
| Title of your thesis / dissertation | Preparation and Characterization of biobia-containing solid acids |
| Expected completion date | Jan 2010 |
| Estimated size(pages) | 110 |
| Total | 0.00 USD |
| Terms and Conditions | |

Introduction

The publisher for this copyrighted material is Springer Science + Business Media. By clicking "accept" in connection with completing this licensing transaction, you agree that the following terms and conditions apply to this transaction (along with the Billing and Payment terms and conditions established by Copyright Clearance Center, Inc. ("CCC"), at the time that you opened your Rightslink account and that are available at any time at http://myaccount.copyright.com).

Limited License

With reference to your request to reprint in your thesis material on which Springer Science and Business Media control the copyright, permission is granted, free of charge, for the use indicated in your enquiry. Licenses are for one-time use only with a maximum distribution equal to the number that you identified in the licensing process.

This License includes use in an electronic form, provided it is password protected or on the university's intranet, destined to microfilming by UMI and University repository. For any other electronic use, please contact Springer at (permissions.dordrecht@springer.com or permissions.heidelberg@springer.com)

The material can only be used for the purpose of defending your thesis, and with a maximum of 100 extra copies in paper.

Although Springer holds copyright to the material and is entitled to negotiate on rights, this license is only valid, provided permission is also obtained from the (co) author (address is given with the article/chapter) and provided it concerns original material which does not carry references to other sources (if material in question appears with credit to another source, authorization from that source is required as well). Permission free of charge on this occasion does not prejudice any rights we might have to charge for reproduction of our copyrighted material in the future.

Altering/Modifying Material: Not Permitted
However figures and illustrations may be altered minimally to serve your work. Any other abbreviations, additions, deletions and/or any other alterations shall be made only with prior written authorization of the author(s) and/or Springer Science + Business Media. (Please contact Springer at permissions.dordrecht@springer.com or permissions.heidelberg@springer.com)

Reservation of Rights
Springer Science + Business Media reserves all rights not specifically granted in the combination of (i) the license details provided by you and accepted in the course of this licensing transaction, (ii) these terms and conditions and (iii) CCC's Billing and Payment terms and conditions.

Copyright Notice:
Please include the following copyright citation referencing the publication in which the material was originally published. Where wording is within brackets, please include verbatim.
"With kind permission from Springer Science+Business Media: <book/journal title, chapter/article title, volume, year of publication, page, name(s) of author(s), figure number (s), and any original (first) copyright notice displayed with material>."

Warranties: Springer Science + Business Media makes no representations or warranties with respect to the licensed material.

Indemnity
You hereby indemnify and agree to hold harmless Springer Science + Business Media and CCC, and their respective officers, directors, employees and agents, from and against any and all claims arising out of your use of the licensed material other than as specifically authorized pursuant to this license.

No Transfer of License
This license is personal to you and may not be sublicensed, assigned, or transferred by you to any other person without Springer Science + Business Media's written permission.

No Amendment Except in Writing
This license may not be amended except in a writing signed by both parties (or, in the case of Springer Science + Business Media, by CCC on Springer Science + Business Media's behalf).

Objection to Contrary Terms
Springer Science + Business Media hereby objects to any terms contained in any purchase order, acknowledgment, check endorsement or other writing prepared by you, which terms are inconsistent with these terms and conditions or CCC's Billing and Payment terms and conditions. These terms and conditions, together with CCC's Billing and Payment terms and conditions (which are incorporated herein), comprise the entire agreement between you and Springer Science + Business Media (and CCC) concerning this licensing transaction. In the event of any conflict between your obligations established by these terms and conditions and those established by CCC's Billing and Payment terms and conditions, these terms and conditions shall control.

Jurisdiction
All disputes that may arise in connection with this present License, or the breach thereof, shall be settled exclusively by the country's law in which the work was originally published.

Other terms and conditions:

v1.2

**Gratis licenses (referencing $0 in the Total field) are free. Please retain this printable license for your reference. No payment is required.**

**If you would like to pay for this license now, please remit this license along with your payment made payable to "COPYRIGHT CLEARANCE CENTER" otherwise you will be invoiced within 30 days of the license date. Payment should be in the form of a check or money order referencing your account number and this license number 2354070063281.**
**If you would prefer to pay for this license by credit card, please go to http://www.copyright.com/creditcard to download our credit card payment authorization form.**

**Make Payment To:**
**Copyright Clearance Center**
**Dept 001**
**P.O. Box 843006**
**Boston, MA 02284-3006**

**If you find copyrighted material related to this license will not be used and wish to cancel, please contact us referencing this license number 2354070063281 and noting the reason for cancellation.**

**Questions? customercare@copyright.com or +1-877-622-5543 (toll free in the US) or +1-978-646-2777.**